Head Office: Università degli Studi di Padova

Department: Padova Neuroscience Center

Ph.D. COURSE IN: Neuroscience (XXXVI cycle)

Impaired olfactory behavior and neuronal network dynamics in oligophrenin1 mutant mice.

Thesis written with the financial contribution of Fondazione Telethon.

Coordinator: Prof. Antonino Vallesi

Supervisor: Prof. Claudia Lodovichi

Co-Supervisor: Prof. Marco dal Maschio

“Poi tutto si è trasformato in una serie di fatti concreti o di nomi propri o di verbi, o di capitoli di un manuale di anatomia sfogliato come un fiore, connessi caoticamente tra loro”.

Roberto Bolaño, I detective selvaggi.

Summary.

Aim of the project. 1

Introduction. 3

Neurodevelopmental disorders as multicomponent diseases. 3

X-linked intellectual disabilities and OPHN1. 5

OPHN1. 7

The olfactory system. 9

The olfactory bulb. 12

Neuronal oscillations. 15

Mechanisms of gamma oscillations. 19

Oscillations in the olfactory bulb. 22

Recording neuronal population at cellular resolution with two-photon calcium imaging. 26

Genetically encoded sensors as reporters of neuronal activity: calcium indicators. 28

Neuronal ensembles as building blocks of the neuronal code. 29

Materials and methods. 32

Animals 32

Locomotion 32

Habituation-Dishabituation 33

Surgery for LFPs recording 34

Local Field Potentials (LFPs) signal recording. 35

LFP video analysis, pre-processing, and spectral analysis. 35

Surgery for cranial window for two-photon calcium imaging. 36

Two-photon calcium imaging experiment 37

Two-photon calcium imaging analysis. 39

Population analysis. 40

Fasudil administration. 41

Subjects. 41

Statistical tests. 42

Results. 43

Ophn1$^{-/y}$ mice exhibit olfactory impairments. 43

Ophn1$^{-/y}$ mice do not exhibit locomotor impairments. 44

Spectral analysis of Local Field Potentials (LFPs) recorded in the OB highlights abnormalities in the power of beta and gamma oscillations. 46

Ophn1$^{-/y}$ mice exhibit significant differences, at single-cell level, in calcium responses to odorants recorded by two-photon imaging. 49

Analysis of calcium peaks in response to odorant stimuli, in ophn1$^{-/y}$ and WT. 53

Impact of OPHN1 mutation on neuronal network organization, in response to odorant presentation. 55

Identification of ensembles in ophn1$^{-/y}$ and WT. 59

Impact of OPHN1 on spontaneous activity. 62

Fasudil treatment rescue behavioural performance in ophn1$^{-/y}$ mice. 63

Effects of Fasudil treatment on the LFP signal recorded in the OB. 65

Discussion. 67

Ophn1$^{-/y}$ mice do not dishabituate to the olfactory stimuli without exhibiting gross locomotor and exploratory impairments. 67

Mutant mice exhibit aberrant rhythms in the OB. 68

Absence of OPHN1 impairs neuronal network organization in the OB. 70

Fasudil rescues part of the ophn1$^{-/y}$ behavioral and spectral phenotype. 74

Aim of the project.

Neurodevelopmental disorders (NDDs), encompassing conditions like intellectual disability (ID) and autism spectrum disorder (ASD), exhibit a wide variety of cognitive, social, and adaptive deficits. Understanding the etiopathogenesis of such disorders is complicated by the absence of a singular explanation for their origins, as they emerge from an intricate combination of genetic, environmental and prenatal causes. However, a subset of ID-ASD-associated pathologies emerges from monogenic causes, being linked to distinct single gene mutations on the X-chromosome, such as *FMR1*, *PAK3*, and *OPHN1*. Among them, OPHN1 encodes a Rho GTPase-activating protein (Rho-GAP) acting as a molecular switch controlling the activation state of Rho GTPases. As a consequence, absence of OPHN1 is characterized by a persistent activity of Rho GTPases and their relative downstream signaling pathways (such as RhoA/ROCK). Remarkably, OPHN1 plays a crucial role in neuronal development, particularly in brain areas with high plasticity like the neocortex, the hippocampus, and the olfactory bulb (OB). As a Rho-GAP, OPHN1 mediates various intracellular pathways influencing spine and dendrite morphology, synaptic function, and integration.

Despite substantial *in vitro* research on OPHN1, *in vivo* evidence demonstrating its impact on the brain function has been poorly addressed. This Ph.D. project focused on elucidating OPHN1's role in behavioral and neuronal network dynamics using a validated mouse model lacking this gene (i.e., ophn1$^{-/y}$), specifically studying the olfactory bulb (OB). The OB, integral to olfactory processing, emerges as a relevant area due to its high OPHN1 expression, involvement in early neurodevelopmental pathologies, and connections with higher brain regions involved in the processing of sensory and cognitive functions, impaired in ID-ASD pathologies.

This study revealed significant alterations in olfactory guided behavior in ophn1$^{-/y}$ mice, without gross impairments in their exploratory activity. Electrophysiological recordings in

awake animals freely behaving allowed us to characterize ophn1$^{-/y}$'s phenotype in different frequency bands of oscillations. In particular, we observed a reduction in power in the high-gamma band, and an increased power in beta oscillations, compared to WT – during both active exploration and resting phases. Such frequency bands contribute to the sensory processing of the olfactory information, as well as to odorant discrimination and learning, involving a wider network of brain areas, including the piriform cortex, therefore it is likely that abnormalities in their physiological rhythmicity may severely impact brain activity.

Furthermore, two-photon calcium imaging uncovered abnormal stimulus-evoked activity in ophn1$^{-/y}$ mice, affecting calcium activity amplitude and delay upon odorant stimulation. Mutant animals displayed less correlated activity and a reduced complexity in network organization, indicating altered olfactory computation.

Ultimately, we administered a medically approved RhoA/ROCK inhibitor, i.e. Fasudil, to alleviate the impact of OPHN1 deficiency. Remarkably, the olfactory behavioral phenotype was entirely rescued, though electrophysiological recordings revealed only a partial recovery in the local field potentials (LFPs) within the olfactory bulb (OB).

This comprehensive approach shed light on OPHN1's role in neurodevelopmental pathologies, emphasizing the importance of *in vivo* investigations for an integral understanding of neuronal network dynamics and their underlying computations in neurodevelopmental pathologies. Such evidence is essential to design effective therapeutic approaches.

Introduction.

Neurodevelopmental disorders as multicomponent diseases.

Neurodevelopmental disorders (NDDs) involve a group of conditions that manifest early in a person's development, leading to a wide spectrum of alterations in cognitive, motor, and executive functions. NDDs usually appear early during childhood, but delineating their presence and severity has historically presented challenges due to social and diagnostic considerations[1]. For this reason, the number of NDDs diagnoses has steadily increased over the years. It is important to note that such disorders manifest across a broad spectrum, and individuals sharing a common diagnosis may experience varying levels of symptoms and impairments. Specifically, the intensity of these conditions typically spans from "mild" – characterized by moderate intellectual and adaptive difficulties – to "profound". In this latter case, the intricacy of the impairments does not allow independent living, with symptoms including global aspects of cognitive and social abilities. For a detailed account of symptomatology in these disorders, please refer to the DSM-5 manual.

One key feature of NDDs is their comorbidity, that is, when two or more of these conditions are observed together. Notably, individuals with intellectual disability (ID) exhibit a high rate of comorbidity with autism spectrum disorder (ASD). ID is characterized by deficiencies in both cognitive abilities and adaptive functions, whereas ASD is defined by persistent deficits in social communication and social interactions, as well as by the presence of repetitive behaviors. While retaining the obvious diagnostic distinctions between these disorders, it is important to consider that the crosstalk between ID and ASD is great; indeed, symptoms associated with one diagnosis often "spill" into the other. This similarity exists beyond the

behavioral issues, and extends to the common cellular pathways involved in their etiopathology[2], through the potential development of future psychopathologies. Extensive chapters dedicated to the relationship between ID and ASD can be found in[3,4]. Remarkably, recent studies focused on the functioning of the olfactory system in people with ID and ASD, observing impairments in recognizing social chemo signals and in the olfactory short-term habituation to novel odorants, thus establishing a link between the physiopathology of these diseases and the computations within this sensory pathway[5,6].

It is important to note that ID-ASD are multifaceted diseases that involve, in their etiology, genetic predisposition, environmental insults, and developmental vulnerability[7]. Regarding the genetic causes, as researchers strove to find single-gene causes that would lead to ID-ASD, Chromosome X has become a main focus of research because of the observed unbalanced sex ratio of 1.3-1.4 to 1 for males to females with ID[8]. Moreover, according to the SFARI gene database, an increasing number of genes located on the X Chromosome is considered a "strong candidate" to be implicated in ASD (please refer to: https://gene.sfari.org/database/gene-scoring/). The function of such genes usually includes synaptic formation and transmission, as well as differentiation of neural and supporting cells of the central nervous system[9,10]. Prenatal causes of ID-ASD include congenital infections (such as cytomegalovirus, toxoplasmosis, herpes), prolonged maternal fever during the first trimester, exposure to toxic agents and/or alcohol, and so on[11,12]. Finally, a minority of cases can be accounted for by environmental factors such as pollution, the presence of particular metals within an area, the geographical remoteness of where the subjects live[5]. In summary, these results provide a more nuanced and complex picture of these disorders than once thought.

X-linked intellectual disabilities and OPHN1.

Influential works that traced a trajectory between X-linked genes in cognition and intellectual disability appeared as early as 1972[13]. Historically, the first XLID-associated gene to be discovered has been the *FMR1*, linked with the Fragile X syndrome – the most prevalent form of ID[14]. Since the first discovery, numerous additional XLID-associated genes have been identified, and research has focused on elucidating the functional roles of their protein products. Conversely, much less is known about the function of genes that are mutated in non-syndromic XLID, as their discovery is a more recent development. In this sense, identifying the role of these genes could offer crucial insights into fundamental aspects of neuronal function. A possible starting point to dissect which cellular mechanisms are responsible for such phenomena is the fact that several of these identified XLID genes directly interact with Rho-GTPases[15]. Rho GTPases constitute a family of small GTP-binding proteins that function as molecular switches: indeed, their key feature is the ability to switch between a GDP-bound (*inactive*) state to a GTP-bound (*active*) state. This switching is tightly regulated by a) nucleotide exchange factors (GEFs), which promote the exchange of GDP for GTP, and b) GTPase-activating proteins (GAPs), which accelerate the hydrolysis of GTP to GDP, returning the GTPase to its inactive state. Additionally, GDP dissociation inhibitor (GDI) maintains Rho-GTPase bound to GDP, thereby retaining its inactive state within the cytosol. Eventually, Rho GTPases exert their cellular effects by interacting with a variety of downstream effector proteins.

In which neuronal processes are GTPases involved? During development, neurons extend two classes of processes: an axon for transmitting outputs, and multiple dendrites for receiving inputs. Once this neuronal polarity is established, the axon navigates to locate its target, while the dendrites undergo extensive growth and branching. These processes necessitate precise regulation of both neuronal

morphogenesis and migration. Rho GTPases play an integral role in orchestrating all the above-mentioned processes: firstly, these proteins govern the outgrowth and retraction of axons during development, actively guiding the trajectory of growing axons[16]. Secondly, Rho GTPases dynamically influence the promotion or inhibition of dendritic growth[17]. While such dysregulations have been well characterized, an obvious question holds: how do they lead to intellectual disability? An initial insight might come from those genes directly involved in cellular signaling through Rho GTPases. Among such genes, there are *PAK3*, *ARHGEF6*, and *OPHN1*. The first encodes the relative PAK3 protein, which exerts downstream effects on various Rho GTPases, influencing actin cytoskeleton remodeling and gene expression[18]; the second one encodes αPIX, serving as a GEF for several Rho GTPases[19]; finally, *OPHN1* encodes oligophrenin-1, functioning as a Rho-GAP, thereby stimulating GTPase activity of numerous proteins[20]. Remarkably, from a morphological point of view, these genes' functional role mirrors findings from Golgi studies on infants and adults suffering from ID[21]. However, a first clue to why mutations in this class of genes lead to ID emerged from the study of OPHN1: when knocked down, it results in a reduction in the length of dendritic spines and an elevation in the activity of RhoA and Rho-kinase – namely, another GTPase and its effector protein[22]. Moreover, it has been demonstrated that OPHN1 binds to Homer, a family of scaffolding proteins forming the postsynaptic density (PSD), a structure that is important for the organization and function of excitatory synapses[23]. To summarize, Rho GTPases integrate numerous signaling pathways regarding neuronal morphogenesis – especially, dendritic spine morphogenesis and plasticity. Dendrites hold significance for synaptic integration, as they are responsible for receiving the majority of excitatory glutamatergic synaptic transmission, and thus they are of major importance also for synaptic plasticity[24]. Given these premises, it is likely that abnormalities in these structures will eventually lead to impairments in information processing at the network level.

OPHN1.

OPHN1 is located on the distal arm of the X chromosome; the precise location can be specified as Xq12. OPHN1 encodes the oligophrenin-1 protein, a Rho GTPase activating protein (Rho GAP), which is primarily expressed in neuronal and non-neuronal cells, and especially in those areas that exhibit a particularly high degree of plasticity – such as the hippocampus, the neocortex, and the olfactory bulb[25]. Oligophrenin-1 negatively regulates Rho GTPases: the current hypothesis suggests that it accelerates the hydrolysis of GTP to GDP, making it possible for Rho GTPases to switch from the active to the inactive form.

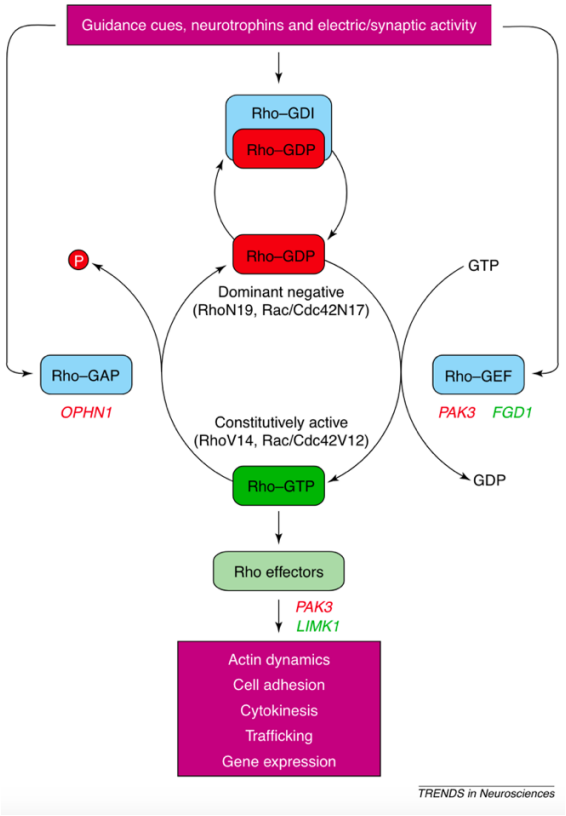

Figure 1. **Regulation of Rho GTPase activity and downstream signaling.** Rho GTPases act as molecular switches. Rho proteins are activated by guanine nucleotide exchange factors (GEFs), which mediate the exchange of GTP for GDP. Inactivation occurs through hydrolysis of the bound GTP by the intrinsic GTPase activity of the protein and is stimulated by GTPase-activating proteins (GAPs). GDP-bound Rho proteins are sequestered in the cytoplasm by guanine dissociation inhibitor (GDI) proteins, which prolong inactivation. Binding of GTP enables interaction with downstream effectors, which are often activated by release from intramolecular autoinhibition. Image from [15]; for a detailed account of Rho GTPases please refer to Aelst S. V.[26].

As previously mentioned, the absence or reduction of OPHN1 triggers an increase in RhoA activity, setting off a chain of events. RhoA, a distinct Rho GTPase protein, in turn modulates several effector proteins: among them, ROCK1 (Rho-associated, coiled-coil containing protein kinase 1) has been extensively studied. The upregulation of RhoA activity leads to a subsequent increase in ROCK1 signaling. Consequently, events occurring in this condition include the effects already discussed in the broader context of Rho-GTPases, but RhoA and ROCK1 are specifically involved in actin cytoskeleton remodeling and cell contraction[27]. Solid evidence indicates that OPHN1 mutations affect the structure of the postsynaptic density, as well as spine and dendrite morphology resulting in disrupted synaptic function and integration[23,28]. Nevertheless, its contribution is not limited to postsynaptic areas. OPHN1 has indeed been localized in pre-synaptic sites within axonal boutons marked by synaptophysin[22], and subsequent experiments have shown disruptions in the cycling of synaptic vesicles at the hippocampal level following OPHN1 knockdown[28]. Furthermore, Kasri et al.[29] demonstrated that OPHN1 plays a pivotal role in shaping the maturation and plasticity of excitatory synaptic function by influencing the stability of AMPA receptors. Specifically, OPHN1 undergoes recruitment or stabilization within dendritic spines in response to spontaneous activity, triggered by the activation of NMDA receptors (NMDARs). This, in turn, mobilizes the OPHN1 signaling pathway, steering the activity-dependent synaptic integration, and ensuring the stability of AMPA receptors, along with the preservation of spine structure[29]. As a result, this regulatory mechanism promotes the maturation and adaptability of synapses. Reduced or compromised OPHN1 signaling results in instability within synaptic AMPARs and alterations in spine structure, leading to a disturbance in plasticity and eventual depletion of synapses and NMDARs. Overall, these results prove that OPHN1 has a multifactorial role – it is critically involved in both the correct development of brain structure and brain function, at the pre- and post-synaptic

level, in excitatory synapses. Critically, recent investigations have elucidated the role of OPHN1 in modulating also inhibitory circuitry. In a recent study, mice carrying a null mutation of OPHN1 (i.e., ophn1$^{-/y}$) exhibited a notable decrease in the population of adult-generated inhibitory interneurons within the olfactory bulb. Interestingly, these impaired interneurons also exhibited an increased prevalence of filopodia-like spines, which are typical protrusions seen in young and immature neurons and altered synaptic function[30]. Additionally, it has been demonstrated the involvement of Cl^- homeostasis in migrating neuroblasts from the subventricular zone (SVZ) towards the olfactory bulb in ophn1$^{-/y}$ mice[31]. Lastly, ophn1$^{-/y}$ mice manifest epileptiform alterations in the hippocampus, often correlated with modifications in interneurons positive for parvalbumin, somatostatin, and neuropeptide Y-[32]. These results hold significance in light of the consolidated literature emphasizing the crucial role of inhibitory circuitry in the potential onset of neurodevelopmental and psychiatric disorders[33].

The development of a mouse model lacking OPHN1 traces back to 2007[34], and subsequent investigations have yielded a partial characterization of its behavioral phenotype. Notably, ophn1$^{-/y}$ mice show specific impairments in tasks involving spatial learning, and they exhibit novelty-driven hyperactivity. Moreover, ophn1$^{-/y}$ mice demonstrate impaired social behavior, and an increased tendency towards helpless behavior when faced with uncontrollable stress[35]. Ultimately, additional research seeking to better characterize the functional outcome of OPHN1 is needed.

The olfactory system.

The olfactory system (OS) is responsible for the detection and processing of odorants, small organic volatile molecules present in the air. This system is crucial for the perception of smells and plays a fundamental role in various physiological and behavioral responses. The Mouse OS can be divided into two subsystems: the

main olfactory system (MOS) and the vomeronasal system (VNS). The MOS processes olfactory signals from the main olfactory epithelium (MOE) to the telencephalon, passing through the main olfactory bulb (MOB). In contrast, the VNS primarily responds to pheromones, non-volatile molecules present in biological fluids, detected by the vomeronasal organ (VNO) and directly targets the accessory olfactory bulb (AOB). The functional role of the VNS will not be addressed in this context, as it is out of the focus of this Ph.D. project. Ultimately, both systems project back to the olfactory bulbs.

Odor detection initiates within the olfactory epithelium, localized in the nasal cavity. Olfactory sensory neurons, which are specialized neurons situated in the olfactory epithelium, express olfactory receptors on their cilia – hair-like projections stemming from the knob, i.e., the globous end of the apical dendrite of sensory neurons. Odorant receptors are G protein-coupled receptors which – upon odor binding – undergo conformational changes leading to an interaction with $G\alpha_{olf}$, the α-subunit of a heterotrimeric G protein. This causes the release of a guanosine triphosphate (GTP)-coupled $G\alpha_{olf}$, which in turn activates adenylyl cyclase III, resulting in increase in cAMP level. Cyclic AMP in turn binds to cyclic nucleotide-gated channels, causing an influx of Na^+ and Ca^{2+}. The intracellular increase of Ca^{2+} activates Ca^{2+}-dependent Cl^- channels, leading to depolarization and – eventually – to an action potential[36]. In the mouse genome there are more than 1000 OR genes encoding different types of OR. Humans have a similar number of genes encoding odorant receptors, although about 60% are pseudogenes. Therefore, humans have about 300-400 functional odorant receptor genes. Noteworthy each olfactory sensory neurons express only one type of odorant receptor[37].

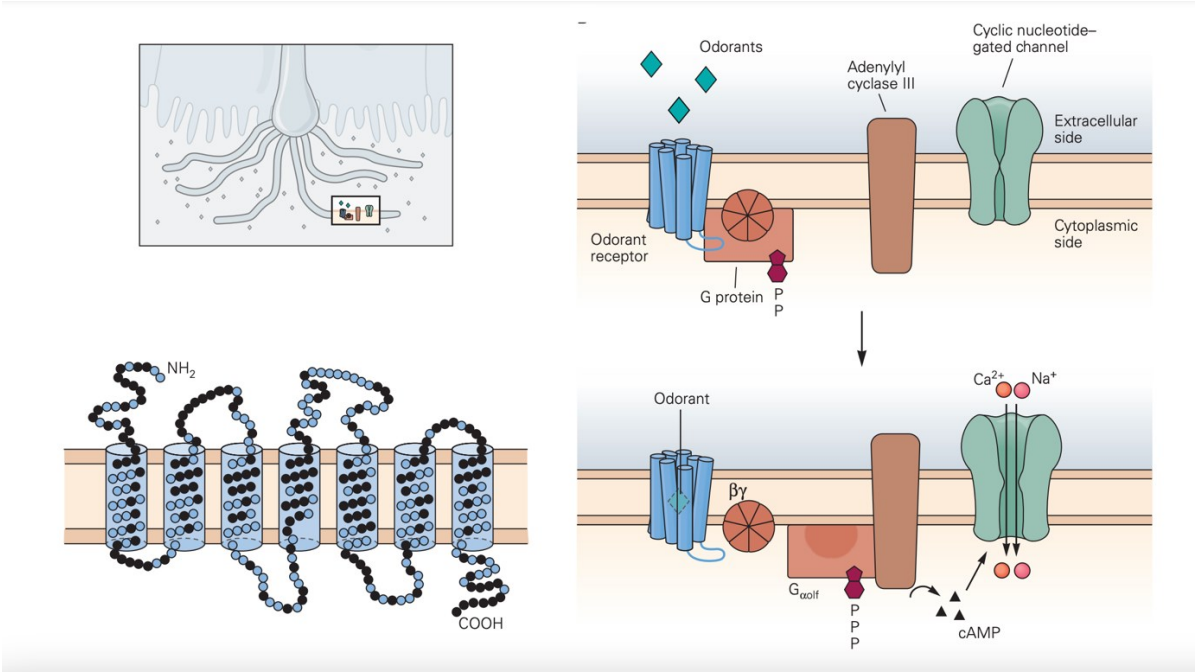

Figure 2. **Odorant receptors.** Bottom left) Odorant receptors have seven transmembrane domains characteristic of G protein-coupled receptors. Top right) The binding of an odorant causes the odorant receptor to interact with the $G\alpha_{olf}$, the α-subunit of a heterotrimeric G protein. This causes the release of a guanosine triphosphate (GTP)-coupled $G\alpha_{olf}$, which stimulates adenylyl cyclase III, leading to an increase in cAMP activity, which in turn induces the opening of cyclic nucleotide-gated cation channels, causing cation influx and changes in membrane potential in the ciliary membrane. Adapted text and image from Principles of Neural Science, 6th edition.

From the olfactory epithelium, olfactory signals reach the olfactory bulb, the first relay station where olfactory information is processed. Output neurons of the olfactory bulb project to higher brain areas, such as the piriform cortex, the anterior olfactory nucleus and the olfactory tubercle. Interestingly, part of the monosynaptic outputs from the olfactory bulb project directly to non-olfactory-related areas, such as the amygdala, the entorhinal cortex, and the prefrontal cortex. All these brain regions are involved in processing emotional and memory aspects of sensory information.

The olfactory bulb can therefore be seen as a hub connected to several sensory and cognitive higher brain areas. Owing to these extensive associations with higher brain regions, the olfactory system stands as a valuable paradigm for investigating not just perception but also cognitive functions.

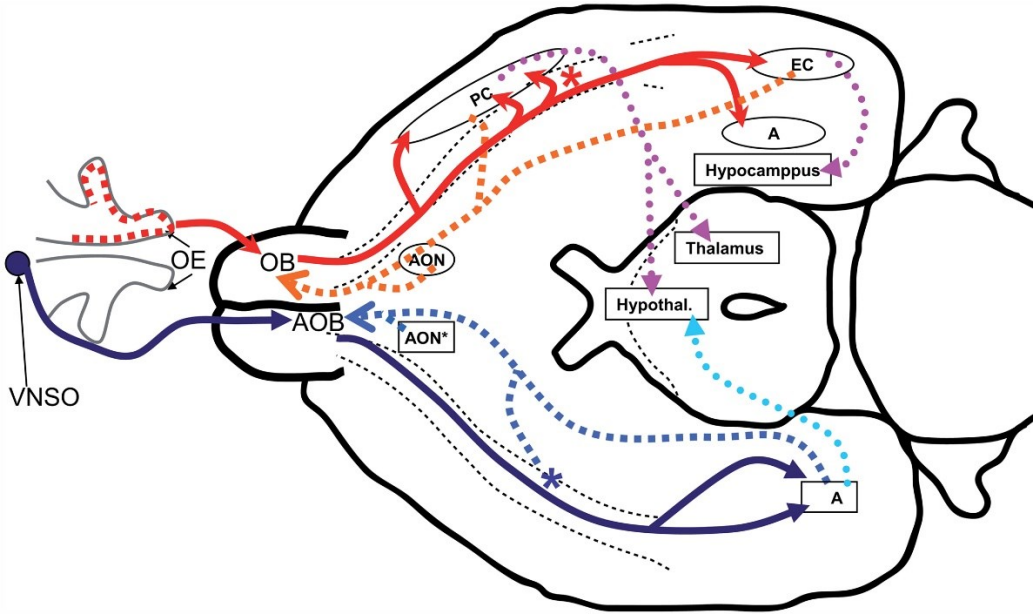

Figure 3. **Schematic of the olfactory system and connected brain areas**. The axons from the OSNs project to the olfactory bulb (OB), forming the olfactory nerve. The projection neurons from the OB send their axons (the lateral olfactory tract, LOT) to the different structures of the olfactory cortex, among them the anterior olfactory nucleus (AON), the olfactory tubercule, the piriform cortex (PC), the amygdala (A) and the entorhinal cortex (EC). In both cases, the olfactory nerve and the LOT are represented with gross red curved arrows. Neurons from the olfactory cortex and the nLOT project back to the OB (gross orange curved arrows). Main intracortical connections (violet dotted arrows) are towards parts of the neocortex, hippocampus, thalamus and the hypothalamus, as well as to the neocortex. The axons arising from the vomeronasal organ (VNSO) form the vomeronasal nerve and project to the accessory olfactory bulb (AOB). Image from De Castro et al.[38]

The olfactory bulb.

The olfactory bulb stands out as a prominent structure in the mouse forebrain. It presents a well-layered structure, resembling the cerebral cortex in many aspects, and its internal components may be broken down into three categories: input, output, and intrinsic structures. Starting from the outermost layer, the olfactory nerve (ON) layer, serves as the main input structure: here, axons from olfactory sensory neurons form the olfactory nerve running along this superficial layer of the OB. Notably, olfactory sensory neurons constantly regenerate, as they derive from stem cells in the olfactory epithelium. Each olfactory sensory neuron expresses only a single type of odorant receptor[37]. In contrast to most sensory modalities, the peripheral sheet, i.e., the olfactory epithelium, exhibits only a coarse topographic

organization, being the olfactory sensory neurons scattered around the epithelium[39–41]. However, a specific topographic organization is reached in the olfactory bulb, where olfactory sensory neurons expressing the same olfactory receptor converge to form glomeruli in distinct locations of the olfactory bulb itself[42–44]. Glomeruli are spheric structures of neuropil where olfactory sensory neurons' axons form synapses with the postsynaptic cells of the olfactory bulb. The alignment of glomeruli forms the glomerular layer. The mitral cell layer sits ~300 μm below the glomerular layer, and it is occupied by the soma of mitral cells (MCs) and a subpopulation of tufted cells (TCs): together, they represent the major output neurons of the olfactory bulb. Notably, every M/T cell extends their apical dendrites in a single glomerulus. As a result of this anatomical connection, olfactory information carried by olfactory sensory neurons expressing the same olfactory receptor converge on specific glomeruli and it is then processed by the complement of M/T cells connected to that very glomerulus. In this sense, the glomerulus can be seen as a functional unit encoding sensory information.

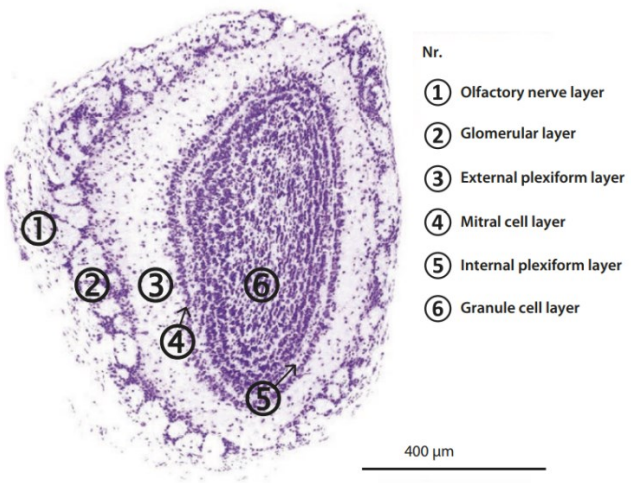

Figure 4. **Anatomy of the OB**. Nissl stain of a coronal section of the olfactory bulb. Its well-layered structure is visible from the staining, from the outermost layer (olfactory nerve layer) to the innermost one (granule cell layer). Image from Schröder et al.[45].

M/Ts form dendro-dendritic synapses with the lateral dendrites of the granule cells, the principal inhibitory interneurons of the olfactory bulb. These M/Tc-GC

synapses form a functional loop that shapes the firing pattern of the mitral tufted cells[46], providing lateral inhibition and contributing to generating oscillations in the olfactory bulb. Surrounding each glomerulus, there is a heterogeneous population of neurons comprising three distinct cell types: the periglomerular (PG) cells, the superficial short-axon (sSa) cells and the external tufted (ET) cells – together with glial cells. For simplicity, such cells are often referred to as juxtaglomerular (JG) cells. Juxtaglomerular cells exert the first modulatory control on the incoming sensory information at the glomerular level. Ultimately, in the glomerular layer, odorants are represented by a spatial pattern of activated glomeruli[47–49], and such representation is further processed in the olfactory bulb at the level of the mitral cell layer by means of lateral inhibition with the granule cells. Eventually, the information is sent to higher brain areas.

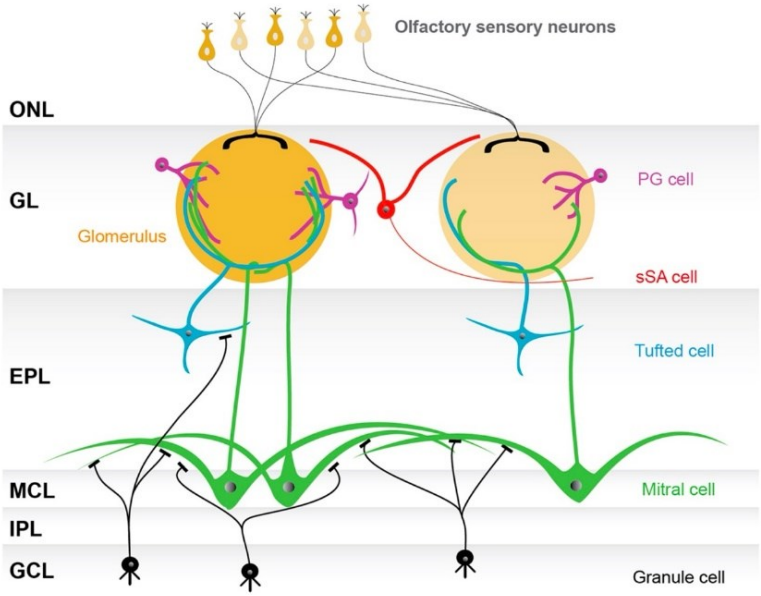

Figure 5. **Schematics of OB connectivity.** A schematic of how the principal cells of the OB are connected, from the outermost glomerular layer (GL) that contains axon terminals of the OSNs, M/T cells' dendrites and juxtaglomerular cells, to the innermost one, the granule cell layer (GCL) containing granule cells' somata. In the central layers of the OB its pyramidal neurons (M/T cells) have their cell bodies and make dendrodendritic synaptic connections with the GCs. Image from Nagayama et al.[50].

Neuronal oscillations.

The term "neuronal oscillations" refers to rhythmic or repetitive patterns generated at the level of the central nervous system. This patterning of neuronal activity is a ubiquitous phenomenon across biological systems, and it is known to be involved in the processing of sensory, cognitive, and motor processes[51,52]. Brain oscillations are usually measured at the extracellular level, at different scales. Oscillations have been observed when recorded from the scalp EEG, from the cortical surface (electrocorticogram, ECoG), or even by placing small electrodes in the given brain area (local field potentials, LFP). Even though the exact source of such signal is not fully understood, some of the contributors to such extracellular currents have been well described[53]. The origin of neuronal oscillations is manifold and involves both micro- and macroscopic processes. From the microscopic standpoint, the neuronal membrane possesses intrinsic excitability properties that contribute to its ability to generate rhythmic activity[54]. Indeed, several biophysical studies have pointed out how several neuronal cell types possess physical properties that enable them to have frequency preferences, making them capable of either generating spontaneous membrane-voltage oscillations, or respond best to stimuli within a narrow frequency band, i.e. to resonate[55,56]. This oscillatory activity is regulated by several membrane properties, including ion channels' conductance, and membrane potential thresholds. Nevertheless, synaptic activity is the main contributor to the generation of neuronal oscillations. Neurons receive input from thousands of other neurons through excitatory and inhibitory synapses. These multitude of excitatory and inhibitory inputs are integrated over time, and their temporal as well as their spatial summation leads to the generation of complex patterns of activity – that in the proper conditions lead to the generation of the neuronal oscillations. The neuronal architecture supporting a given network is composed of two major cell types: excitatory principal neurons, and inhibitory interneurons. Given these premises, just three types of networks are possible,

namely recurrent excitatory or inhibitory network (E-E or I-I), and feedback loops between excitatory neurons and inhibitory interneurons (E-I). E-E connections contribute to the synchronization of neural activity because – as neurons receive excitatory inputs from their neighbors – the network can exhibit coordinated firing patterns. The feedback loops formed by recurrent excitatory connections (E-E) can lead to the amplification of specific oscillatory frequencies, depending on the distinct band-pass filtering properties of the neurons[57,58]. Recurrent excitatory connections are often found within local circuits, where neurons form synapses with nearby regions, and such connections exist within a cortical layer or between different layers. Similarly, I-I networks involve the release of inhibitory neurotransmitters (in particular, GABA) by fast-spiking interneurons, binding to ionotropic receptors (in particular, $GABA_A$), allowing for Cl^- influx in the cell. Such recurrent networks have been associated with the generation of fast neuronal oscillations in the hippocampus (~20—80 Hz), providing a mechanism for synchronized oscillations in sparsely connected networks of inhibitory interneurons[59]. Moreover, the existence of such recurrent networks has been proven even in absence of glutamate-regulated synaptic transmission, when AMPA and NMDA receptors were blocked[60,61]. The mechanisms governing E-I feedback loops have been described fairly well: in this case, an oscillatory cycle begins when the excitatory drive of principal neurons directed towards inhibitory interneurons triggers their activation; this recruited inhibition tears down the ongoing excitation. As the excitation slowly vanishes, the network is ready to start a new oscillatory cycle[62,63].

Neuronal oscillations cover several orders of magnitude in the frequency domain – from the infra-slow (0.01—0.1 Hz), to the ultrafast oscillations (faster than >500 Hz). This classification does not indicate the physiological function of the oscillations nor its neuronal origin. Each oscillation has a distinct physiological and functional significance, even though a detailed taxonomy does not exist, and the

attempts that have been made so far have focused on the frequency band of these rhythms rather than on their mechanisms and functional significance.

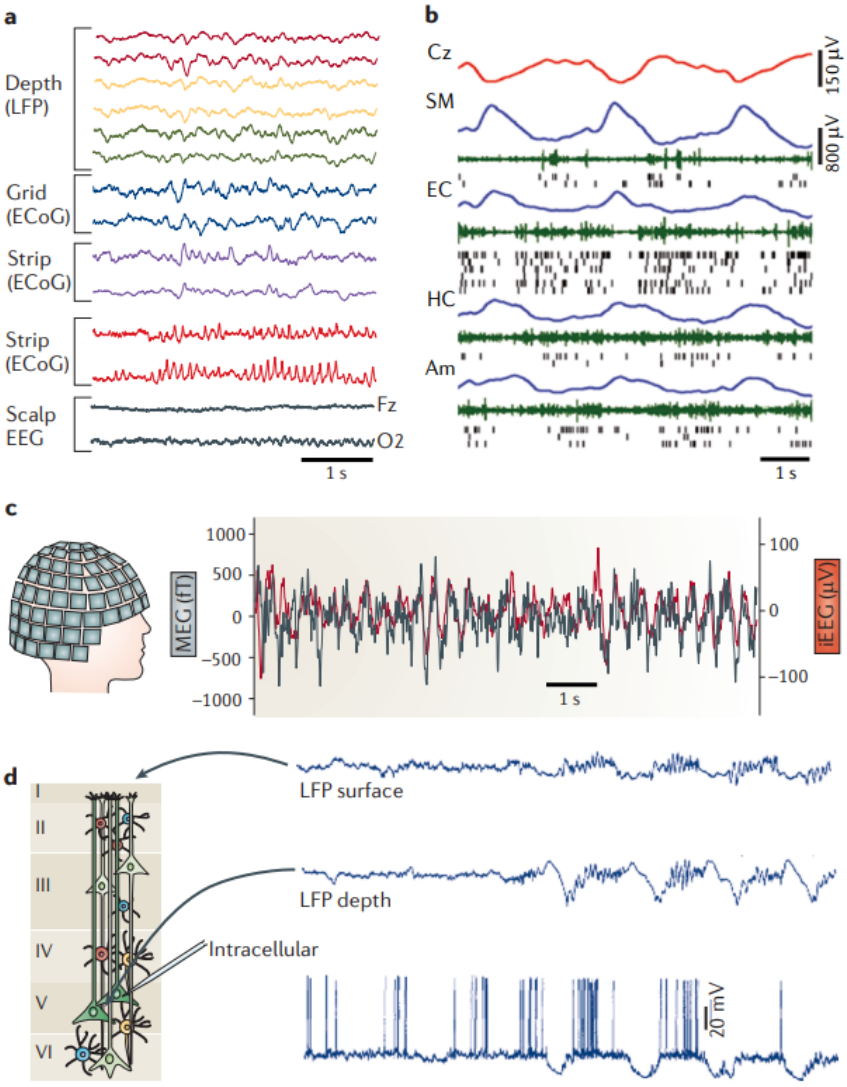

Figure 6. **Extracellular currents with different recording techniques.** A) Simultaneous recordings from three depth electrodes (two selected sites each) in the left amygdala and hippocampus (measuring the LFP); a subdural grid electrode array placed over the lateral left temporal cortex (measuring the electrocorticogram (ECoG); two four-contact strips placed under the inferior temporal surface (measuring the ECoG); an eight-contact strip placed over the left orbitofrontal surface (measuring the ECoG); and scalp electroencephalography (EEG) in a single patient. B) A 6s epoch of slow waves recorded by scalp EEG, and LFP recorded by depth electrodes placed in the deep layers of the supplementary motor area (SM) and entorhinal cortex (EC), hippocampus (HC) and amygdala (Am). C) Simultaneously recorded magnetoencephalogram (MEG; black) and depth EEG (red). D) Simultaneously recorded LFP traces from the superficial ('surface') and deep ('depth') layers of the motor cortex in an anesthetized cat and an intracellular trace from a layer 5 pyramidal neuron. Text and figures adapted from Buzsaki et al.[53].

When oscillations are integrated over longer timescales, they tend to follow the so-called "power law", according to which the power distribution of the various

frequencies is distributed according to a 1/f appearance. This observation suggests the involvement of large-scale functional networks in slow changes of membrane potential, while faster oscillations asynchronously occur in local networks comprising a relatively low number of neurons of fluctuations in membrane[64]. Nevertheless, when the brain is engaged in sensory, cognitive, or motor tasks, the power distribution could peak in distinct – more or less narrow – frequency bands[57,65]. Such a result suggests that brain rhythms, underlie different neuronal computations in specific brain regions during a given time window. Moreover, different frequencies may co-occur in response to a sensory stimulus, or while carrying out a cognitive or a motor task – often, in these cases the phase of slower oscillations hierarchically guides the power of the faster ones[52,66,67]. The functional interplay between the functional coupling of different brain oscillations is at the core of extensive current research.

Among the most widely studied oscillations there are the ones appearing in the theta band (4—8 Hz), that are observed across the brain in both cortical and subcortical structures. Research concerning the role of the theta oscillations in the hippocampus during spatial navigation tasks has paved the way to link oscillations in distinct frequency bands to a precise cognitive function – in this case, memory formation and retrieval[68,69]. Theta oscillations have also been observed in cortical areas of the human brain during task related to working-memory[70] and in the mouse olfactory bulb, coupled to respiratory rhythms[71,72].

Beta oscillations (15—35 Hz) were discovered in the human somatosensory cortex by the pioneering studies of Hans Berger[73]. Evidence indicates that beta oscillations become particularly prominent during the preparation of a movement, while they vanish as soon as the actual movement begins. In general, beta oscillations coordinate the precise timing of the neurons within the motor system[74].

Gamma oscillations (20—80 Hz) are fast neuronal rhythms produced within local brain networks. Typically, when a neuronal group is activated – wherever the specific brain region and independent of the sensory modality – it will start oscillating within this frequency band[62,64,75–77]. Moreover, gamma rhythms are thought to support attentional control processes, especially in frontal and parietal networks of the human and non-human brain[78]. Regardless, the functional role of gamma oscillations goes beyond attentive mechanisms and sensory-motor processes, but pertains the very processes through which information is integrated and distributed in the brain.

Neuronal oscillations captured by LFPs primarily reflect the collective electrical activity of local neuronal populations, i.e., the synchronized synaptic currents generated by a large number of neurons in a given region close to the recording electrode. Brain oscillations also allow the study of temporal connectivity between neuronal assemblies, such as their coherence and their phase relationship, providing insights into how information is processed and transmitted across brain regions. Therefore, neuronal oscillations are advantageous for understanding network-level interactions and dynamics.

Mechanisms of gamma oscillations.

Neurons engage within the gamma frequency band in response to sensory stimuli[64,79]. Basically, neuronal *gamma* oscillations rely on excitatory-inhibitory (E-I) feedback loops, where principal excitatory neurons interact with inhibitory interneurons. What is really necessary for this oscillation to be observed is the presence of inhibitory interneurons, which play a fundamental role in the generation of gamma-band synchrony, as it is known that they are capable of engaging in rhythmic gamma oscillations and sustain them even in the absence of principal neurons[80,81]. The key phenomenon to understand the gamma-band synchronization is the phase relation that exists between the firing of the excitatory

neuron and the consequent activation of the inhibitory ones. Interneurons tend to fire a little after the principal cells, and this has been observed in different conditions[80,82]. What is the mechanism that regulates these network dynamics? In short, after the excitatory neuron fires, the gamma-band rhythmicity is imposed by the inhibitory interneurons with a little phase delay; during this ramping inhibition, no other excitatory neuron can fire. While inhibition starts to fade away, principal neurons can receive excitation again from sensory inputs, in turn commencing a new gamma cycle. One crucial feature to keep in mind for understanding how gamma oscillations work is that the greater the excitatory input, the sooner principal neurons will be able to fire with respect to the phase of the decaying inhibition[82]. A speculation for this peculiar process that transforms the incoming excitation into a relative spike timing with respect to the gamma cycle is to imagine the gamma cycle as a rapid, endlessly repeating winner-takes-all algorithm[62]. Excitatory neurons have a narrow temporal window in which they can fire – that is, during the fading phase of the gamma cycle. If they are not able to fire at that moment, they will not fire at all because of the subsequent local inhibition exerted over the whole network by inhibitory interneurons. This means that the neuron conducting the greatest excitatory input will not only be able to fire before with respect to the phase of the gamma cycle, but it will also make unlikely for other neurons to get activated. A likely consequence of this mechanism is to increase the signal-to-noise ratio, as weak responses are redundant and likely unnecessary, and to decrease the computational effort required by multiple action potentials. In this sense, from the point of view of the downstream neuron, the activity coming from all the upstream neurons within the same gamma cycle is considered as a single event, while the spikes falling before or after the time window of a putative gamma cycle, are seen as another one[51,64]. Importantly, if analyzed in this context, gamma oscillations can be intended as a sort of temporal reference frame to process the incoming sensory information, but they provide no

clue about the real nature of the excitation itself: they message that a putative local network has received some form of excitation, but in *what* such excitation consists depends on the external stimulus and the neuronal architecture processing it – that is, the brain region[83]. In this sense, recording transient increases in the gamma band in the LFPs of a distinct brain region may be a footprint of active operations within the local circuit[64]. In synthesis, a higher gamma power is often associated with increased neural processing and is observed in tasks requiring active processing of the sensory stimulus. This should not be confused with an increase in spiking activity, where individual neurons fire action potentials more frequently: spiking activity refers to a more general measure of neuronal excitability and it can occur across different frequency bands, not just in the gamma range. It reflects the overall level of neural activity in response to a stimulus or during a particular cognitive state.

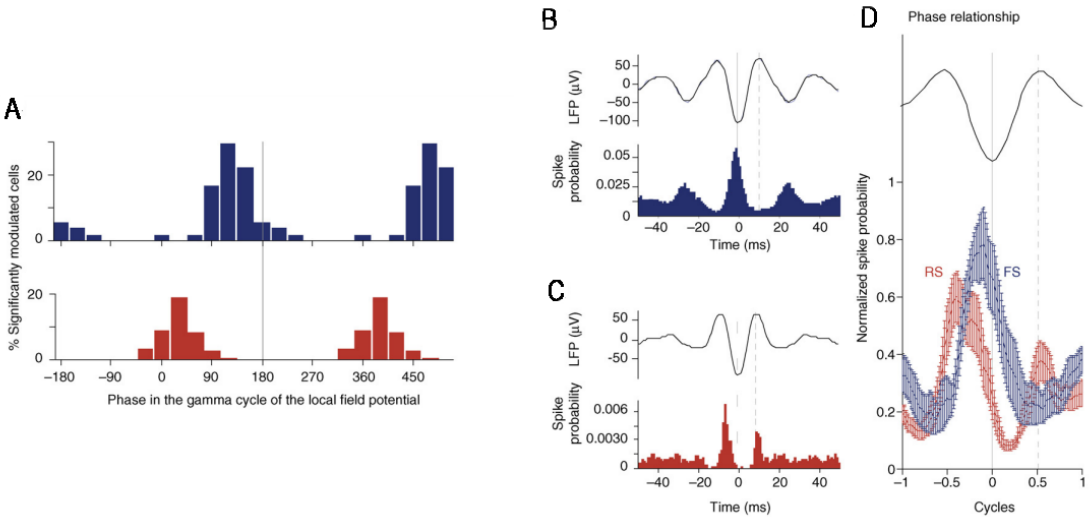

Figure 7. **Pyramidal cell–interneuron firing in the gamma cycle.** A) Recordings from the hippocampus of behaving rats. The vertical line indicates the moment of peaks in the gamma band-filtered LFP. Recorded spikes were sorted into interneuron spikes (blue) and pyramidal cell spikes (red). Results show the phase-locking of pyramidal cell firing to interneuron firing. B-D) Similar analyses conducted on the prefrontal cortex of an anesthetized ferret. D) Average normalized spike probability for the two cell classes. Adapted text and images from Fries[62].

Oscillations in the olfactory bulb.

The olfactory bulb exhibits a wide range of oscillations and is one of the brain areas where oscillations have been first characterized[84]. It is now widely recognized that these oscillatory patterns are generated by precise neuronal circuits and underpin distinct behaviors. In particular, three types of oscillations – occupying different frequency bands – have been characterized within the OB: theta, beta, and gamma.

Theta oscillations occupy the same frequency band of hippocampal theta oscillations (1—12 Hz), although their source and their role are completely different compared to the role and origin of hippocampal theta. In the olfactory bulb, theta oscillations are driven by sensory inputs, and they are also called "respiratory oscillations" as they track the breathing rhythm, which – in rodents – is around 1-4 Hz during the waking state, reaching up to 12 Hz while the animal explores novel odorants and performs odor discrimination tasks, with active sniffing. This oscillatory activity is mainly driven by the volley of sensory input coming from olfactory sensory neurons (OSNs) to the olfactory bulb. Evidence indicate that theta oscillations can be supported by the firing rate of the external tufted cells in the olfactory bulb. These two components are not mutually exclusive as several experimental and modeling studies suggest that theta oscillations are generated by sensory inputs at the glomerular layer of the OB[85,86]. There are also central components to the theta rhythms. For instance, the piriform cortex generates theta oscillations that can – in turn – exhibit alternate periods of coupling to olfactory bulb thetas; when mice are anesthetized, such coupling greatly decreases[87]. In some cases, this coherence also appears between theta in the hippocampus and the olfactory bulb: studies on phase coherence indicate that theta rhythms in the hippocampus may actually drive theta in the olfactory bulb during fast sniffing[88,89]. The contribution of higher brain areas to these brain oscillations is, however, little known and further investigations are required. Regardless, theta oscillation might

be a part of a greater network involving higher olfactory areas as well as hippocampal ones. They could represent two distinct processes, one connected to the inhalation phase of the sniffing cycle, and one to the exhalation phase. In the first part, theta rhythm may support the sensory acquisition of the olfactory stimuli (in this time, rarely do other rhythms appear in the LFP), while the latter seems to contain higher frequency rhythms probably related to the processing of the acquired information.

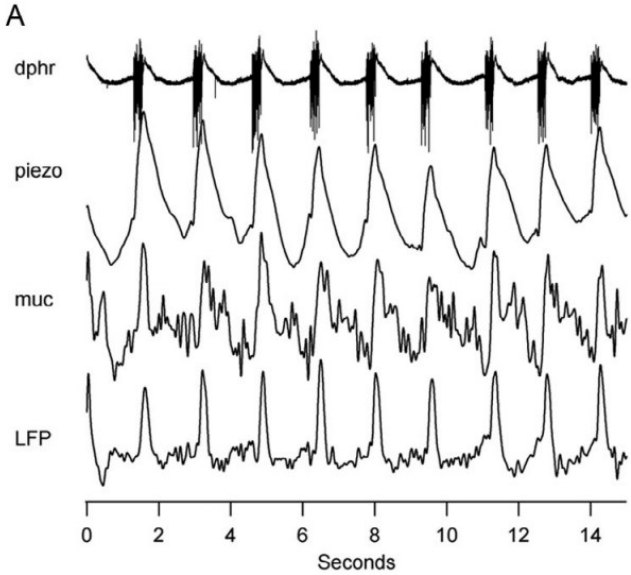

Figure 8. **Theta activity in the olfactory bulb with respect to respiratory activity**. From top to bottom: diaphragm EMG, airflow in the front of the nose, olfactory mucosa population and LFP from the OB of a rat. Image from Kay et al.[90].

On the other hand, beta oscillations (15—30 Hz) are generated in several cortical areas such as the piriform cortex, the entorhinal cortex and in the hippocampus and most prominently in the motor cortex and in the olfactory system. They remained undetected until recordings were conducted in awake animals, and their initial observation occurred in response to the olfactory stimulation of predator odor during sniffing[91,92]. Beta rhythms appear in several contexts: when animals learn to associate odorants during learning, during anticipation of odor stimuli as tuning signal for the OB when entorhinal inputs drive the OB[93,94]. Beta oscillations have been associated with motor behaviors during an olfactory reaching task, which reminds the role of beta oscillations in motor tasks in other brain areas[95]. Despite

the wide knowledge of the various physiological and behavioral contexts in which beta oscillations occur, their source is little known. Several pieces of evidence indicate that beta oscillations rely on the intact loop between the OB and higher brain areas to which the OB itself is monosynaptically connected – such as the PCx[93,96].

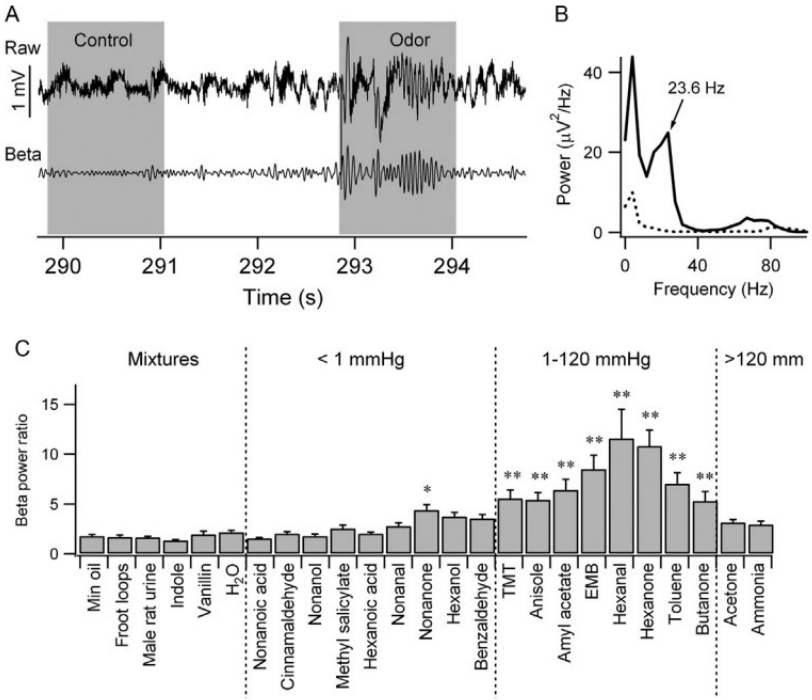

Figure 9. **Increase in beta oscillations during the presentation of high volatility odorants.** A) LFP of a rat during odor presentation; B) concurrent power spectra highlighting an increase in beta activity; C) relative beta power increase for a range of odorants. Highly volatile odorants are correlated to the highest increase in beta activity. Image from Lowry et al.[97].

Nonetheless, the mechanism through which M/T cells and GCs interact with pyramidal neurons of the PCx to generate the beta oscillations is not known, nor is it known whether specific subcellular types differently participate in this rhythm. The real function of beta oscillations is still unclear: in other sensory systems, beta rhythms often accompany the observation of an object to the actual movement required to reach it[98]. In accordance with this result, also rats performing odor-guided tasks in order to reach an object exhibit coherent patterns of beta oscillations across olfactory and motor areas[93,95].

Gamma oscillations (40—100 Hz) represent the most studied olfactory oscillations and resemble cortical gamma rhythms in many ways. They arise from an E-I feedback loop between principal neurons (M/T cells) and inhibitory GABAergic interneurons, the granule cells, of the OB. The schematics of their architecture in turn follow what happens at the cortical level, with sensory input heightening the activity of M/T cells which excite GCs through dendrodendritic synapses, which in turn inhibit M/T's lateral dendrites activity. In various studies it has been demonstrated that mitral cells fire typically with ~90 degrees with respect to the peak of gamma oscillations, suggesting that an increase in the LFP gamma might be generated by a more coordinated activity by mitral cells, while a lower LFP amplitude might reflect the activity of smaller of less coordinated cell assemblies[99]. As for other sensory systems, OB gamma oscillations are sensory-evoked rhythms generated in response to olfactory stimuli. Moreover, gamma oscillations exhibit a clear correlation with theta oscillations: in particular, they appear at the end of the inhalation period and extend during the whole expiratory phase[99]. Gamma oscillations occupy a broad frequency band, but they are usually divided in two sub-bands: the first one, the gamma1, occupies the upper band (70—100 Hz) of the gamma oscillations, and it is related to proper sensory-evoked mechanisms, while a second gamma oscillation – gamma2 – occupies the lower end of this frequency band (40—70 Hz) and it has been observed during alert immobility and grooming behaviors[99,100]. A more precise function of OB gamma oscillations might be related to fine odor discrimination. In particular, Beta3 mice (mice lacking the beta3 subunit of the $GABA_A$, and also having nonfunctional $GABA_A$ receptors on OB granule cells) exhibit extremely large gamma oscillations – probably due to the fact that local interneurons cannot be inhibited by other local GABAergic neurons. Beta3-knockout mice also exhibit a better fine odor discrimination, with respect to WT[101].

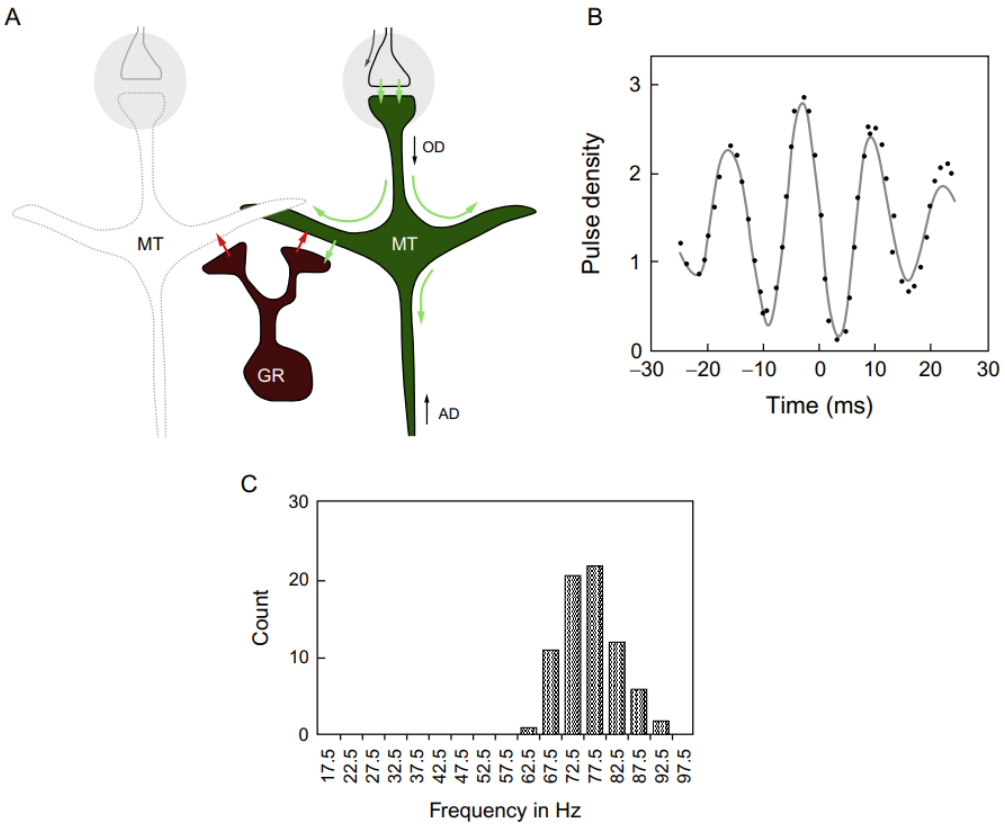

Figure 10. **Mechanisms of gamma oscillations in the OB.** A) Schematic of the circuit generating gamma oscillations. (MT, mitral/tufted cell; GR, granule cell; OD and AD, orthodromic and antidromic directions). B) Pulse probability density of multiunit activity based on the LFP signal depicts a gamma cycle. C) Frequency distribution of several OB recordings returns the gamma frequency band. Image from Rojas Libano et al. and Eeckmann et al.[100,102].

Recording neuronal population at cellular resolution with two-photon calcium imaging.

LFPs measurements bring some level of spatial ambiguity, making it impossible to define the exact cellular sources of the recorded signals. This distributed nature might obscure the contribution of each distinct cell type in network computations. A technique that proposes to overcome such limitation is two-photon calcium imaging[103]. Two-photon imaging allows the optical recording of hundreds of cells, expressing fluorescent proteins – with single-cell resolution – *in vivo*.

In brief, two-photon imaging works in this way: two low-energy photons are simultaneously absorbed to cause the transition of a fluorescent molecule towards

a higher vibration energy level. This is followed by the return to the fundamental energy level by releasing the absorbed energy as an emitted photon[103–105].

Two-photon microscopy allows for a better resolution and sensitivity to fluorescence signals, compared to the ordinary one-photon confocal microscopy. A remarkable property of two-photon microscopy is that since fluorescence depends on two independent events – i.e., the absorption of two photons –it is not linearly proportional to the excitation but depends on the second power of light intensity [105]. Because of this, fluorescence is emitted only in a restricted volume around the focal plane, reducing issues of phototoxicity and photobleaching. The usual excitation wavelengths used in two-photon microscopy are within the near-infrared spectrum (between 800 and 1000 m, and beyond), with better tissue penetration with respect to one-photon excitation. These distinctive features position two-photon imaging as an indispensable tool for recording hundreds of neurons with single-cell resolution, which represents the required substrate for computational analysis aimed at unraveling the dynamics of neuronal networks.

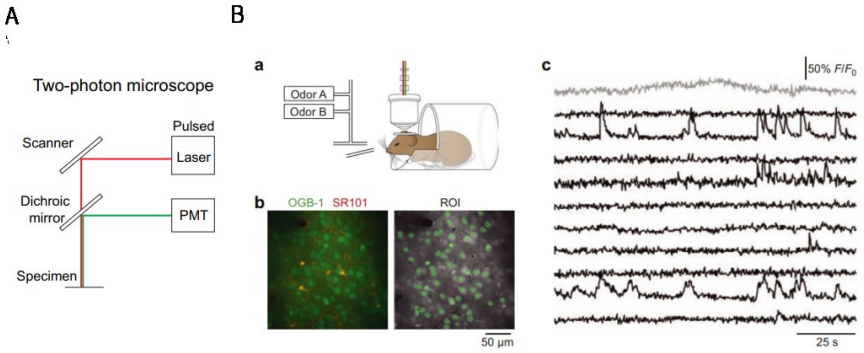

Figure 11. **A) Two-photon microscopy**. Two-photon microscopy using a pulsed near-IR laser suitable for two-photon microscopy. The excitation spot is steered across the specimen by a scanner. The emitted fluorescence is detected by a photomultiplier tube (PMT). **B) Imaging in the motor cortex of a head-fixed mouse engaged in an olfactory-related choice behavior with lick/no lick response**. Ba) Scheme of the experimental set-up showing a head-fixed mouse under a two-photon microscope while performing the task. Bb) Two-photon image of layer 2/3 cells. Left, overlay of sulforhodamine 101 (SR101, red) and Oregon Green BAPTA-1 AM (green). Bc) Example of spontaneous calcium traces from ten neurons (black) and one astrocyte (gray). Panels adapted from Grienberger et al., and Komiyama et al.[104,106].

Genetically encoded sensors as reporters of neuronal activity: calcium indicators.

Neuronal activity causes rapid changes in intracellular free calcium levels. This condition has been exploited to generate genetically-encoded fluorescent calcium indicators (GECIs) as a reporter of neuronal activity[107–109]. Namely, GECIs are designed to optically report the rise in calcium levels associated with the firing activity of population of neurons, with single-cell resolution. In addition, by genetic engineering, GECI can be targeted to a specific population of neurons or to subcellular domains to perform Ca^{2+} imaging in specific locations. Genetically encoded sensors for Ca^{2+} are typically composed of two main parts: a calcium-binding domain and a fluorescent protein. The calcium-binding domain is represented by a fragment of the Ca^{2+}-binding protein, calmodulin which undergoes conformational changes upon calcium binding. The other component is a fluorescent protein, mostly derived from green fluorescent protein (GFP). The most widely used genetically-encoded sensor for Ca^{2+}, GCaMP is based on a circular permutated green fluorescent protein (cGFP): the n-terminal of cGFP is linked to the M13 fragment of the light chain of myosin kinase, which is a target sequence for calmodulin, hence the name calmodulin-binding peptide (CBP), whereas the C-terminus of cGFP is linked to calmodulin. Ca^{2+}-dependent conformational changes of calmodulin propagate to the rest of the protein modulating the GFP chromophore environment.

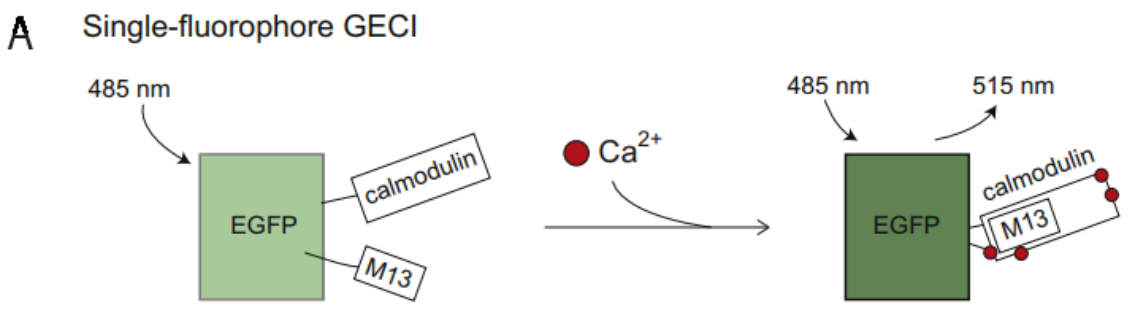

Figure 12. **Single fluorophore GECI.** After the binding of calcium to the GCaMP, conformational intramolecular changes lead to an increase in the emitted fluorescence. Image from Grienberger et al.[104].

Neuronal ensembles as building blocks of the neuronal code.

A recent advancement in discovering the structure underlying network dynamics in the brain has been the studies pertaining neuronal ensembles[110,111]. In brief, neuronal ensembles are groups of coactive neurons that appear in response to sensory stimuli and in spontaneous activity, in absence of sensory stimuli[112]. Neuronal ensembles have been proposed to be building blocks of functional circuits, and units of the neuronal code[113]. In this framework, neurons firing together represent organic units, coding for stimuli. This kind of topic is a common motif in neuroscience from the studies of Donald Hebb, who proposed its influential theory according to which neurons repeatedly – and simultaneously – activated, strengthen their connection [114]. This concept has been highly influential especially in the context of the discourse around memory and learning processes, founding experimental confirmation in biological processes such as long-term potentiation (LTP), depression (LTD) and spike-timing-dependent plasticity (STDP). Despite their similarity, Hebbian processes refer to learning processes *per se*, while neuronal ensembles have been observed even during spontaneous activity, showing dynamics resembling the evoked activity[111,112]. In this sense, neuronal ensembles do not represent Hebbian processes, but rather their consequence. Thanks to the development of two-photon calcium imaging, which

enables to record population of neurons, with cellular resolution *in vivo* researchers have been able to visualize such ensembles. Strikingly, further experiments have not only demonstrated the existence of neuronal ensembles, but also the possibility of artificially imprinting them following Hebbian paradigms[110]. These imprinted ensembles exhibit "pattern completion" properties, meaning that the activation of a few or even a single neuron being part of an ensemble triggers the activation of the whole group of cells composing the same ensemble[113,115]. Such processes had already been predicted by John Hopfield, who modeled these collective patterns that arise in a neural network as a result of neuron interactions: these properties would emerge from the network's overall spontaneous dynamics rather than being explicitly programmed, showcasing the system's ability to self-organize and exhibit complex functions[116]. Last, and most importantly, recent experiments have demonstrated a causal link between the stimulation of "pattern completion" neurons and an actual change in the behavior of the mouse[113,117–119]. Critically, so far experiments that probed the existence and the collective behavior of neuronal ensembles have only been conducted on cortical neurons, and especially in brain regions devoted to encoding visual sensory stimuli. The fact that neuronal ensembles should represent a general property of the brain might suggest other brain regions to exhibit this kind of behavior, at least the ones involved in primary transformations of external stimuli in other sensory modalities. Due to the relevance of neuronal ensembles in neuronal coding, it is not surprising that alterations in the ensembles have been observed in pathological states. Indeed, recent experiments have already demonstrated abnormally generated and recruited neuronal ensembles in different models of pathologies, such as epileptic seizures and schizophrenia [120,121]. There are no studies to date that have proved the existence of neuronal ensembles within the OB, and studies on models of ID-ASD are lacking too.

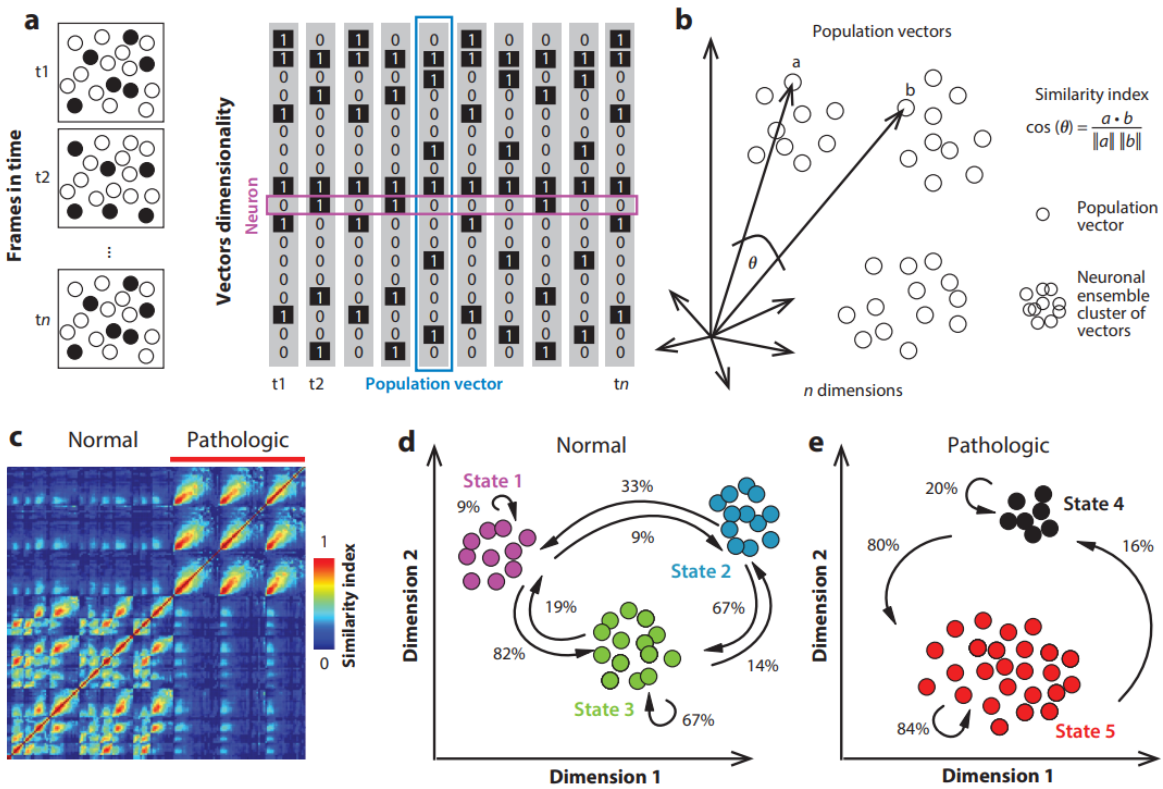

Figure 13. **Detection of neuronal ensembles using multidimensional population vectors.** A) Schematic representation of active neurons from calcium imaging data. (Left) Black filled circles show active neurons at different time frames. (Right) Binarized matrix of activity representing the overall population activity, where rows indicate individual neurons and columns indicate individual time points representing population vectors. “1” means that the neuron is active, while “0” that is not active. B) Population vectors representing the coactivation of neurons at a given time. Cosine similarity indicates the angle between population vectors. Thus, clustered population vectors define a neuronal ensemble. C) Similarity maps to visualize the angle between all population vectors. Repetitive structures in similarity maps represent neuronal ensembles activated at different times. D) Dimensionality reduction techniques and cluster analysis could be used to define and count neuronal ensembles. A neuronal ensemble is defined as a cluster of population vectors pointing in a similar direction. Arrows represent the transition probability between different network states. (e) During pathological conditions, neuronal ensembles are affected. Adapted text and image from Carrillo-Reid et al.[122].

Materials and methods.

Animals: All procedures adhered to the EU Directive 2010/63/EU for animal experiments and followed the ARRIVE guidelines. Experimental protocols received approval from the Italian Ministry of Health. Animals were housed in filtered cages in a temperature-controlled environment with a 12h dark/12h light cycle, and they had *ad libitum* access to water and food. Behavioral and LFP experiments were conducted on male OPHN1$^{-/y}$ (n = 7) animals and their wild-type (WT; n = 7) littermates (C57BL/6J background, The Jackson Laboratory, Stock No: 005304), at an age of a ≥ 8 weeks. For the two-photon Ca^{2+} experiment, separate groups of ophn1$^{-/y}$ animals and relative controls were used (WT, n = 6; ophn1$^{-/y}$, n = 6). All analyses were performed blind to the genotype.

Locomotion: Each animal was free to move within a 35 cm² arena for 40 minutes. The first 10 minutes were used for the habituation phase and discarded from the subsequent analysis of locomotion, which was performed on the remaining 30 minutes. The data reduction performed by OptiMouse (Carrillo-Reid et al., 2019) and subsequently analyzed with MATLAB comprised three phases: *Definition*, *Detection*, and *Analysis*.

- **Definition phase**: This phase begins by determining the actual size of the objects in the video through a calibration step that rescales pixel units to millimeters. Rectangular arenas are then defined for each animal and applied to each frame of the recording.

- **Detection phase**: This step involves frame-by-frame pose estimation of the animal. A median background image, created from all frames, is subtracted to provide an estimate of the arena without the mouse. At this point, visual inspection of the frames is required to ensure OptiMouse correctly detects the animal; in case it does not, the background subtraction thresholding can be manually adjusted. Once optimal thresholding is reached for each mouse, OptiMouse detects four landmarks on the mouse's body: the nose, the body center, the beginning of the tail, and the end of the tail. OptiMouse utilizes an algorithm that exploits the geodesic distance (i.e., the shortest route from the tail to the nose) to correctly detect the animal. For our purposes, only the body center – considered as the mouse's center of mass – has been used for the subsequent analyses.
- **Analysis phase**: After the detection phase, results are saved in a .mat file that contains a structure with all the relevant information. We conducted further analyses by extracting data from a variable called Res.pD.position_results.mouseCOM. This variable contains a 2xN array (where N represents the number of frames), with the x and y coordinates of the mouse's body for each frame in the session.

To calculate occupancy metrics, coordinates of the mouse (i.e. mouse's center of mass) were grouped in 2 mm^2 bins and the occupancy frequency was calculated for each mouse. Mice were then averaged over groups. The arena was divided into 16 quadrants: four central quadrants represented the center of the arena, while four quadrants located in the four corners represented the periphery of the arena.

Habituation-Dishabituation. Mice were placed in a 20 cm × 15 cm × 13 cm plexiglas cage without access to water or food for a 30-minute habituation period, prior to the behavioral task. During this time, a cotton swab soaked in double-

distilled water replaced the drinking bottle. During the behavioral experiment, a second water-soaked cotton swab was presented for 3 consecutive presentations (3 habituation trials) with 1-minute intervals between trials. Each presentation lasted 2 minutes. In the fourth trial (dishabituation trial), a cotton swab scented with a new odorant, in this case isoamyl acetate (ThermoFisher Scientific, CAS: 123-92-2) was exposed into the cage for 2 minutes. The new odorant was presented again with a cotton swab for 3 consecutive times, for 2 minutes per presentation, and a 1-minute interval between presentations. These same sequence of 3 presentations was applied to a third odorant: eugenol (ThermoFisher Scientific, CAS: 97-53-0). Odorants were diluted 1% *v/v* in mineral oil (ThermoFisher Scientific, CAS: 8042-47-5).

The investigation time – defined as the period of active sniffing with the nose in close proximity to the cotton swab – was measured within the 2 minutes of each trial. To prevent odor contamination, clean cages were used for each subject. All behavioral tests were conducted during the same daytime and video recorded with a camera (XIMEA XiQ, 30 frames per second, 2592 × 1944 pixels).

Surgery for LFPs recording. Animals were anesthetized using a mixture of Ketamine (Nimatek, 100mg/mL; Dechra, Nortwich, UK) and Rompun (Xylazine 2%, 0.06 mL/kg; Bio98, Milan, Italy) and placed on a thermostatic blanket in a custom stereotaxic frame A small stainless-steel screw was used as reference electrode placed above the cerebellum. A small hole was drilled in the skull above the olfactory bulb to insert a custom-made bipolar stainless-steel electrode (Advent, Stainless Steel Wire AISI316LVM, quadruple PTFE insulated, bare wire ø 0.125 mm). The bipolar electrode weas placed at the following stereotaxic coordinates: anterior = 800 μm, lateral = 500 μm, depth = 180 μm relative to the midline and inferior cerebral vein intersection. All components were connected to a fingerprint connector and fixed to the skull using dental cement (Paladur, AgnTho's, Lidingö, Sweden). After the surgery, mice received Tramadol (10 mg/kg, Formevet, Milan,

Italy) for pain relief and were maintained in their own cage under a heating lamp till full recovery from the anesthesia. Animals were then housed individually for three days to ensure complete recovery before commencing LFP recordings.

Local Field Potentials (LFPs) signal recording. The LFP signal was amplified using a mini head-stage preamplifier (NPI electronic GmbH, Tamm, Germany) and a 2-channel extracellular amplifier (EXT-02F NPI electronic Germany). The amplified signal underwent band-pass filtering (0.3–300 Hz; EXT-02F NPI electronic, Germany) and digitization at 10 kHz (DAQ: National Instruments; Austin, TX, USA). We recorded LFPs from both ophn1$^{-/y}$ and WT littermate control mice. Mice were free to move within a plexiglas arena measuring 35 cm × 35 cm × 40 cm, located inside a Faraday cage. Before recording, the mice were allowed to get accustomed to the environment for about 30 minutes. Each mouse underwent two recording sessions on two consecutive days, each lasting about 100 to 150 minutes. One recording was performed on day 1 in the morning, and the second record on the day 2 in the afternoon. During these recordings, mice were video recorded as described above.

LFP video analysis, pre-processing, and spectral analysis. Videos were manually reviewed with a software (MPC-HC, v1.9.5) to identify two behaviors: *resting* and *exploring*. We referred to "resting" when a mouse remained still for at least one minute in the arena, while "exploring" indicated a mouse moving around and investigating its surroundings, without engaging in other activities (i.e., burrowing, grooming, wagging the tail, jumping etc.) which were discarded from the analysis. To perform LFP analysis, we processed 15 minutes aggregated recording datasets.

The raw signal acquired at 10 kHz was filtered with a 5th order band-pass Butterworth filter in the 1–100 Hz range and then down-sampled at 250 Hz. To capture different spectral bands, we applied different band-pass filters: 1–12 Hz for

theta band, 15–35 Hz for beta band, 40–70 Hz for low gamma and 70–100 Hz for high gamma band. Power spectral density (PSD) of LFP was computed with Welch's method, with a mobile Hann window of 0.5 s and with 0.25 s overlap between windows, using the SciPy package for Python (https://www.scipy.org/, accessed on 1 August 2020). PSD was computed for each behavioral state (i.e., "resting" or "exploring") by averaging the spectra computed in each window. Spectrograms were calculated with the same Hann's window width and overlaps. To calculate the normalized power of the "exploring" tags and the "resting" ones with respect to the recording, first we calculated their power by means of a PSD; then, each point of such PSDs was divided by the total amount of LFP power in the recording. In this way, every animal – and every recording – was normalized over the power of the recording itself, so to avoid any potential bias in the normalization. Eventually, each animal was averaged for its two recordings.

Surgery for cranial window for two-photon calcium imaging. Mice were anesthetized using a mixture of ketamine (Nimatek, 100mg/mL; Dechra, Nortwich, UK) and Rompun (Xylazine 2%, 0.06 mL/kg) and placed on a thermostatic blanket in a custom-made stereotaxic frame. Adeno-associated viruses (AAVs) containing the calcium indicator GCaMP6s (pAAV9.Syn.GCaMP6s.WPRE.SV40, Addgene, Watertown, MA, USA, catalog number: 100843-AAV9) were bilaterally injected into each olfactory bulb (OB) at two distinct sites per OB, with each injection delivering 250 nL of AAV vector at a rate of 70 nL/min. The injection coordinates for the first site were as follows: anterior = 1.2 mm; lateral = 500 μm; depth = 400 μm, and for the second site: anterior = 800 μm; lateral = 500 μm; depth = 400 μm, relative to the intersection of the midline and the inferior cerebral vein. To ensure the well-being, animals were injected with post-operative analgesia (Tramadol, 10 mg/kg) immediately after the surgical procedure and were placed in a warm environment until complete recovery from anesthesia. Animals were then housed

in individual cages for at least two weeks to allow full expression of the calcium indicator.

Two-photon calcium imaging experiment. On the day of the experiment, the animals were anesthetized using a mixture of Ketamine (Nimatek, 100mg/mL; Dechra, Nortwich, UK) and Rompun (Xylazine 2%, 0.06 mL/kg; Bio98, Milan, Italy), and placed on the thermostatic blanket in the stereotaxic frame. The mouse's body temperature was continually monitored and maintained at 37°C throughout the entire experimental session. A craniotomy of 1-2 mm in diameter (i.e. cranial window) was performed over each OB while maintaining the integrity of the *dura mater*. The brain surface within the cranial window was continuously perfused with artificial cerebrospinal fluid (aCSF; 119 mm NaCl; 26.2 mm $NaHCO_3$; 2.5 mm KCl; 1 mm NaH_2PO_4; 1.3 mm $MgCl_2$; 10 mm glucose) during the imaging procedure, to maintain brain surface's moisture. Animals' anesthesia was maintained with 1% v/v isoflurane for the entire imaging session. Odorant stimuli consisted of a mixture of odorants: Eugenol (Sigma Aldrich, CAS: 97-53-0), Isoamyl Acetate (Sigma Aldrich, CAS: 123-92-2), Butyralaldehyde (Sigma Aldrich, CAS: 123-72-8), Hexanal (Sigma Aldrich, CAS: 66-25-1), Carvone (Sigma Aldrich, CAS: 6485-40-1), Citral (Sigma Aldrich, CAS: 5392-40-5) were delivered with a custom-made olfactometer. All odorants were diluted 1% *v/v* in mineral oil. Odorant mixtures were prepared fresh prior to each experiment. Calcium imaging was performed in the olfactory bulb (OB) using a two-photon microscope (Bergamo I series, Thorlabs, Newton, NJ, USA). The system uses a tunable Ti:Sapphire laser (Chameleon Ultra II, Coherent) set at 920 nm to excite the calcium indicator, and its intensity was modulated with a Pockell cell (Conopitcs, Danbury, CT, USA). The fluorescence collection path includes a 705 nm long-pass main dichroic, an IR blocking filter, and a 495 nm long-pass dichroic that directs the fluorescence light to a highly sensitive GaAsP photomultiplier (PMT) detector (H7422PA-40 from Hamamatsu) with a EM525/50

emission filter. The control software was set up to image 30 frames per second, with a bidirectional galvo-resonant scanner, with a resolution of 512 X 512 pixels. Acquisitions were performed using 16x water-dipping objective (Nikon, Tokyo, Japan, LWD DIC N2, N.A. 0.8), with 2x zoom, with a field of view of 400 x 400 um. Focal plane was set at a depth of about 200-400 μm below the surface of the OB, corresponding to the mitral cell layer, populated by M C and a subpopulation of T cells. Identification of MC/TC was based on imaging depth and cell morphology.

Each imaging session had a duration of 25 minutes, resulting in the acquisition of 45,000 frames stored in .raw format. Multiple consecutive sessions were performed for each subject and each OB, typically amounting to around 5 sessions per OB.

Each acquisition session was structured as follows: an initial 60-second period without any odorant-stimulation to record baseline activity, followed by 10 stimulus presentations. Of these 10 presentations, 7 consisted of a mixture of odorants (See above for odorant mixture composition), while 3 was of mineral oil. Stimulus presentations were delivered in a pseudo-randomized fashion. Each odorant presentation lasted 3 seconds and was followed by a 117-second post-stimulus period. At the end of the stimuli sequence, spontaneous activity was recorded for an additional 120 seconds. To evoke sensory-induced activity, odorant stimulation was administered using a custom-made olfactometer. Imaging acquisition and odor delivery were synchronized and controlled by means of LabJack (https://labjack.com/products/labjack-t4) and a custom-made Python script. The olfactometer comprised three lines, each controlled by a two-way valve that was managed through the LabJack interface. The three lines converged into the gas mask, where they were administered along with isoflurane mix. The first line delivered clean air to the animal throughout the experiment, to ensure the removal of any residual odors from prior stimulations. The second line was employed to deliver mineral oil, while the third was dedicated to delivering the odor mixture. The use of the latter two lines was determined based on the pseudo-random

sequence generated for each experiment. Various signals were recorded, including the trigger for initiating imaging acquisition, the opening and closing of the valves, the identity of the operated valve, and the corresponding timing for each event. This dataset was saved in a .csv file for each acquisition. The time-series data from imaging and the timepoints for stimulation were aligned with the timing of the microscope's initiation trigger. At the conclusion of the experimental procedure, animals were humanely euthanized through the administration of urethane (with specific composition, 20%) followed by cervical dislocation.

Two-photon calcium imaging analysis. Time series data containing functional activity were processed using Suite2p (version 0.14.2) in Python 3.9.18. Suite2p was utilized for both motion correction and semi-automatic cell segmentation. At the end of automatic segmentation procedure, data set was manually inspected to verify accuracy and quality of ROI classification. Calcium traces were then Z-scored. Calcium peaks in the Z-scored traces were identified with the "peeling" algorithm[124]. Briefly, the peeling algorithm involved an iterative fitting of the z-scored trace using a double exponential function. In each iteration, the algorithm identified the first calcium event and subtracted the corresponding fitted trace from the raw trace. The process was repeated until the peeling procedure ceased to identify calcium events. Results produced by the peeling processes were subsequently employed to reconstruct the trace for each cell; the quality of the reconstruction process was assessed on the 30 second post stimulus Ca^{2+} traces. Once checked the quality of the reconstruction, the peeling approach was the extended to the entire recording. We then quantified the number of identified peaks, their amplitude, and the delay upon stimulus delivery (with the opening of the valve = t_0).

Population analysis.

- **Pearson's correlation**

  We computed Pearson's correlation coefficients on the recorded population of cells, during spontaneous activity and in response to odorant stimulation. To identify functional clusters based on the structure of the Pearson's correlation matrix, we performed a dimensionality reduction approach based on Single Value Decomposition (SVD). The number of dimensions of the SVD was defined for each acquisition in order to capture up to 99.9 % of the variance of the data. The number of the SVD components for each matrix identified the number of functional clusters. We performed this analysis on the various epochs of each recordings using the peeling-reconstructed traces.

  For the period upon stimulus presentation, clusters were identified on all the peaks, on the first peak alone, or on all the other peaks with the exclusion of the first one.

- **Identification of Ensembles on the recorded neuronal population**

  Additionally we computed the number of ensembles on spontaneous activity and in response to odorant stimuli, adapting the methodology introduced by Miller et al.[111]. In brief, the process involved the following steps:

  1. Binarization of the reconstructed traces using a threshold of ± 3.5 standard deviations.
  2. Identification of population vectors by selecting frames in which at least two cells display activity above threshold.
  3. Population vectors expected by chance were excluded using a surrogate data set generated by randomly shuffling 10,000 times individual column values for each cell in the data matrix. A frequency histogram of the surrogate data was created. We set a threshold to a significance value of p=0.05 and we discarded all the population vectors that fell below the set

threshold. Once identified the vectors above threshold, those were used for the subsequent analysis.

4. In order to identify clusters of population vectors we exploited Single Value Decomposition (SVD) based dimensionality reduction approach. Each component of SVD, i.e. cluster, contains all similar vectors, identified group of coactive cells indicated as ensemble.
5. We then quantified the average number of ensembles for each epoch of the recording, i.e. upon stimulus presentation, pre-stimulus and so on (see Fig. 20)

- **Principal Component Analysis (PCA)**

  PCA was computed on the reconstructed traces to identify differences in the principal components of Calcium signal in ophn1$^{-/y}$ and WT control mice. In order to have a single shared principal component space, we constructed a data structure containing the concatenated reconstructed traces, spanning from -30 to +30 seconds from each odorant stimulus presentation, for both the WT and ophn1$^{-/y}$ cells, facilitating the identification of shared or distinct components between the genotypes.

Fasudil administration. Ophn1$^{-/y}$ mice and WT littermate controls were treated with the ROCK non-competitive inhibitor Fasudil (HA1077, https://www.lclabs.com/), at around 8-10 weeks. Fasudil was dissolved in daily drinking water at 0.65 mg/ml and given orally 12 days before starting the intraperitoneal injection, for a complete chronic treatment of 3 weeks. Three mice were housed in each cage and received 20 mL of water with fasudil per day, to ensure a similar intake of the compound for each animal.

Subjects.

- Habituation-Dishabituation trials: WT n = 6; ophn1$^{-/y}$ n = 7; ophn1$^{-/y}$ + F = 9;
- OFT: WT n = 6; ophn1$^{-/y}$ n = 7; ophn1$^{-/y}$ + F = 9;

- LFP: WT n = 6; ophn1$^{-/y}$ n = 6; ophn1$^{-/y}$ + F = 7;
- Two-photon calcium imaging: WT n = 6; ophn1$^{-/y}$ n = 6;

Statistical tests.

Unless differently specified, all the statistical comparisons were carried out by means of a Mann-Whitney non-parametrical t-test.

Results.

Ophn1$^{-/y}$ mice exhibit olfactory impairments.

At first, we analyzed the impact of OPHN1 mutation on olfactory behavior. To this end, we exploited a common and well-validated behavioral paradigm, namely the habituation-dishabituation task (Fig. 14 A). This behavioral test is designed to assess the mouse's ability to detect and discriminate between different odorants, and it is also valuable for studying olfactory memory[125,126]. Briefly, cotton swabs soaked in double-distilled water were presented to the mouse for three consecutive times. On the fourth trial, a different odorant (i.e. isoamyl acetate or eugenol) was presented to the mouse. The investigation time for sniffing each odorant – within a period of two minutes – was measured. WT mice spent progressively less time investigating the same odorant, as they habituated (Fig. 14 C top panel; WT (1) vs. WT (2): 5.93 s ± 2.88 vs. 2.55 s ± 1.95; WT (4) vs. WT (5): 5.62 s ± 3.43 vs. 1.61 s ± 0.81; WT (7) vs. WT (8): 4.14 s ± 1.78 vs. 0.77 s ± 0.67) while when they detected a new odorant – in the dishabituation trials – the exploration time for sniffing the new odorant significantly increased (Fig. 14 C top panel; WT (3) vs. WT (4): 2.36 s ± 1.62 vs. 5.63 s ± 3.43; WT (6) vs. WT (7): 1.12 s ± 1 vs. 4.14 s ± 1.78). Ophn1$^{-/y}$ mice progressively spent less time investigating the same odorant, but the investigation time did not significantly increase in none of the two dishabituation trials. Importantly, the sniffing time was significantly higher for WT with respect of ophn1$^{-/y}$ in both the dishabituation trials (Fig. 14 B; WT (4) vs. ophn1$^{-/y}$ (4): 5.62 s ± 3.43 vs. 0.68 s ± 1.44; WT (7) vs. ophn1$^{-/y}$ (7): 4.14 s ± 1.78 vs. 0.93 s ± 0.85) and the

habituation trials (Fig. 14 B; WT (5) vs. ophn1$^{-/y}$ (5): 1.61 s ± 0.81 vs. 0.46 s ± 0.65; WT (8) vs. ophn1$^{-/y}$ (8): 0.77 s ± 0.67 vs. 0).

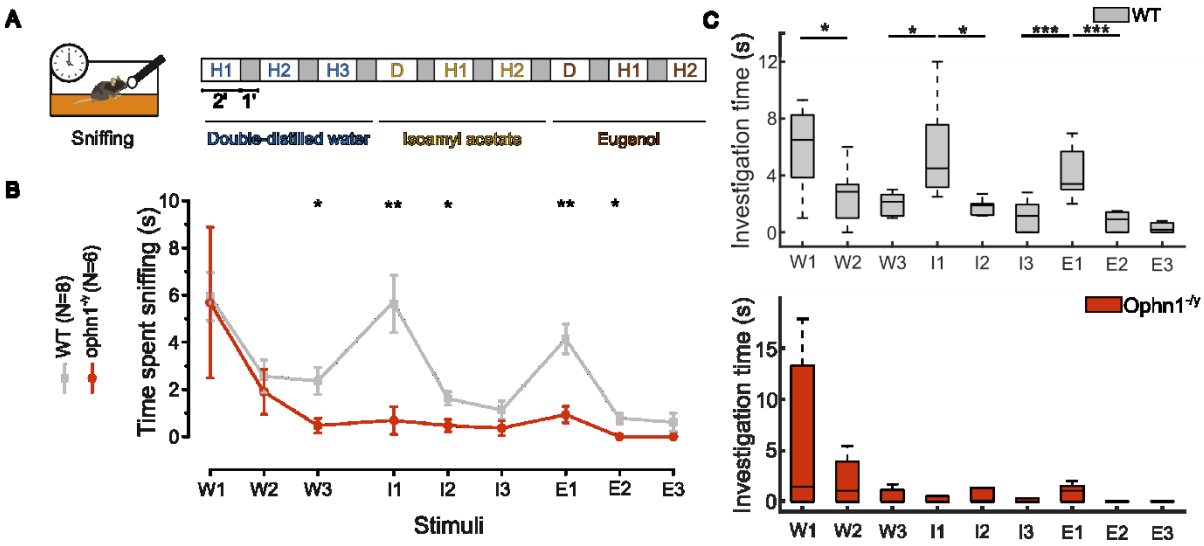

Figure 14 **Ophn1$^{-/y}$ mice exhibit impairments in the habituation-dishabituation task**. A) Schematic of the habituation-dishabituation task. Mice were placed within a Plexiglas cage and acclimated for a 30-minute period. Mice were then exposed to 3 consecutive presentations of a cotton swab soaked in double-distilled water (habituation trials). On the fourth trial (i.e., dishabituation trial), a cotton swab scented with isoamyl acetate was presented to the mice. The same happened at the seventh trial with the eugenol. B) WT mice exhibit a higher dishabituation to the olfactory stimuli presented in sequence, with respect to ophn1$^{-/y}$ for both the isoamyl acetate ($p = 0.004$) and the eugenol ($p = 0.001$), and longer sniffing time during the habituation trials, after the isoamyl acetate ($p = 0.04$) and the eugenol ($p = 0.05$) C) Intra-group analysis revealed that, within the WT mouse cohort, statistical distinctions were evident between in the first habituation trial ($p = 0.01$), in the second ($p = 0.01$) and in the third ($p = 5.62e^{-4}$), and the two dishabituation trials ($p = 0.04$; $p = 8.58e^{-5}$) while the same did not hold true for ophn1$^{-/y}$ for the habituation and the dishabituation.

Ophn1$^{-/y}$ mice do not exhibit locomotor impairments.

To exclude that impairments in the olfactory task could be ascribed to limited locomotor activity of ophn1$^{-/y}$ mice with respect to controls, we investigated the locomotor activity of the two genotypes. Mice were placed into an arena (35 x 35 cm) and were free to move within this space; subsequently, they were videorecorded for the entire duration of the test, i.e. 30 minutes. Eventually, thanks to the OptiMouse toolbox, animals' pose was segmented and estimated (Fig. 15 A-C). We found that ophn1$^{-/y}$ did not display significant differences in their mean

speed with respect to WT controls, although mutants exhibited a higher interindividual variability in speed than WT. (Figure 15 E-F, WT vs. ophn1$^{-/y}$: 1.95 cm/s ± 0.56 vs. 1.35 cm/s, ± 0.71). We then assessed how much time OPHN1 mutants spent in the center versus the periphery of the arena, with respect to their WT littermates. This ratio provides a good estimation of the subjects' anxiety levels and exploratory tendency, and it has been employed to characterize ASD/ID models[127]. We observed that ophn1$^{-/y}$ and WT mice spent a similar amount of time in the periphery with respect to the central zone of the arena. (Figure 15 G, WT vs. ophn1$^{-/y}$: 0.36, ± 0.47 vs. 0.33 ± 0.29). Overall, these results indicate that ophn1$^{-/y}$ mice do not exhibit neither a major locomotor impairment nor an anxious phenotype.

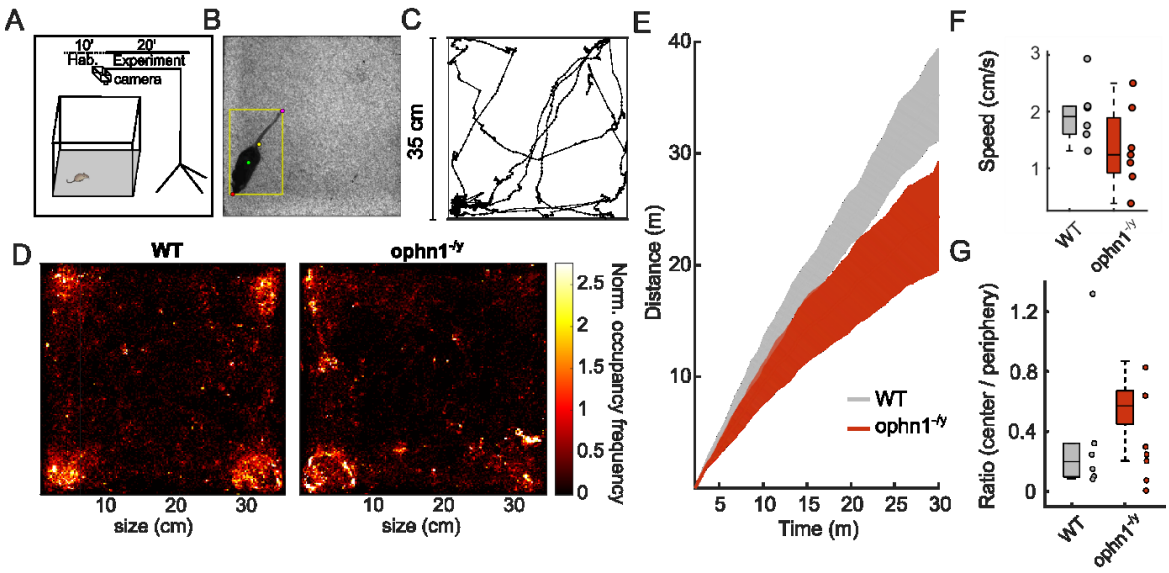

Figure 15 | **Ophn1$^{-/y}$ do not exhibit motor impairments in the open field task.** A) Schematic of the experiment structure. Mice were placed within a squared arena free to move, and video recorded for 30 minutes. B) Example of a single video frame. Color dots represent the landmarks on the mouse's body (See "Locomotion" in the Materials and Methods section for details). The resulting video was analyzed with OptiMouse[123]. C) Example of a reconstructed trace from 10-m exemplar segment. D) Heatmaps for ophn1$^{-/y}$ and WT littermates. In these pictures, all the spaces occupied by each mouse were grouped and averaged in 2 mm^2 bins, and the occupancy frequency was calculated for each mouse; then, mice were averaged over groups. E) Total distance covered by the two groups over the 30-m period of free exploration. F) Mean body speed of the two groups. ($p > 0.12$). G) Ratio between the time spent in the center compared to the periphery of the arena by mutant and control mice ($p = 0.85$).

Spectral analysis of Local Field Potentials (LFPs) recorded in the OB highlights abnormalities in the power of beta and gamma oscillations.

The habituation dishabituation task is a complex behavior supported by neuronal circuits within the OB and a wider network of brain areas, including the piriform cortex. The results we obtained in this olfactory task suggest that odor information processing is disrupted in these regions and indicate the potential benefit for dissecting their network dynamics. In this project, we focused our attention on the OB. Seeking to decipher the contribution of network dynamics to the olfactory behavior, we recorded LFP oscillations in the OB in freely behaving mice. Each mouse was recorded for a period of time lasting about 100 to 150 minutes. In this setting, mice exhibited two prominent behaviors: "resting" and "exploring" (Fig. 16). 15 minutes for each one of these behaviors was extracted by tagging multiple behavioral snippets.

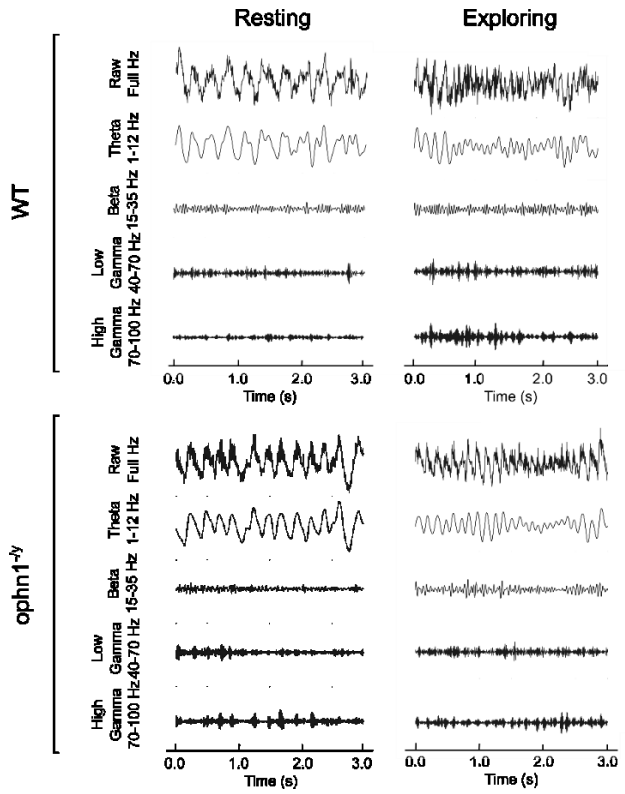

Figure 16. **LFP recorded in the mouse OB.** Top row) Exemplar LFP traces from the OB of a single WT mouse, during "resting" (left) and "exploring" (right) activity. Bottom row) Same as in the top row, but for an exemplar ophn1$^{-/y}$ mouse.

The range of the oscillations composing the LFP signal in these two different conditions was readily visible in the spectrograms of the whole recordings, with the two states exhibiting clear spectral signatures (Fig. 17 A). In particular, as shown in the power spectral densities (PSDs), the "resting" condition was mostly characterized by a high power in the low range (1—4 Hz) of theta oscillations (1—12 Hz) and a steep decrease in power in the beta (15—35 Hz) and gamma (40—100 Hz) bands, while the "exploring" condition displayed a widely distributed power over the theta range (1— 12 Hz) and presented more power in the beta and gamma ranges with respect to the "resting" condition (Fig. 17 B).

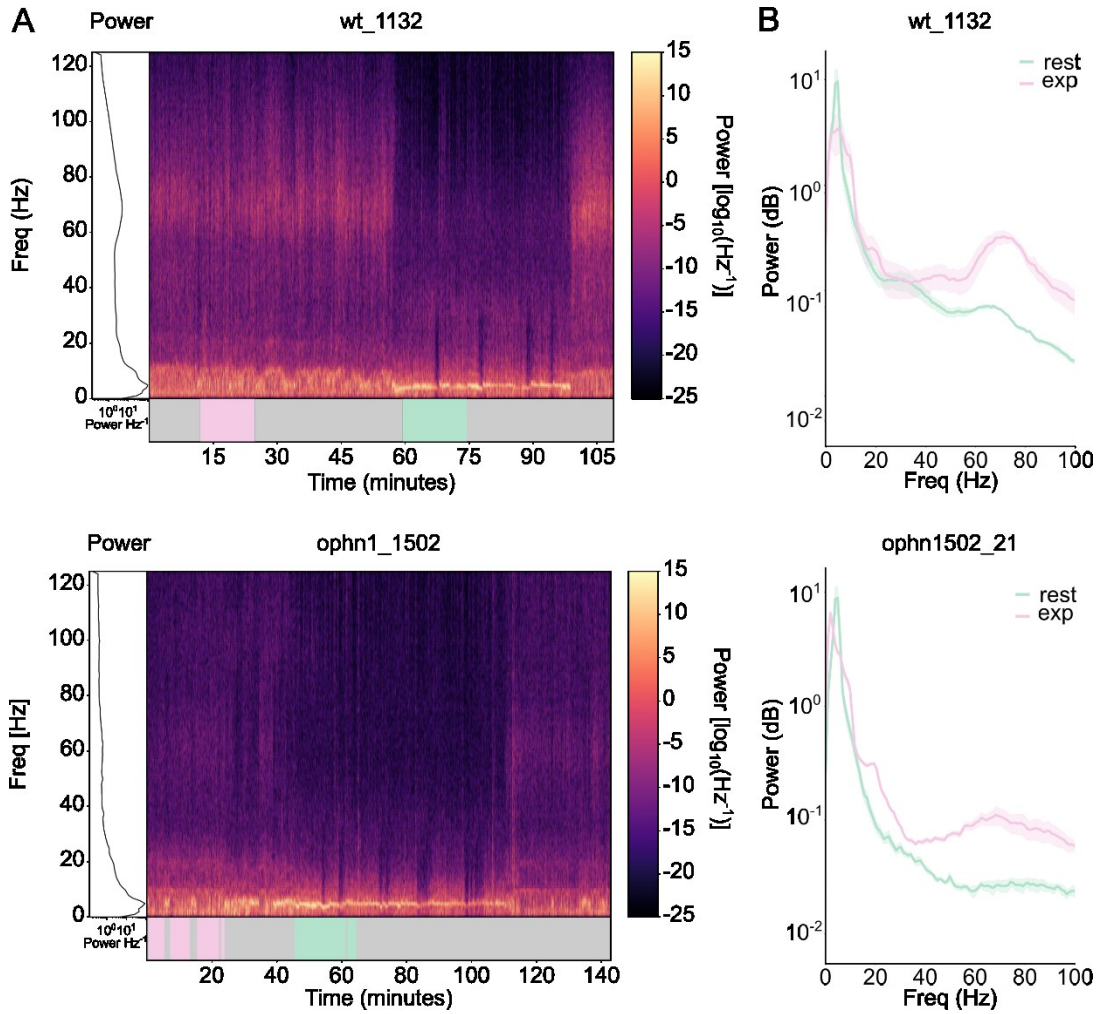

Figure 17. **Spectrogram and power spectral densities (PSDs) for exemplar mice.** A) Two spectrograms of a whole LFP recording for a WT (top) and an ophn1$^{-/y}$ (bottom) mouse. Pink and green rectangles indicate the extracted snippets of – relatively – exploring and resting. B) PSDs calculated over the same recordings in the same exemplar WT (top) and ophn1-/y (bottom) subjects.

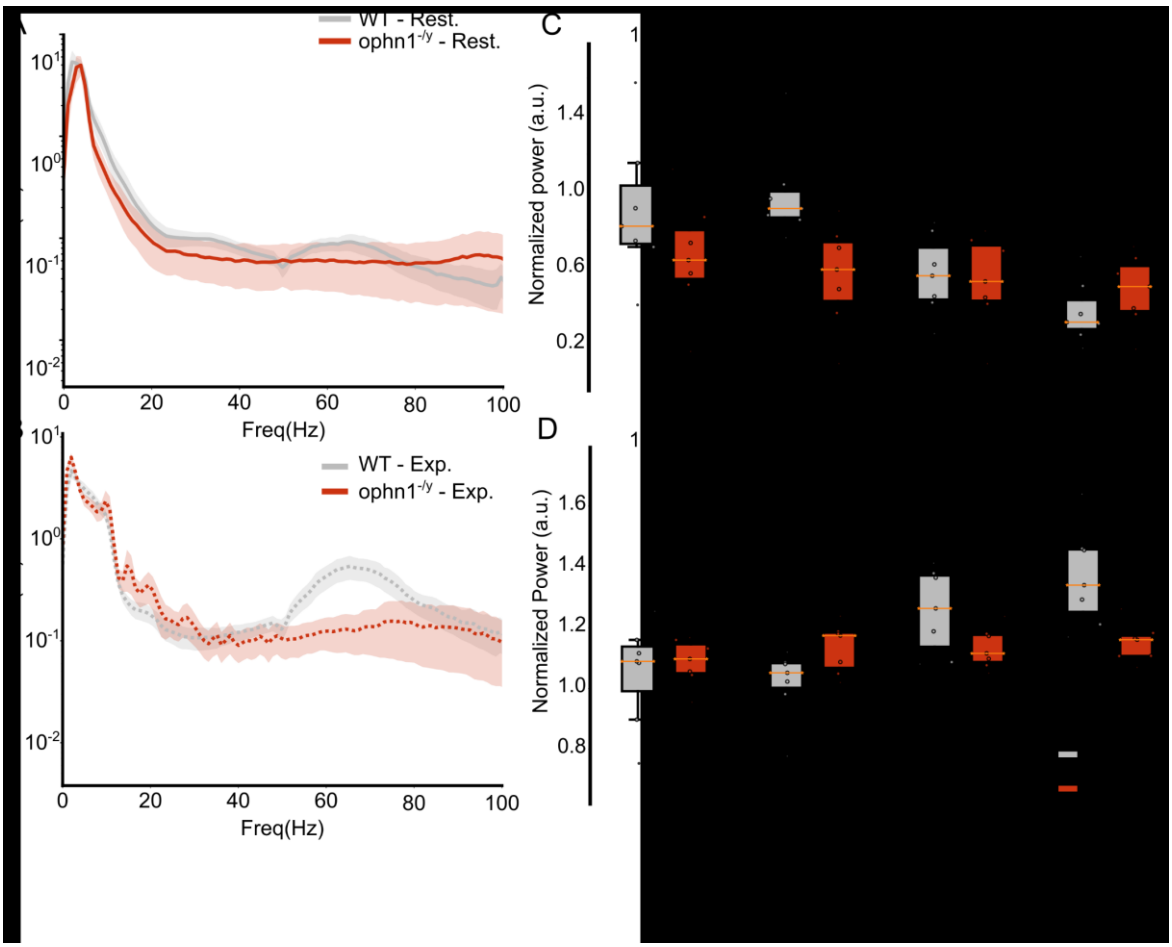

Figure 18. **Relative powers in the "exploring" and "resting" conditions**. A) Average PSD for the "resting" condition. B) Average PSD for the "exploring" conditions. C) PSD averaged over different frequency bands, i.e. theta, beta, low-gamma and high-gamma, display differences between strains during the "resting" condition in the beta band ($p < 8e^{-3}$) and D) Higher power for WT mice in the beta ($p = 0.05$) and high-gamma band, in the "exploring condition ($p < 0.006$).

We sought to understand whether ophn1$^{-/y}$ mice exhibited unique features in this landscape of oscillatory power. First, we compared the normalized power in the "resting" condition in WT and ophn1$^{-/y}$, finding significant differences in the beta frequency band between the two genotypes (Fig. 18 A-B, "Top Panel"; WT vs. ophn1$^{-/y}$: 0.93 ± 0.06 vs. 0.58 ± 0.14). We then replicated this procedure for the "exploring" condition, which highlighted a significant difference in the beta (Fig. 18 A-B, "Bottom Panel"; WT vs. ophn1$^{-/y}$: 1.04 ± 0.03 vs. 1.13 ± 0.05) and in the high-gamma band (WT vs. ophn1$^{-/y}$: 1.35 ± 0.09 vs. 1.14 ± 0.03).

Eventually, we calculated the difference between the average power in the "exploring" and the "resting" phase in the beta and gamma bands, to compare significant differences in WT and mutants. The results highlighted significant differences in both the beta (Fig. 19 B; WT vs. ophn1$^{-/y}$: 0.10 dB ± .10 vs. 0.54 dB ± 0.21) and the high-gamma range (Fig. 19 B; WT vs. ophn1$^{-/y}$: 1.01 dB ± 0.19 vs. 0.63 dB ± 0.15). In particular, ophn1$^{-/y}$ mice exhibited a significantly higher power in the beta band, while a reduced power in the high-gamma band. Together, these data indicate that OPHN1 deficiency severely impacts neuronal oscillations in the olfactory bulb when subjects are engaged in sensory-processing tasks.

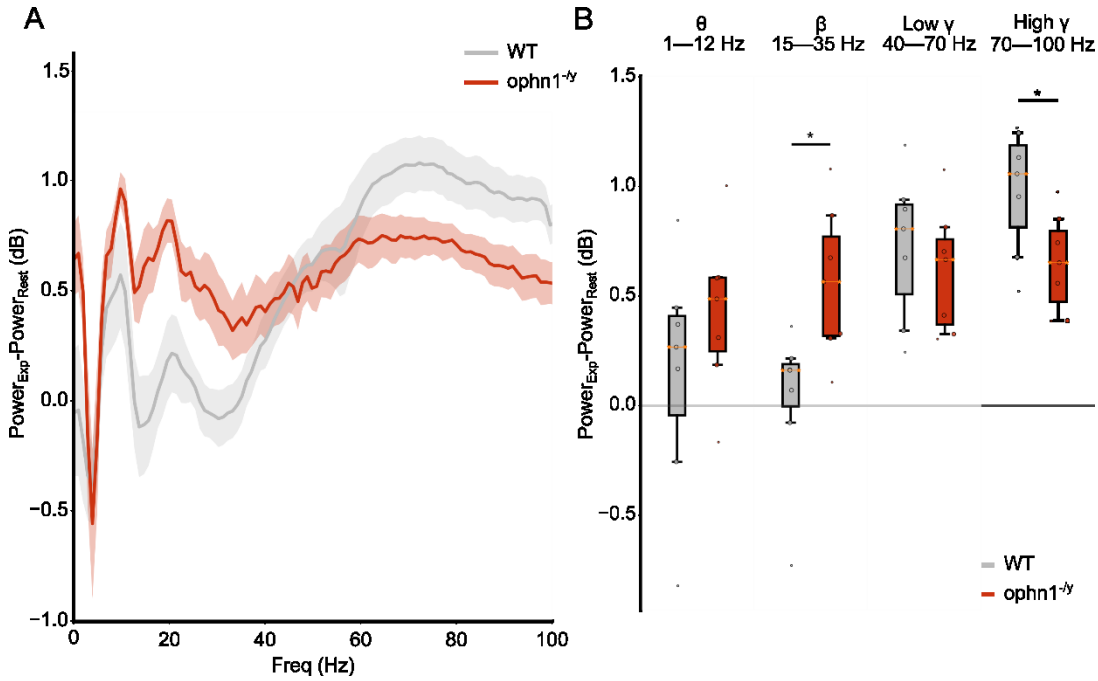

Figure 19. **Ophn1$^{-/y}$ mice exhibit altered oscillations in the OB when displaying the difference between the two considered conditions.** A) Power difference between "exploring" and "resting" condition. B) Power difference was segmented between the four considered frequency bands (i.e., theta, beta, low-gamma and high-gamma). The power difference highlighted statistically significant power differences between the WT and mutated subjects; in particular, ophn1$^{-/y}$ exhibited higher power in the beta band (p = 0.01), while displaying a reduced power in the high-gamma range (p = 0.04).

Ophn1$^{-/y}$ mice exhibit significant differences, at single-cell level, in calcium responses to odorants recorded by two-photon imaging.

LFP recordings provide critical information essential to describe the temporal dynamics of brain activity. Nonetheless, despite their ability to finely catch fast processes occurring within large populations of neurons, the major disadvantage

of LFPs consists of their limited spatial resolution. In order to characterized neuronal population activity with single-cell resolution in the OB, we took advantage of two-photon calcium imaging. We employed two-photon functional imaging to capture the activity of neuronal populations at cellular resolution in the OB utilizing the genetically encoded calcium sensor GCaMP6s as an activity reporter (see "Two-photon calcium imaging" experiment in the "Materials and Methods" section; Fig. 20 A). Taking advantage of the well-layered structure of the OB, we recorded neuronal activity at about 300 μm below the OB surface, corresponding to the mitral cell layer (MCL), where mitral cells and a sub-population of tufted cells are located (Fig. 20 B). Importantly, gamma oscillations are generated within this layer since they originate at the synapse between mitral cells and granule cells. Therefore, this layer represents a key spot in the OB for unveiling ongoing processes in response to sensory stimuli. The experimental protocol consisted of a pseudo-randomized odorant sequence comprising 10 stimuli (7 odorant mix and 3 mineral oil). Odorants were presented for 3 seconds, with two minutes of inter-stimulus interval (ISI). The analysis of neuronal activity was performed as follows: we analyzed the neuronal activity for 30 seconds upon stimulus presentation (i.e., 30 seconds following the opening of the valves which delivers odorants; Fig. 20 C). This time window was considered to analyze a period of early response to the stimulus and the subsequent stimulus-related activity. In addition, we analyzed neuronal activity in a window of 30 seconds before each stimulus presentation – so that it was set as the reference time window for spontaneous activity. In each experiment, several FOVs were acquired from the OBs of each animal, and only the cells responsive to odorant stimuli presentation were considered for the subsequent analysis (see "Two-photon calcium imaging experiment" in the Materials and Methods section).

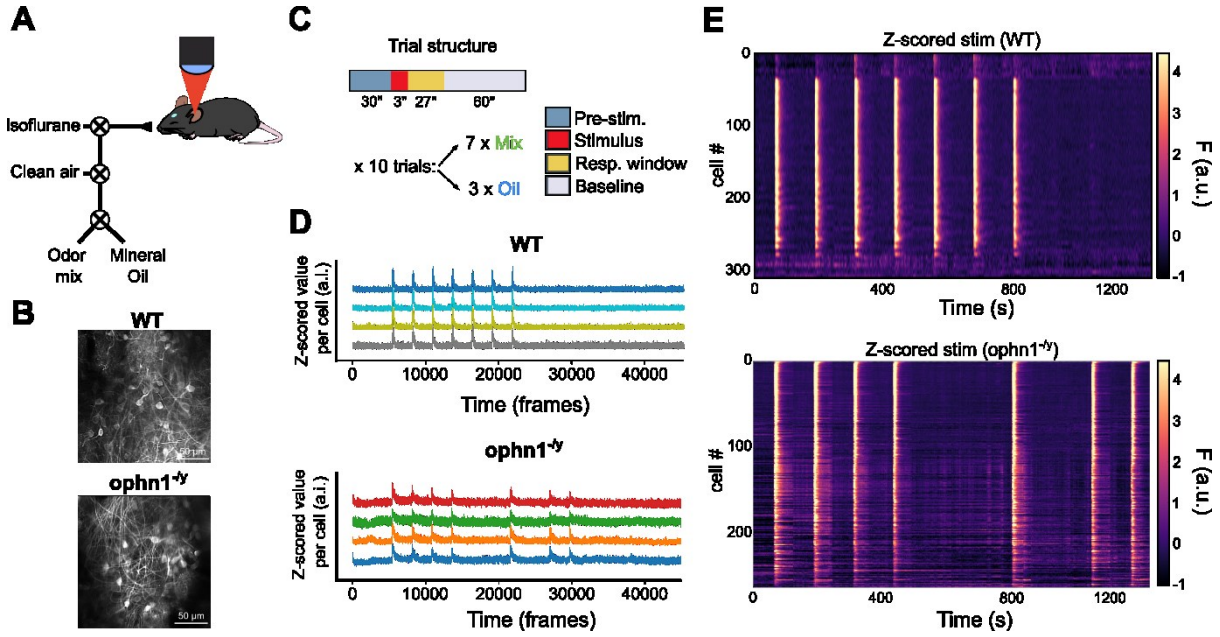

Figure 20. **Two-photon imaging experiment.** A) The animal is placed under the two-photon microscope and receives olfactory stimuli via a custom-made olfactometer. B) Representative two-photon average projections images of GCaMP6s-expressing M/T cells. C) Trial structure of the two-photon imaging experiment with the considered time windows. D) Example of calcium traces of the neurons recorded in the OB in WT and ophn1$^{-/y}$ mice. E) Raster plots of calcium responses (F) to stimuli in WT and OPHN1 mice.

We first compared the average number of responsive cells in WT and ophn1$^{-/y}$ mice by looking at the ratio of active cells in response to at least one odorant mix stimulus, or to all (n = 7) odorant mix stimuli. The percentage of cells responsive to at least one odorant mix stimulus was on average 95.7% for the WT mice, while the percentage of cells responsive to at all odorant stimuli (n = 7) was on average 74.2% (Fig. 21 A, left column; WT (1) vs. WT (7): 95.7 % ± 5.47 S.D. vs. 74.2 % ± 25.9 S.D.). Similarly, the percentage of cells responsive to at least one odorant mix stimulus was on average 99% for the ophn1$^{-/y}$ mice, while cells responding to all odorant stimuli represented on average the 73.8% (Fig. 21 A, right column: 99 ± 0.6 S.D. vs. 73.8 S.D.). Altogether, we observed no significant difference in cell responsiveness between WT and ophn1$^{-/y}$ mice. To analyse neuronal responsiveness in the two genotypes, we first computed the integral of the ΔF/F signal over time (Fig. 21 B). We compared the response to the olfactory stimuli (for each odorant mix and mineral oil, that functioned as a control for the odorant delivery), and we observed

a significantly greater response to the odorant mix compared to the mineral oil, in WT (WT mix vs. WT oil: 607.4 a.u. ± 328.8 vs. 143.9 a.u. ± 171.2) and in ophn1$^{-/y}$ mice (ophn1$^{-/y}$ mix vs. ophn1$^{-/y}$ oil: 416 a.u. ± 206.3 vs. 179.7 a.u. ± 177.9). Given the small responses elicited by the mineral oil, this stimulus was excluded in subsequent analyses. In contrast, comparing the integral ΔF/F in response to odorant stimuli in the two genotypes, we found that the average ophn1$^{-/y}$ mice response to odorants was smaller than in WT. A larger integral of ΔF/F implicates an overall greater level of activity, in terms of firing rate, of M/T cells within the OB, suggesting a more prolonged and intense response to the olfactory stimulus.

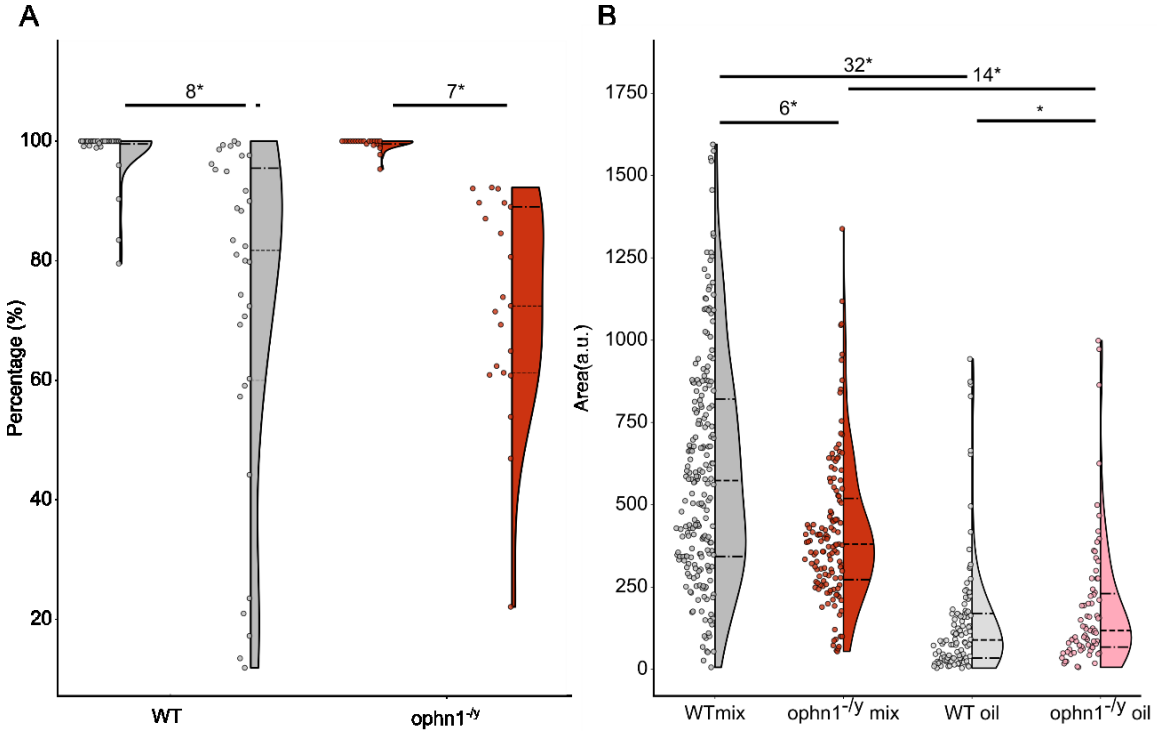

Figure 21. **Quantification of percentage of active cells and odorant responsiveness in WT and ophn1 mice** A) Percentage of cells responsive to at least one or to all odorant stimuli for WT ($p < 2.5e^{-9}$) and ophn1$^{-/y}$ ($p < 1.7e^{-8}$). No differences emerged comparing the strains, considering both cells responsive to at least one stimulus ($p = 0.88$) or to all the stimuli ($p = 0.33$). B) Area under the response curve for WT and ophn1$^{-/y}$ in response to both the odorant mix and the mineral oil. Both the WT ($p < 3.7e^{-33}$) and ophn1$^{-/y}$ ($p < 2.1e^{-15}$) showed higher response compared to mineral oil; additionally, WT responses to mix were on average higher, with respect of ophn1$^{-/y}$ ($p < 2.26^{e-7}$).

Analysis of calcium peaks in response to odorant stimuli, in ophn1$^{-/y}$ and WT.

The analysis of the integral of the calcium response to the olfactory stimuli provides a coarse, though valuable, representation of neuronal activity. Since we aimed to better characterize the structure of the calcium responses, we adapted the peeling algorithm from a previous study of Grewe and colleagues[124] to identify and characterize individual calcium events likely originating from brief spike bursts. The peeling approach consists of an iterative double exponential fitting and subtraction that allows to identify and reconstruct putative calcium events in the noisy raw traces (see "Two-photon calcium imaging analysis" in the Materials and Methods section). This peeling algorithm gave the opportunity to look not only at the unfolding of the calcium activity over time in response to the stimulus, but also to compare several parameters, such as the amplitude of the individual calcium events and their temporal structure, and to further characterize the organization of the network. The result of the peeling procedure is a reconstructed trace which has two important features: the first one consists of the elimination of instrumental noise, while the second one is its faithfulness in reconstructing the calcium trace, with the respect to the raw one. To evaluate the goodness of the peeling algorithm, we calculated the RMSE between each z-scored and reconstructed trace, for both WT and ophn1$^{-/y}$. The RMSE distribution may be used as a parameter to evaluate the faithfulness of the reconstruction – indeed, it should represent most of the noise in the signal. We found that the RMSE values were not differing between the two strains (Fig. 22 B; WT vs ophn1$^{-/y}$: 0.79 a.u. ± 0.09 vs. 0.82 a.u. ± 0.06). Given these results, we decided to use only the reconstructed traces for subsequent analyses. A further selection of active cells was operated downstream of the peeling process: only the cells with at least one calcium event were further analyzed (See "Two-photon imaging analysis" in the Materials and Methods section). The number of identified peaks was different between the two genotypes, with WTs having a

higher number of identified peaks (Fig. 22C; WT vs. ophn1$^{-/y}$: 2.59 ± 0.83 vs. 2.00 ± 0.72) over the 30 seconds time window after the stimulus presentation, with respect to ophn1$^{-/y}$ mice. The peeling process returned at most 5 peaks in this time-window. To further characterize the morphology and the temporal structure of the calcium peaks, we quantified the amplitude of each peak, and their temporal relation with respect to the odorant presentation (time to reach the peak, indicated as "delay").

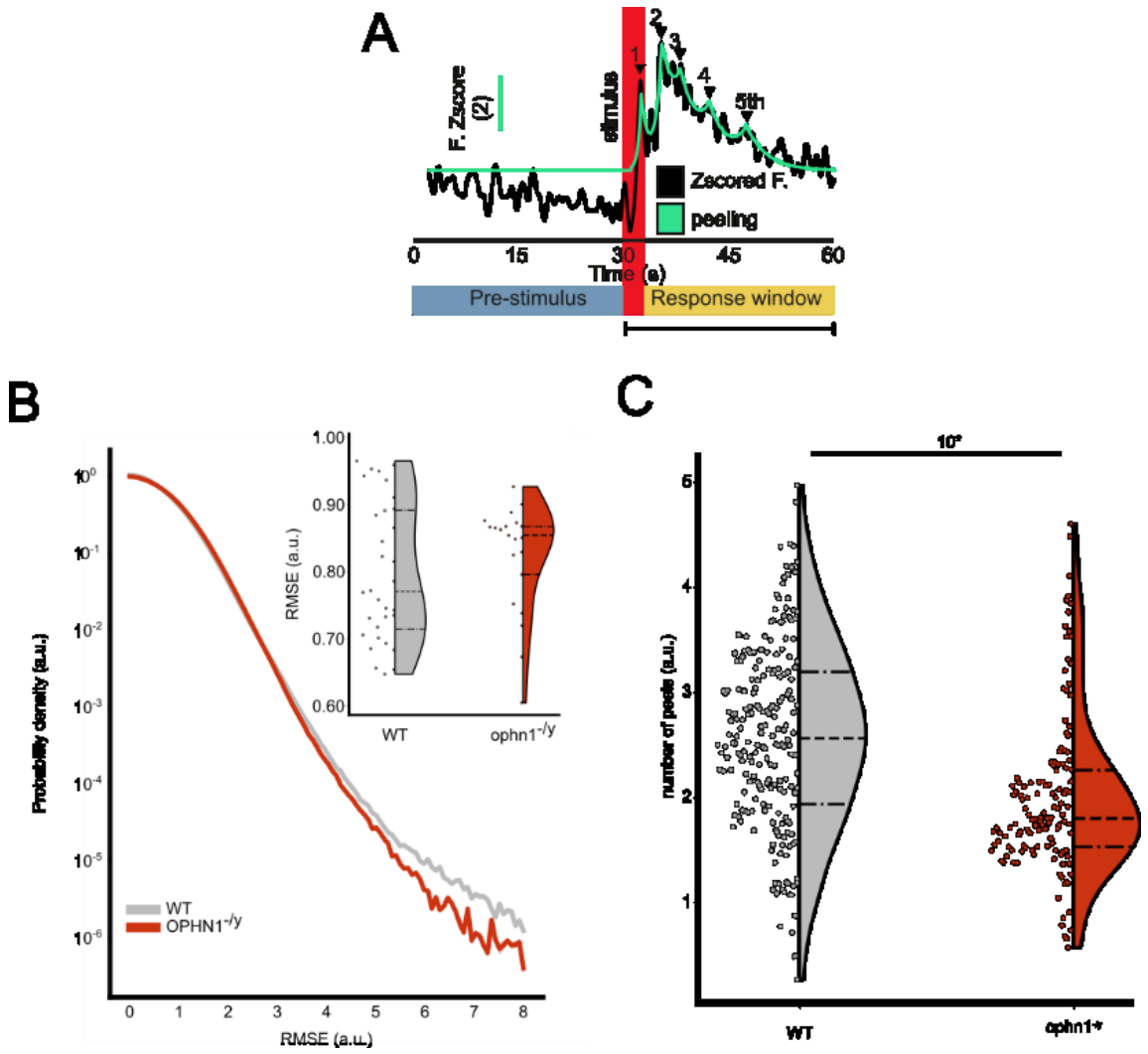

Figure 22. **Reconstruction of calcium traces exploiting the peeling algorithm.** A) Raw (black) versus peeling-reconstructed (light green) trace. Peaks found by the peeling algorithm are shown in the image. B) Probability density of the Root Mean Square Errors (RMSE) of the residuals between the observed values and the ones generated by the peeling algorithm. Top right. Boxplot of the RMSE value for each field, for both WT and ophn1$^{-/y}$, highlights no difference between the strains ($p = 0.37$). C) Number of identified peaks for WT and ophn1$^{-/y}$ highlights a higher average number of peaks WT ($p < 2.91e^{-11}$).

The amplitude was measured at the peak of each identified calcium event, while the delay was considered as the time between stimulus onset and the calcium transient peak (t_0 = trigger of the odorant stimulus). We evaluated such metrics within the 30-s time window of response. The amplitude and the delay of each peak highlighted abnormalities in the ophn1$^{-/y}$ mice with respect to their WT littermates, with all the five identified peaks to display significant differences between the genotypes. The first peak was on average identified within five seconds from t_0, with no significant differences between the two strains, (i.e. no difference in the delay of the first peak in WT and ophn1$^{-/y}$. Fig. 23; WT delay 1st vs. ophn1$^{-/y}$ delay 1st: 4.24 s ± 2.40 vs. 3.68 s ± 0.99). Nevertheless, when we compared the amplitude of the first peak, ophn1$^{-/y}$ displayed a significantly larger rise in calcium transients (Fig. 23; WT amplitude 1st vs. ophn1$^{-/y}$ amplitude 1st: 2.92 a.u. ± 1.41 vs. 3.38 a.u. ± 1.48). From the second peak on, we observed for each peak a significantly consistent reduction in amplitude in ophn1$^{-/y}$ mice, compared to their WT littermates (WT amplitude 2nd vs. ophn1$^{-/y}$ amplitude 2nd: 1.35 a.u. ± 0.75 vs. 1.22 a.u. ± 0.95; WT amplitude 3rd vs. ophn1$^{-/y}$ amplitude 3rd: 0.58 a.u. ± 0.37 vs. 0.41 a.u. ± 0.40; WT amplitude 4th vs. ophn1$^{-/y}$ amplitude 4th: 0.32 a.u. ± 0.28 vs. 0.17 a.u. ± 0.28; WT amplitude 5th vs. ophn1$^{-/y}$ amplitude 5th: 0.16 a.u. ± 0.19 vs. 0.10 a.u. ± 0.19), while the delay was significantly larger in ophn1$^{-/y}$ than in WT (Fig. 23; WT delay 2nd vs. ophn1$^{-/y}$ delay 2nd: 11.49 s ± 3.65 vs. 13.70 s ± 2.83; WT delay 3rd vs. ophn1$^{-/y}$ delay 3rd: 18.40 s ± 3.24 vs. 20.90 s ± 2.11; WT delay 4th vs. ophn1$^{-/y}$ delay 4th: 22.99 s ± 2.43 vs. 24.75 s ± 1.87; WT delay 5th vs. ophn1$^{-/y}$ delay 5th: 26.66 s ± 1.54 vs. 27.26 s ± 1.27).

Impact of OPHN1 mutation on neuronal network organization, in response to odorant presentation.

To investigate the impact of the OPHN1 mutation on network organization, we computed the Pearson's correlation for all the active cells in response to each odorant stimulus in every FOV. Pearson's correlation coefficient – denoted as "r" – is a linear measure of the covariance of two sets of data. Pearson's correlation in

neuronal activity is critical to understand how populations of neurons collectively encode information. In this scenario, two-photon calcium imaging provides a unique opportunity to record the activity of thousands of neurons, *in vivo*, offering the key substrate to analyze how correlated activity among neurons encode neuronal information and to investigate neuronal network organization (Fig. 24 A).

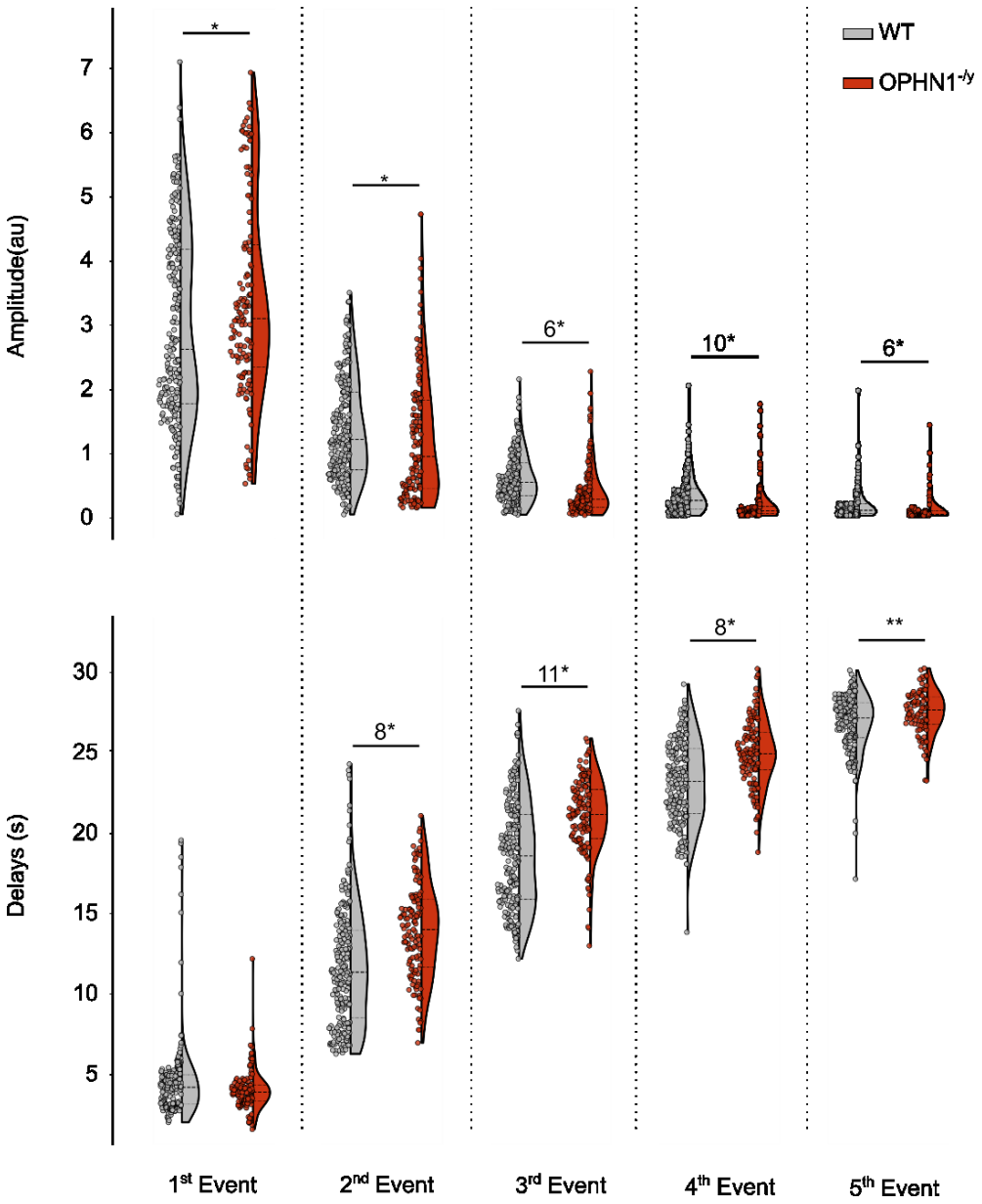

Figure 23. **Amplitude and delay of each calcium peak in response to odorant stimuli.** Top panel) The average amplitude of the first identified calcium peak was higher in ophn1$^{-/y}$ mice with respect to WT ($p = 0.006$), while it decreased with the subsequent ones (2nd: $p = 0.019$; 3rd: $p = 1.48e^{-7}$; 4th: $p = 2.80e^{-11}$; 5th: $1.43e^{-7}$). B) Average delay of calcium peaks upon stimulus presentation highlighted no differences for the event ($p = 0.12$), while it decreased in ophn1$^{-/y}$ for the subsequent ones (2nd: $2.04e^{-9}$; 3rd: $p = 1.59e^{-12}$; 4th: $p = 7.18e^{-10}$; 5th: $p = 0.003$).

Importantly, the degree of correlation between cells is thought to be regulated by inhibitory interneurons[128,129]. We then computed the average Pearson's correlation on the 30 seconds time window upon stimulus presentation, finding no significant differences between ophn1$^{-/y}$ mutants and WT controls (Fig. 24 B first column; WT response vs. ophn1$^{-/y}$ response window: 0.52 ± 0.23 vs. 0.50 ± 0.18). Such result is apparently at odd with the behavioral and electrophysiological data, and in particular with the alterations of the high-gamma-band activity. In addition, considering the differences in the amplitude and delay of calcium peaks in the two genotypes (see Fig. 23), we expected a difference in network organization in ophn1$^{-/y}$ with respect to their WT littermates. We reasoned that we could not highlight possible differences in Pearson's correlation as the analysis was performed on the whole period of 30 seconds upon stimulus presentation, which includes several different calcium events (see Fig. 22). For this reason, we decided to compute the Pearson's correlation leveraging on the reconstructed traces with the peeling process. In this way, we could compute the Pearson's correlation for the first peak and in all the subsequent peaks. When evaluating only the first peak, that is, the one closer to the odorant presentation, no significant differences between the two genotypes were identified (Fig. 24 B, second column; WT 1st event vs. ophn1$^{-/y}$ 1st event: 0.58 ± 0.22 vs. 0.55 ± 0.18). However, when Pearson's correlation was computed on all the peaks except for the first one, the difference between the two genotypes became statistically significant, with a greater Pearson's correlation among neurons in WT, compared to ophn1$^{-/y}$ mice (Fig. 24 B, third column; WT 2nd to 5th event vs. ophn1$^{-/y}$ 2nd to 5th event: 0.21 ± 0.15 vs. 0.15 ± 0.08).

Based on the values of the Pearson's correlation coefficient we clustered the cells in functional modules. We used single-value decomposition (SVD) to extract the number of clusters in the matrices of the Pearson's correlation. WT and ophn1$^{-/y}$ had significant different number of clusters for the overall 30 seconds time window

after the stimulus, for the first peak only, and for all the subsequent ones together (Fig. 25).

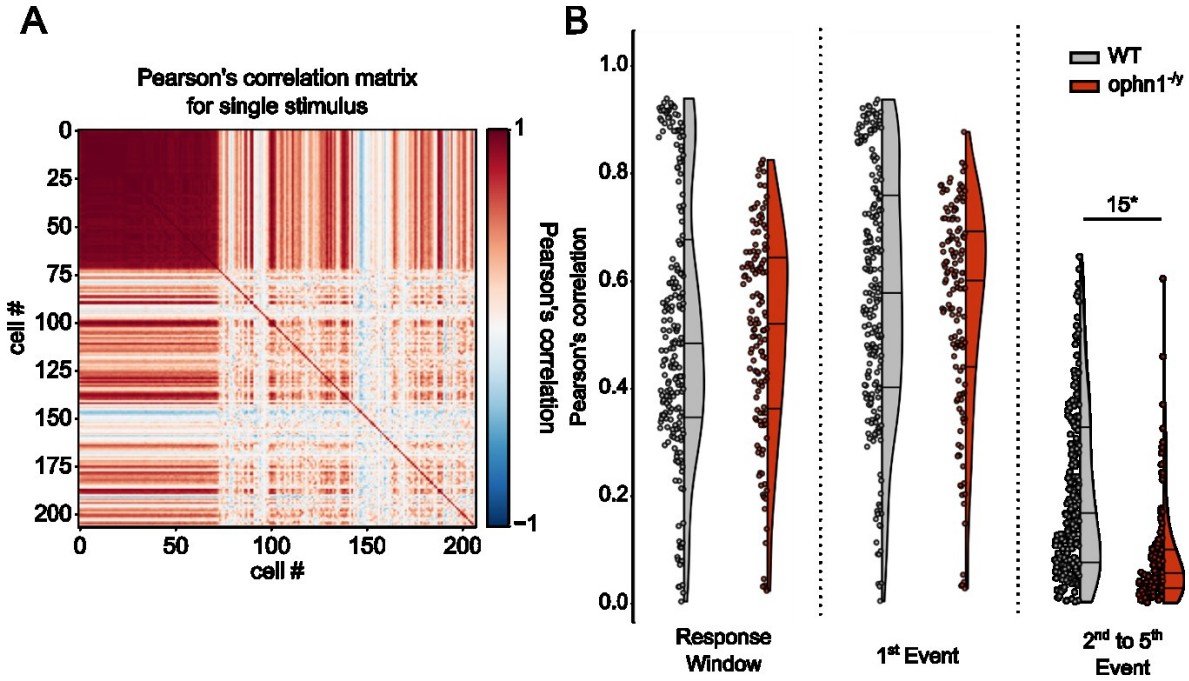

Figure 24. **Pearson's correlation analysis on Ca^{2+} responses to odorants.** A) Cross correlation matrix for a single stimulus between all the cells. B) Pearson's correlation values for the whole 30-s post-stimulus time window (first column) highlighted no difference between the genotypes ($p = 0.23$); similarly, no difference emerged when considering exclusively the first peak (second column; $p = 0.39$) and for all the peaks except for the first one (third column; $p < 1.22e^{-16}$).

The number of clusters was significantly lower for ophn1$^{-/y}$ when we considered the whole 30 second post-stimulus time window (Fig. 25, first column; WT response window vs. ophn1$^{-/y}$ response window: 6.14 ± 2.01 vs. 4.99 ± 1.64), suggesting an overall reduced diversity among the functional profiles of the cells, forming fewer distinct groups in response to the olfactory stimuli. This result was confirmed when we considered only the first peak identified by the peeling algorithm (Fig. 25, second column; WT 1st event vs. ophn1$^{-/y}$ 1st event: 4.86 ± 1.15 vs. 4.52 ± 1.28). In contrast, when we considered all the remaining peaks, ophn1$^{-/y}$ exhibited a higher number of clusters, with respect of their WT littermates (Fig. 25, third column; WT 2nd to 5th event vs. ophn1$^{-/y}$ 2nd to 5th event: 7.17 ± 2.45 vs. 7.96 ± 2.69).

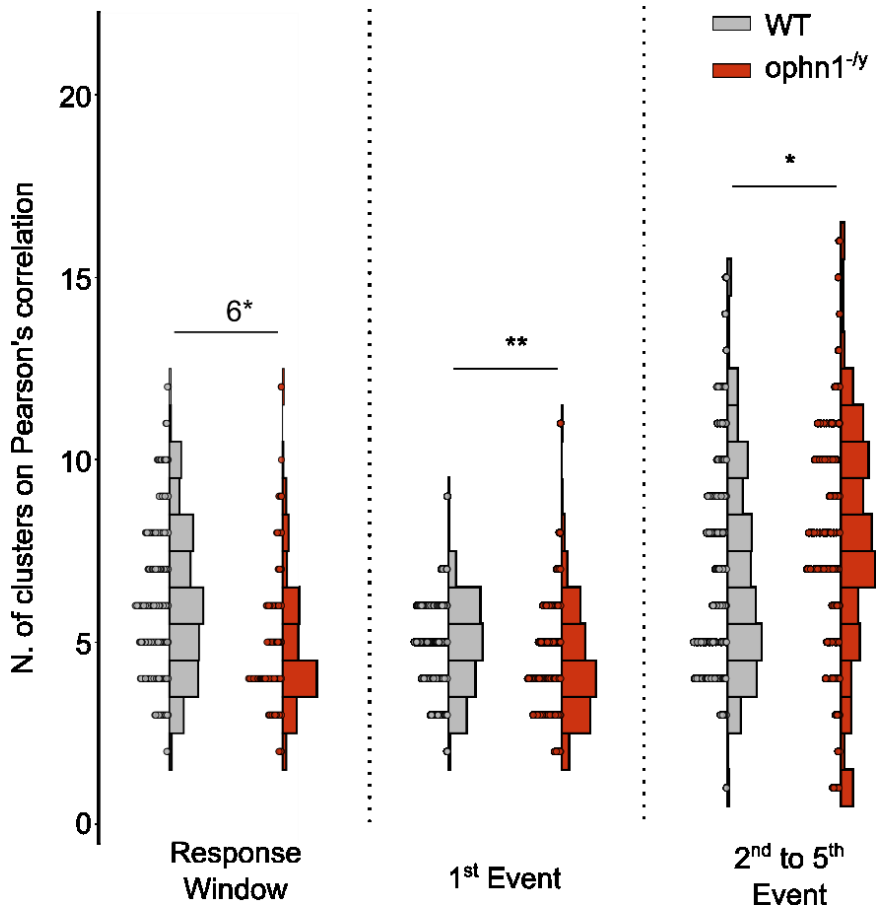

Figure 25. **Clustering based on the Pearson's correlation analysis.** Number of functional clusters found based on the Pearson's correlation matrices is higher for WT considering the whole post-stimulus period (first column; $p = 1.48e^{-7}$), and the first event (second column; $p = 0.001$), while the result inverted when considering all the remaining peaks (third column; $p = 0.007$).

Identification of ensembles in ophn1$^{-/y}$ and WT.

Different approaches to study the complexity of network activity have been developed, among them the characterization of neuronal ensembles structures has been proven to be effective and it is nowadays largely used[111,121,130]. Briefly, neuronal ensembles are groups of coactive neurons that are considered "building blocks of functional circuits" and units of the neuronal code[113]. The presence of such ensembles in the OB remains currently elusive, even though it is reasonable to think this kind of structure is a distributed property of the CNS[115]. For this reason, we extracted the number of neuronal ensembles in the neuronal population of the OB. To identify these functional ensembles, we binarized the peeling-reconstructed

traces for each cell and clustered by means of single-value decomposition (SVD) the resulting population vectors (Fig. 26 A-B. See "Two-photon imaging analysis" in the Materials and Methods section). We report the number of neuronal ensembles identified in response to each odorant stimulus. The analysis was conducted on the whole period upon stimulus presentation (Fig. 26 C, first column. WT response window vs. ophn1$^{-/y}$ response window: 7.95 ± 3.74 vs. 8.51 ± 4.00). In addition, leveraging on the peeling algorithm, we repeated this same computational approach on the first calcium peak upon odor stimulation (Fig. 26 C, second column. WT 1st event vs. ophn1-/y 1st event: 10.39 ± 1.71 vs. 9.46 ± 1.87), or on all the peaks following the first one, which, in this case, was excluded (Fig. 26 C, third column. WT 2nd to 5th event vs. ophn1-/y 2nd to 5th event: 10.05 ± 2.93 vs. 8.65 ± 2.59). We observed a significantly different number of ensembles for each of these conditions and – importantly – the average number of ensembles for the ophn1$^{-/y}$ mice was significantly lower, compared to WT.

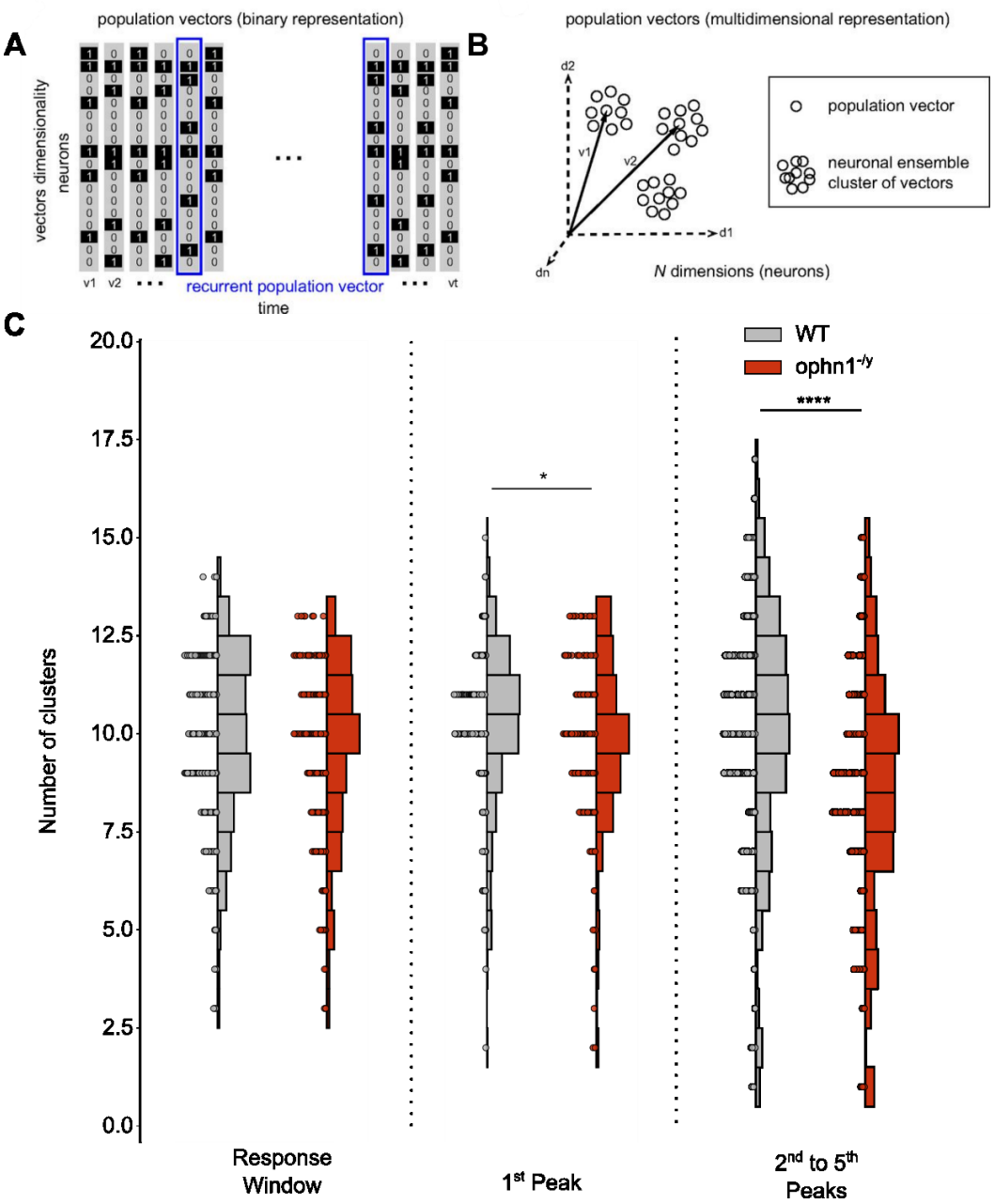

Figure 26. **Neuronal ensembles in OB's neuronal populations, in WT and ophn1$^{-/y}$ mice .** A) Example binarized raster plot from a single recording. White indicates non-active cells, while black identifies the active ones. B) Population vectors obtained with a dimensionality reduction approach (SVD). C) Neuronal ensembles identified based on binarized traces in different neuronal population, namely the whole 30-second post-stimulus time window, the first peak identified by the peeling algorithm and all the remaining peaks, excluding the first one.

Impact of OPHN1 on spontaneous activity.

We then investigated the impact of OPHN1 on spontaneous activity. We performed the same analyses we carried out on the feature of single-cell responses, observing no differences between the two genotypes in 1) the integral of the calcium ΔF/F signal (Fig. 28 A; WT vs. ophn1$^{-/y}$: 112.23 a.u. ± 134.50 vs. 109.40 a.u. ± 145.45), and 2) in the number of peaks identified with the peeling algorithm (Fig, 28 B; WT vs. ophn1$^{-/y}$: 1.35 ± 0.77 vs. 1.25 ± 0.83). We then analyzed the impact of OPHN1 on network organization in spontaneous activity computing the Pearson's correlation and we did not find difference in the two strains (Fig. 28 C; WT vs. ophn1$^{-/y}$: 0.04 ± 0.09 vs. 0.04 ± 0.06). We calculated the number of clusters based on the Pearson's correlation matrix, finding again no differences between WT and ophn1$^{-/y}$ (Fig. 28 D; WT vs. ophn1$^{-/y}$: 10.07 ± 3.03 vs. 10.40 ± 2.80). Finally, we evaluated the number of neuronal ensembles, and also in this case no difference emerged between the genotypes (Fig. 28 E; WT vs. ophn1$^{-/y}$: 7.95 ± 3.74 vs. 8.51 ± 4.03).

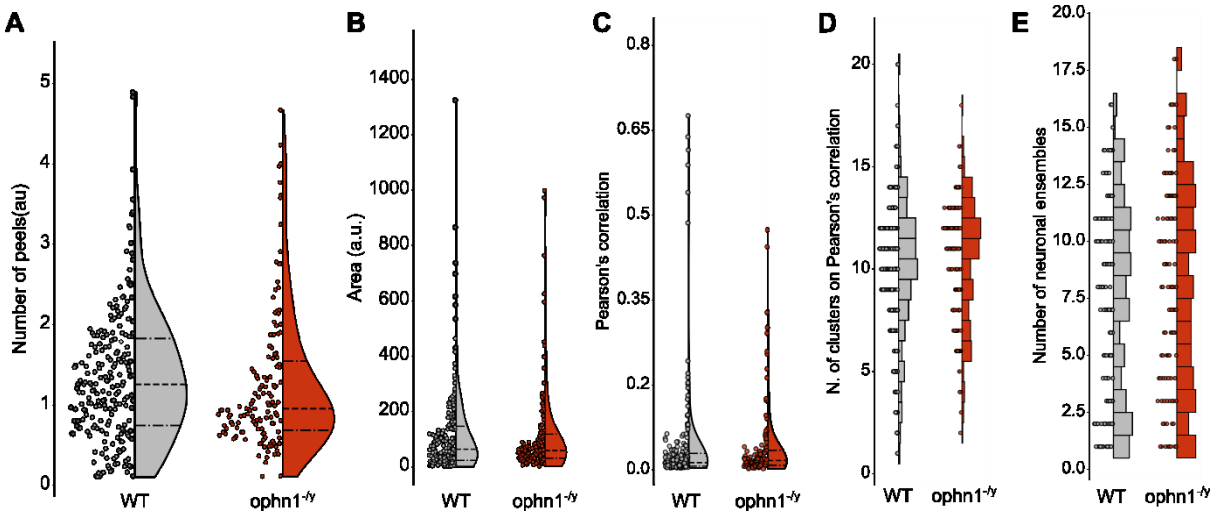

Figure 27. **Analysis on the pre-stimulus time window.** A) Integral of the calcium signal for the two genotypes (p = 0.88). B) Number of identified peaks for WT and ophn1$^{-/y}$ in the pre-stimulus interval (p = 0.054). C) Pearson's correlation values on the pre-stimulus interval. D) Cluster based on the Pearson's correlation values (p = 0.12). E) Neuronal ensembles found for the pre-stimulus interval (p = 0.27).

Fasudil treatment rescue behavioural performance in ophn1$^{-/y}$ mice.

Previous studies have shown that at least some defects triggered by ophn1 mutation can be ascribed to an overactivation of the Rho A kinase and of its major downstream effector (ROCK); therefore, such defects could be rescued by administration of a ROCK inhibitor, Fasudil. We treated ophn1$^{-/y}$ animals with a chronic administration of Fasudil dissolved in daily drinking water for three weeks. At the end of the treatment period, the animals were tested with the habituation-dishabituation task and then with the OFT assays. Animals were tested in the habituation-dishabituation task, as described above (see "Habituation-dishabituation" in the Materials and Methods section). We observed that ophn1$^{-/y}$ treated with Fasudil exhibited habituation and dishabituation effects. These data clearly indicate a rescue of the olfactory behavior in animals treated with Fasudil.

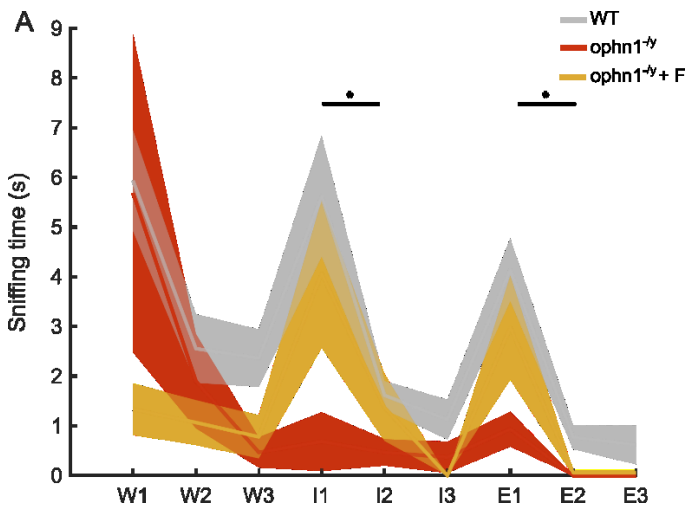

Figure 28. **Fasudil rescues the olfactory behavior during the habituation-dishabituation trial.** Ophn1$^{-/y}$ mice treated with Fasudil mice exhibit a higher dishabituation to the olfactory stimuli presented in sequence, with respect to ophn1$^{-/y}$ for the isoamyl acetate ($p = 0.04$). and longer sniffing time during the habituation trials, after the isoamyl acetate ($p = 0.04$) and the eugenol ($p = 0.05$).

On the other hand, ophn1$^{-/y}$-treated mice exhibited a significant increase in locomotor activity, in the open field test with untreated ophn1$^{-/y}$ (Fig. 28 C; ophn1$^{-/y}$ vs. ophn1$^{-/y}$ + Fasudil: 1.35 s ± 0.71 vs. 2.61 s ± 0.57). The speed of ophn1$^{-/y}$ treated mice was however not different with respect to WT (Fig. 28 C; WT vs. ophn1$^{-/y}$ +

Fasudil: 1.95 cm/s ± 0.56 vs. 2.61 cm/s ± 0.57). Moreover, ophn1$^{-/y}$-treated mice presented no difference in the occupancy ratios with respect to both WT (Fig. 28 D; WT vs. ophn1$^{-/y}$ + Fasudil: 0.36 ± 0.47 vs. 0.20 ± 0.19) and untreated ophn1$^{-/y}$ animals (Fig. 28 D; ophn1$^{-/y}$ vs. ophn1$^{-/y}$ + Fasudil: 0.33 ± 0.29 vs. 0.20 ± 0.19).

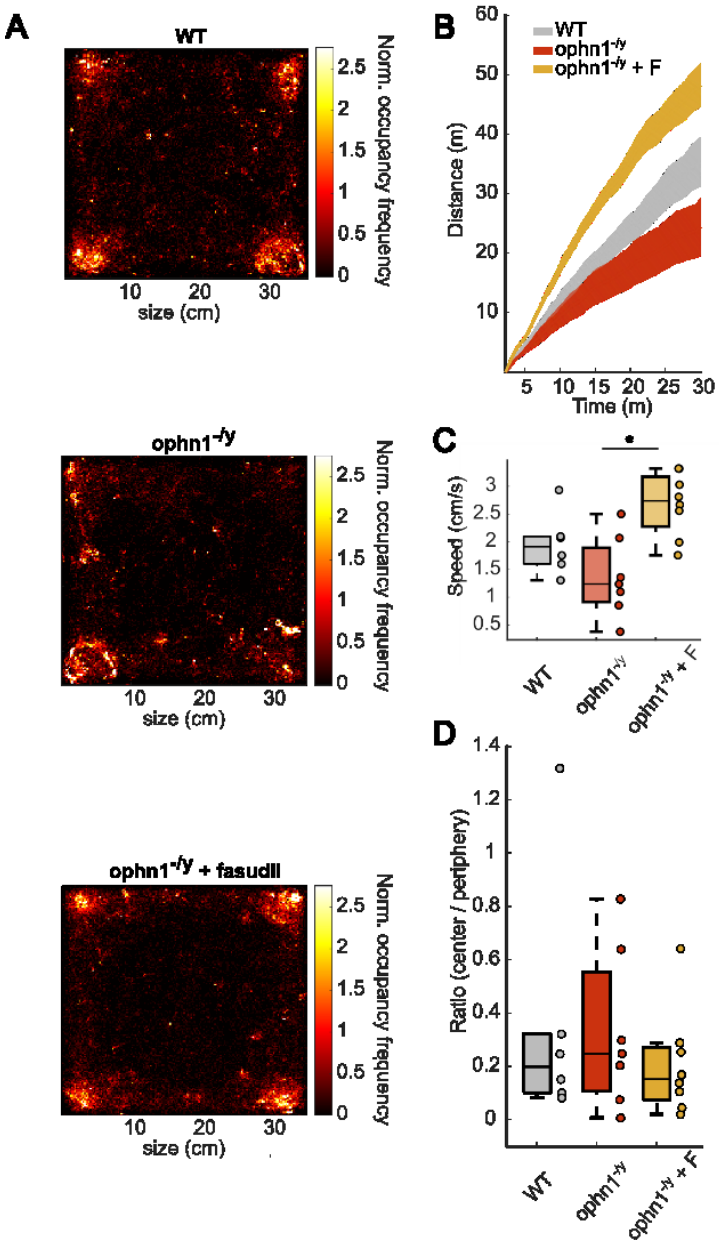

Figure 29 **Fasudil slightly impact on ophn1$^{-/y}$ locomotor activity.** A) Occupancy maps for WT (top panel), ophn1$^{-/y}$ and treated ophn1$^{-/y}$. and B) Total distance covered by the two groups over the 30-m period of free exploration. F) Mean body speed of the two groups resulted in a significant difference between untreated and treated ophn1$^{-/y}$ mice (p = 0.001), while we observed no difference between WT and treated animals (p = 0.07). G) Occupancy ratios highlighted no differences in treated animals with both WT (p = 0.39) and ophn1$^{-/y}$ (p = 0.36) animals.

Effects of Fasudil treatment on the LFP signal recorded in the OB.

The same animals that carried out the habituation-dishabituation task and the OFT, were then implanted with chronic electrodes, and LFPs were eventually recorded in their OB. Also in this case, mice were freely behaving within an arena and subsequently video recorded. Finally, their behavior was segmented in "resting" and "exploring" conditions. We computed the normalized power distribution for the resting and the exploring conditions, and we quantified the relative difference between the two conditions ("resting" vs. "exploring") across the three genotypes (ophn1$^{-/y}$-treated animals, untreated ophn1$^{-/y}$, and WTs). Ophn1$^{-/y}$-treated animals exhibited no statistical differences in the beta power, with respect to both WT (Fig. 29; WT vs. ophn1$^{-/y}$: 0.10 ± 0.10 vs. 0.36 ± 0.26) and untreated ophn1$^{-/y}$ (Fig. 29; 0.54 ± 0.21 vs. 0.36 ± 0.26), denoting at least a partial recovery of the LFP power in these conditions. On the other hand, high-gamma power in animals treated with Fasudil remained significantly different with WT mice (Fig. 29; WT vs. ophn1$^{-/y}$ + Fasudil: 1.01 ± 0.19 vs. 0.70 ± 0.12), exhibiting no differences with respect to untreated ophn1$^{-/y}$ animals (Fig. 29; ophn1$^{-/y}$ vs. ophn1$^{-/y}$ + Fasudil: 0.63 ± 0.15 vs. 0.70 ± 0.12). Altogether these results indicate a partial effect of fasudil on network oscillations in the OB.

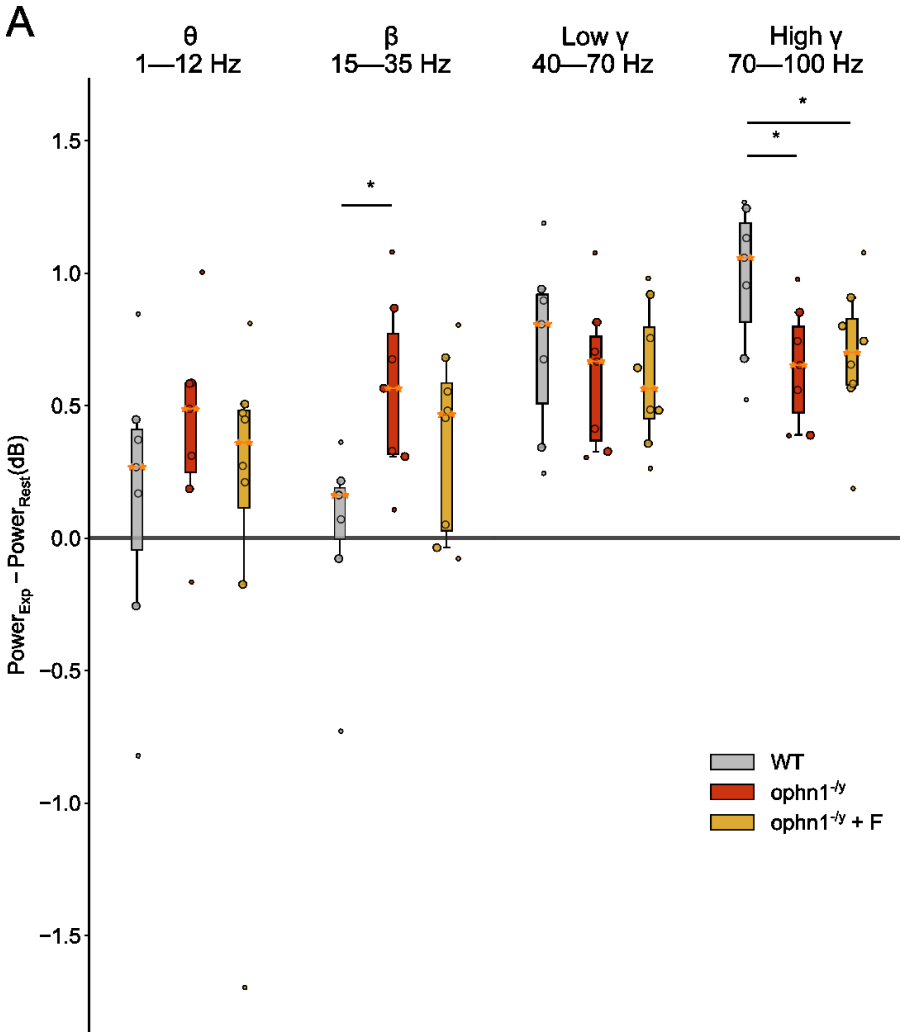

Figure 30. **Fasudil leads to a partial rescue of the ophn1$^{-/y}$ phenotype in the LFP.** A) Power difference was segmented between the four considered frequency bands (i.e., theta, beta, low-gamma and high-gamma). The power difference highlights no statistically significant power differences in the beta band neither with WT ($p = 0.24$) nor with untreated ophn1$^{-/y}$ ($p = 0.42$), but a statistically significant power difference is found in the high-gamma band between the Fasudil-treated animals and the WT ($p = 0.03$), but not the untreated ophn1$^{-/y}$ ($p = 0.42$) animals.

Discussion.

In this study we characterized for the first time the impact of OPHN1 deficiency in the behavioral and network dynamics in the olfactory bulb, *in vivo*. Ophn1$^{-/y}$'s phenotype was impaired when animals underwent an olfactory habituation-dishabituation assay, while exhibiting a similar behavior to their control littermates for what concerned the spontaneous exploration of the environment, indicating an unaffected locomotor activity. Electrophysiological recordings of LFPs in the OB during spontaneous exploration of the environment showed significant alterations in the beta and high-gamma frequency bands, for both the "resting" and "exploring" conditions. Using two-photon calcium imaging we characterized OB neuronal population activity with single-cell resolution, observing a reduced amplitude and an increased delay in calcium responses to odorant stimuli, along with a reduced complexity at the network level in ophn1$^{-/y}$ mice. Administration of the RhoA/ROCK inhibitor Fasudil completely rescued the behavioral phenotype, while partially recovering LFPs's abnormal features.

Ophn1$^{-/y}$ mice do not dishabituate to the olfactory stimuli without exhibiting gross locomotor and exploratory impairments.

The first step of our investigation involved assessing the olfactory behavior of ophn1$^{-/y}$ mice. For this purpose, we employed a widely used olfactory assay, the habituation-dishabituation task. In brief, this task is designed to assess how animals respond to changes in olfactory stimuli over time. When undergoing this task, unconditioned WT animals would reduce the sniffing time spent on a given olfactory cue presented several times (i.e. habituation trials), while increasing the sniffing time when a new odorant is presented (i.e., dishabituation trials). The

habituation-dishabituation paradigm is valuable for studying sensory perception, memory, and discrimination abilities in mice[125,126].

Our results clearly pointed out defects in ophn1$^{-/y}$ mice, with respect to their WT littermates, in carrying out the assay. Mutant mice did not exhibit a dishabituation behavior once the habituation to the first stimulus was established, neither in the case of isoamyl acetate nor in the case of eugenol. There are several explanations for such behavioral impairments: the first implicates a defection of the mice to process the olfactory stimuli *per se*. A failure to dishabituate, and thus to exhibit an increased interest or responsiveness when presented with a novel stimulus during the dishabituation phase may suggest difficulties in discriminating between the different odors, and this – in turn – could implicate impairments in olfactory discrimination abilities[125]. By ascertaining a similar behavior in carrying out the OFT between mutant and WT mice, we excluded the possibility that the impaired olfactory behavior could be ascribed to the inability of ophn1$^{-/y}$ to reach and explore the odorant stimuli. The occupancy ratios confirmed a similar behavior between the two genotypes, excluding the possibility that abnormalities in carrying out this task could refer to an elevated stress, anxiety, or to general motor deficits.

Seeking to decipher the neuronal basis underlying the impaired olfactory behavior, we recorded LFPs in the OB during a spontaneous behavior in the absence of odorant stimulation, namely, when animals were recorded freely moving within an arena.

Mutant mice exhibit aberrant rhythms in the OB.

OB characterization with LFPs was carried out taking into consideration two major behaviors the animals could exhibit during spontaneous activity: one associated with active sniffing exploration ("exploring"), and a latter related to a low arousal

state ("resting"), during which the animals remained still. The spectral analysis was conducted taking into consideration the frequency bands of oscillations well-characterized in the OB. WT animals show – as expected – an increase in the high-gamma activity during the "exploring" condition, compared with the "resting" one. On the other hand, although ophn1$^{-/y}$ mice also displayed an increase in the high-gamma power during the "exploring" condition, such increase was significantly reduced with respect to WT animals. Moreover, we observed for ophn1$^{-/y}$ mice an additional difference at the level of the beta band: a reduction in power during the "resting" condition, while an increase during the "exploring" phase. Given that there were no discernible variations in the theta band across all conditions, a frequency traditionally linked to the sniffing rhythm, it is reasonable to consider ruling out any distinctions in sniffing patterns between the two genotypes. Importantly, beta oscillations in the OB are supported by a wider network of brain areas, and mostly importantly by the piriform cortex. Therefore, an increased beta power observed in ophn1$^{-/y}$ could be ascribed to defects at the level of either the OB network or at the level of the piriform cortex, possibly a target area for further investigations.

Conversely, high-gamma activity is supported by local networks integral to the OB (by the feedback loop between the excitatory M/T cells and the local inhibitory GABAergic cells, the granule cells), and it is associated to the processing of the incoming sensory information: namely, high-gamma power increases as a consequence of sniffing activity, and in response to task demand – indeed, it has been shown how higher gamma activity is present in response to more difficult discriminations than in easier ones[97]. The reduced increase in the ophn1$^{-/y}$ gamma power, thus, suggests an alteration at the level of the OB circuitry.

Importantly, oscillations are critically regulated by inhibitory interneurons which dictate the frequency of the oscillations and correlate the activity among pyramidal neurons. The role of inhibitory GABAergic interneurons has been thoroughly

addressed especially in gamma oscillations, and PV inhibitory interneurons have been demonstrated to orchestrate the underlying computation to this[53]. Not surprisingly, defects in PV function result in a reduced gamma power, which can be rescued by restoring the functionality of the inhibitory circuitry[131].

Lastly, morphological and functional alteration of inhibitory interneurons is a hallmark in neurodevelopmental disorders and is considered a unifying mechanistic link to the wide spectrum of ID-ASD. In ophn1$^{-/y}$ mice, it has been shown that forebrain GABAergic interneurons, generated postnatally, exhibit several defects in their morphology and synaptic functionality[30]; moreover, also newly-generated inhibitory interneurons show altered migrating dynamics, eventually resulting in a reduced number of GC in the OB[132]. Ultimately, altered oscillations in the OB point to alterations in the GABA circuitry. In spite of this speculation, whether and how the resident GABA population is affected in ophn1$^{-/y}$ remains a crucial point to be clarified.

Finally, the readout of the LFP should not be confused with the firing rate of OB neurons, since a higher gamma power expresses a more coordinated activity among neurons recorded in this frequency band, and not a higher firing rate of the neuronal population in this brain region.

Absence of OPHN1 impairs neuronal network organization in the OB.

LFPs recordings are an invaluable tool to define aberrant rhythms in the OB circuitry of ophn1$^{-/y}$ mice, although their limited spatial resolution left unaddressed the characterization of single cells responses within this target brain region; similarly, the underlying spatio-temporal organization of the OB neurons during their coordinated activity could not be resolved by the sole recording of LFPs. To address these open questions, we performed two-photon calcium imaging in the

OB, focusing on the activity of M/T cells. Imaging sessions were conducted on anesthetized animals subjected to a complex odorant mix stimulation in order to maximally activate the OB network. The experimental protocol comprised ten stimuli (7 odorant mix stimuli and 3 mineral oil, presented in a pseudo-randomized sequence), to which we observed no differences at the level of responsive cells in a time window of 30 seconds of post-stimulus activity. Such time window was chosen according with the objective to characterize an early sensory-evoked activity, and a stimulus-related subsequent phase of activity. Both WT and ophn1$^{-/y}$ exhibited a highly significant increase in calcium activity when presented with the odorant mix, compared to the control (i.e., mineral oil). This result suggests that ophn1$^{-/y}$ animals are responsive to olfactory cues, further supporting the electrophysiological data. We observed a significant difference in the integral of $\Delta F/F$ signal over time in response to the stimulation, between the genotypes. To characterize the early and the late response to sensory stimuli, we adapted a "peeling algorithm" on our imaging data, originally implemented by Grewe and colleagues[124] to identify individual calcium events associated with instantaneous increase in the firing rate of the cells. We adapted the peeling procedure to identify single calcium peaks and define their amplitude and delay with respect to the stimulus presentation. The peeling procedure reconstructed traces for the WT and ophn1$^{-/y}$, with no statistical differences between the RMSE. With this computational approach, we decomposed the overall 30 seconds of post-stimulus activity in discrete calcium events and analyzed the network activity on a fine-grained scale. The average number of identified peaks was significantly larger in WT animals with respect to ophn1$^{-/y}$ during the whole post-stimulus time window. Calcium events were sorted according to the time to peak relative to the triggering of the olfactory stimulus, indicated as delay, and separately analyzed. On average, first peaks exhibited a significantly higher amplitude for ophn1$^{-/y}$, compared to WT, with no difference in terms of the delay. We considered this first peak as the

putative "early" response to the sensory stimulus, while the remaining peaks formed what we considered as the "late" response. The amplitude of such "late" response, for each peak, was higher in WT animals with respect of ophn1$^{-/y}$. The delay of the remaining peaks, after the first one, was significantly longer in the mutated mice with respect to controls. These results gave us a measure of the relative excitability of the OB network in response to the olfactory stimulation: in this sense, it appears that ophn1$^{-/y}$ mice exhibit a higher, early excitability period followed by a reduced and delayed one, with respect to WTs. Moreover, this evidence further supports a possible alteration in the information processing at the level of the OB in ophn1$^{-/y}$ animals.

To further characterize network properties, we first computed a Pearson's correlation analysis on our peeling-reconstructed traces. Pearson's correlation is a measure of the average normalized covariance between two signals. In our case a high Pearson's correlation expressed a similar unfolding of calcium events over time, across cells. Over the whole 30 seconds of post-stimulus activity, we found no differences between the genotypes; considering only the early response to the odorant stimulation (i.e. the first peak), again we observed no differences between WT and ophn1$^{-/y}$ mice. In contrast, when considering the late part of the response (i.e. all the remaining peaks but the firs one), ophn1$^{-/y}$ exhibited a reduced average Pearson's correlation. This results further support the idea that the olfactory response comprises two functionally distinct components, even at the level of the network activity. The reduced Pearson's correlation in the late response is in line with the reduced gamma activity we observed in our electrophysiological data, expressing a less coordinated activity between ophn1$^{-/y}$ mice's cells.

Since the Pearson's correlation analysis is a measure of network coordination, we hypothesized that a more complex network would result in a higher number of functional modules contributing to correlation value. For this reason, we decomposed the Pearson's correlation pattern in clusters of functionally active

cells. We found a higher number of functional clusters in WT, with respect to the mutated mice, for both the whole 30 seconds of post-stimulus activity and for the early part of the response alone. Conversely, when considering the late part of the response, it emerged an apparent paradoxical increase in the number of functional modules, for ophn1$^{-/y}$ mice with respect to WT. In this sense, it appears that WT might have a "richer" representation of the sensory-evoked stimulus, that is balanced by a more nuanced stimulus representation of ophn1$^{-/y}$ during the late phase of the response. Still, results on the number of clusters calculated on the Pearson's correlation matrices, for the pre-stimulus activity, highlight no significant differences between the number of modules in the late phase of the response and precisely the ones in the pre-stimulus activity: this result holds just for ophn1$^{-/y}$ mice, but not for WT which persist to exhibit a reduced number of modules with respect of the pre-stimulus activity. In this sense, it is tempting to speculate that after a period of increased excitability and more coordinated activity, ophn1$^{-/y}$ network rapidly returns to a pre-stimulus condition of minor excitability and less coordinated activity.

Another measure of network functional organization that we took into consideration is the ensemble structure proposed by Yuste and colleagues[111]. An ensemble of neurons is considered as a collection of coactive cells that consistently appears in the data, more than expected by chance. Such functional structures have been associated to both encoding – and decoding – of sensory stimuli, as well as to spontaneous features; importantly, they have been shown to be altered in animal models of psychiatric disorders[120]. We extracted the ensemble structure from the peeling-reconstructed data, finding no differences for what concerned the whole 30 seconds post-stimulus response, while observing a significantly higher number of neuronal ensembles in WT in both the early and late phase of the response activity. Such evidence is complementary to the clustering operated on Pearson's correlation matrices, as they originate from two different computational operations

aimed at reflecting two distinct physiological processes. In the first case, neuronal ensembles are considered to be building blocks of network activity, while in the latter case, clusters calculated on the Pearson's correlation matrices vary across states and do not assume any pre-existing underlying structure. Ultimately, they are dynamically modulated in response to sensory stimulation and – in turn – assume different values in the presence or in absence of the sensory stimulation.

Replicated our analyses on the 30 seconds of pre-stimulus time window, we highlighted no differences in the integrated ΔF/F signal over time, in the number of identified peaks, in the average Pearson's correlation – and relative functional modules – and in the number of identified neuronal ensembles. For this reason, we could not ascribe ophn1$^{-/y}$ defections in light of an alteration in the spontaneous activity of the mice.

Fasudil rescues part of the ophn1$^{-/y}$ behavioral and spectral phenotype.

Finally, we examined how a RhoA/ROCK inhibitor influenced the ophn1$^{-/y}$ phenotype. Preceding results demonstrated its effectiveness in alleviating numerous behavioral and cellular defects linked to the ophn1 mutation – although it's worth noting that the inhibitor did not fully address all observed abnormalities[31]. Recently, chronic treatment with Fasudil was shown to recover behavioral deficits in mice selectively lacking OPHN1 in the prefrontal cortex[35].

We found that chronic administration of Fasudil completely rescued the behavioral phenotype in the habituation-dishabituation assay, with Fasudil-treated animals capable of both habituating and dishabituating to the sensory stimuli. As for their exploratory activity, treated animals exhibited a higher average speed during the OFT with respect to untreated ophn1$^{-/y}$, while no difference was observed with WT animals. Moreover, Fasudil had no effects on the occupancy maps of treated animals, which showed no differences with respect to both WT and untreated

ophn1$^{-/y}$. The same mice that carried out the habituation-dishabituation assay and the open field test underwent LFP recording in the OB. In this case, results highlighted a relative decrease in the power in the beta-band activity (suggesting a partial rescue of the ophn1$^{-/y}$ phenotype), while no difference emerged in the high-gamma band power, with treated animals being significantly different with WTs, but not with ophn1$^{-/y}$. In light of this partial rescue, further experiments will be needed to dissect the relative contribution of Fasudil in modulating the olfactory network activity at the level of the OB and in higher brain areas. Fasudil partial rescued the abnormal increase in power in the beta frequency band, while being ineffective on the high-gamma activity. Because Fasudil a drug that selectively target the Rho A/ROCK activity, we do not point out what could be its possible contribution to the inhibitory network activity. Since brain oscillations are critically regulated by the inhibitory circuitry and Cl^- homeostasis, a potential future direction in dissecting the impact of OPHN1 on neuronal network dynamics would be to investigate this precise aspect, possibly developing tailored treatments for this pathology.

Bibliography.

1. Coplan, J. Three Pitfalls in the Early Diagnosis of Mental Retardation. *Clin Pediatr (Phila)* **21**, 308–310 (1982).
2. Galasso, C. *et al.* Deletion 2q37: an identifiable clinical syndrome with mental retardation and autism. *J Child Neurol* **23**, 802–806 (2008).
3. Lecavalier, L., Snow, A. V. & Norris, M. Autism Spectrum Disorders and Intellectual Disability. in *International Handbook of Autism and Pervasive Developmental Disorders* (eds. Matson, J. L. & Sturmey, P.) 37–51 (Springer, New York, NY, 2011). doi:10.1007/978-1-4419-8065-6_4.
4. Matson, J. L. & Shoemaker, M. Intellectual disability and its relationship to autism spectrum disorders. *Research in Developmental Disabilities* **30**, 1107–1114 (2009).
5. Leonard, H. *et al.* A systematic review of the biological, social, and environmental determinants of intellectual disability in children and adolescents. *Frontiers in Psychiatry* **13**, (2022).
6. Petitpierre, G., Dind, J. & De Blasio, C. Olfactive short-term habituation in children and young people with profound intellectual and multiple disabilities. *Research in Developmental Disabilities* **140**, 104569 (2023).
7. Harris, J. C. & Greenspan, S. Definition and Nature of Intellectual Disability. in *Handbook of Evidence-Based Practices in Intellectual and Developmental Disabilities* (ed. Singh, N. N.) 11–39 (Springer International Publishing, Cham, 2016). doi:10.1007/978-3-319-26583-4_2.
8. Maulik, P. K., Mascarenhas, M. N., Mathers, C. D., Dua, T. & Saxena, S. Prevalence of intellectual disability: A meta-analysis of population-based studies. *Research in Developmental Disabilities* **32**, 419–436 (2011).

9. Ellison, J. W., Rosenfeld, J. A. & Shaffer, L. G. Genetic Basis of Intellectual Disability. *Annual Review of Medicine* **64**, 441–450 (2013).

10. Guilmatre, A. *et al.* Recurrent Rearrangements in Synaptic and Neurodevelopmental Genes and Shared Biologic Pathways in Schizophrenia, Autism, and Mental Retardation. *Archives of General Psychiatry* **66**, 947–956 (2009).

11. Bilder, D. A. *et al.* Prenatal and Perinatal Factors Associated with Intellectual Disability. *American Journal on Intellectual and Developmental Disabilities* **118**, 156–176 (2013).

12. Hisle-Gorman, E. *et al.* Prenatal, perinatal, and neonatal risk factors of autism spectrum disorder. *Pediatr Res* **84**, 190–198 (2018).

13. Lehrke, R. A theory of X-linkage of major intellectual traits. *American Journal of Mental Deficiency* **76**, 611–619 (1972).

14. Verkerk, A. J. M. H. *et al.* Identification of a gene (FMR-1) containing a CGG repeat coincident with a breakpoint cluster region exhibiting length variation in fragile X syndrome. *Cell* **65**, 905–914 (1991).

15. Ramakers, G. J. A. Rho proteins, mental retardation and the cellular basis of cognition. *Trends in Neurosciences* **25**, 191–199 (2002).

16. Luo, L., Jan, L. & Jan, Y. N. Small GTPases in axon outgrowth. *Perspect Dev Neurobiol* **4**, 199–204 (1996).

17. Li, Z., Van Aelst, L. & Cline, H. T. Rho GTPases regulate distinct aspects of dendritic arbor growth in Xenopus central neurons in vivo. *Nat Neurosci* **3**, 217–225 (2000).

18. Allen, K. M. *et al.* PAK3 mutation in nonsyndromic X-linked mental retardation. *Nat Genet* **20**, 25–30 (1998).

19. Kutsche, K. *et al.* Mutations in ARHGEF6, encoding a guanine nucleotide exchange factor for Rho GTPases, in patients with X-linked mental retardation. *Nat Genet* **26**, 247–250 (2000).

20. Billuart, P. *et al.* Oligophrenin-1 encodes a rhoGAP protein involved in X-linked mental retardation. *Nature* **392**, 923–926 (1998).

21. Purpura, D. P. Dendritic Spine 'Dysgenesis' and Mental Retardation. *Science* **186**, 1126–1128 (1974).

22. Govek, E.-E. *et al.* The X-linked mental retardation protein oligophrenin-1 is required for dendritic spine morphogenesis. *Nat Neurosci* **7**, 364–372 (2004).

23. Nakano-Kobayashi, A., Tai, Y., Kasri, N. N. & Aelst, L. V. The X-linked Mental Retardation Protein OPHN1 Interacts with Homer1b/c to Control Spine Endocytic Zone Positioning and Expression of Synaptic Potentiation. *J. Neurosci.* **34**, 8665–8671 (2014).

24. Häusser, M., Spruston, N. & Stuart, G. J. Diversity and Dynamics of Dendritic Signaling. *Science* **290**, 739–744 (2000).

25. Fauchereau, F. *et al.* The RhoGAP activity of OPHN1, a new F-actin-binding protein, is negatively controlled by its amino-terminal domain. *Molecular and Cellular Neuroscience* **23**, 574–586 (2003).

26. Aelst, L. V. & D'Souza-Schorey, C. Rho GTPases and signaling networks. *Genes Dev.* **11**, 2295–2322 (1997).

27. Luo, L. RHO GTPASES in neuronal morphogenesis. *Nat Rev Neurosci* **1**, 173–180 (2000).

28. Nakano-Kobayashi, A., Kasri, N. N., Newey, S. E. & Van Aelst, L. The Rho-Linked Mental Retardation Protein OPHN1 Controls Synaptic Vesicle Endocytosis via Endophilin A1. *Current Biology* **19**, 1133–1139 (2009).

29. Kasri, N. N., Nakano-Kobayashi, A., Malinow, R., Li, B. & Aelst, L. V. The Rho-linked mental retardation protein oligophrenin-1 controls synapse maturation and plasticity by stabilizing AMPA receptors. *Genes Dev.* **23**, 1289–1302 (2009).

30. Redolfi, N. *et al.* Oligophrenin-1 regulates number, morphology and synaptic properties of adult-born inhibitory interneurons in the olfactory bulb. *Human Molecular Genetics* **25**, 5198–5211 (2016).

31. Maset, A. *et al.* Altered Cl− homeostasis hinders forebrain GABAergic interneuron migration in a mouse model of intellectual disability. *Proceedings of the National Academy of Sciences* **118**, e2016034118 (2021).

32. Busti, I. *et al.* ROCK/PKA Inhibition Rescues Hippocampal Hyperexcitability and GABAergic Neuron Alterations in a Oligophrenin-1 Knock-Out Mouse Model of X-Linked Intellectual Disability. *J. Neurosci.* **40**, 2776–2788 (2020).

33. Marín, O. Interneuron dysfunction in psychiatric disorders. *Nat Rev Neurosci* **13**, 107–120 (2012).

34. Khelfaoui, M. *et al.* Loss of X-Linked Mental Retardation Gene Oligophrenin1 in Mice Impairs Spatial Memory and Leads to Ventricular Enlargement and Dendritic Spine Immaturity. *J. Neurosci.* **27**, 9439–9450 (2007).

35. Wang, M., Gallo, N. B., Tai, Y., Li, B. & Van Aelst, L. Oligophrenin-1 moderates behavioral responses to stress by regulating parvalbumin interneuron activity in the medial prefrontal cortex. *Neuron* **109**, 1636-1656.e8 (2021).

36. Bakalyar, H. A. & Reed, R. R. Identification of a Specialized Adenylyl Cyclase That May Mediate Odorant Detection. *Science* **250**, 1403–1406 (1990).

37. Buck, L. & Axel, R. A novel multigene family may encode odorant receptors: A molecular basis for odor recognition. *Cell* **65**, 175–187 (1991).

38. De Castro, F. Wiring olfaction: the cellular and molecular mechanisms that guide the development of synaptic connections from the nose to the cortex. *Frontiers in Neuroscience* **3**, (2009).

39. Miyamichi, K., Serizawa, S., Kimura, H. M. & Sakano, H. Continuous and Overlapping Expression Domains of Odorant Receptor Genes in the Olfactory Epithelium Determine the Dorsal/Ventral Positioning of Glomeruli in the Olfactory Bulb. *J. Neurosci.* **25**, 3586–3592 (2005).

40. Ressler, K. J., Sullivan, S. L. & Buck, L. B. A zonal organization of odorant receptor gene expression in the olfactory epithelium. *Cell* **73**, 597–609 (1993).

41. Vassar, R., Ngai, J. & Axel, R. Spatial segregation of odorant receptor expression in the mammalian olfactory epithelium. *Cell* **74**, 309–318 (1993).

42. Lodovichi, C., Belluscio, L. & Katz, L. C. Functional Topography of Connections Linking Mirror-Symmetric Maps in the Mouse Olfactory Bulb. *Neuron* **38**, 265–276 (2003).

43. Ressler, K. J., Sullivan, S. L. & Buck, L. B. Information coding in the olfactory system: Evidence for a stereotyped and highly organized epitope map in the olfactory bulb. *Cell* **79**, 1245–1255 (1994).

44. Vassar, R. *et al.* Topographic organization of sensory projections to the olfactory bulb. *Cell* **79**, 981–991 (1994).

45. Schröder, H., Moser, N. & Huggenberger, S. The Mouse Olfactory System. in *Neuroanatomy of the Mouse: An Introduction* (eds. Schröder, H., Moser, N. & Huggenberger, S.) 319–331 (Springer International Publishing, Cham, 2020). doi:10.1007/978-3-030-19898-5_14.

46. Egger, V., Svoboda, K. & Mainen, Z. F. Mechanisms of Lateral Inhibition in the Olfactory Bulb: Efficiency and Modulation of Spike-Evoked Calcium Influx into Granule Cells. *J. Neurosci.* **23**, 7551–7558 (2003).

47. Rubin, B. D. & Katz, L. C. Optical Imaging of Odorant Representations in the Mammalian Olfactory Bulb. *Neuron* **23**, 499–511 (1999).

48. Uchida, N., Takahashi, Y. K., Tanifuji, M. & Mori, K. Odor maps in the mammalian olfactory bulb: domain organization and odorant structural features. *Nat Neurosci* **3**, 1035–1043 (2000).

49. Wachowiak, M. & Shipley, M. T. Coding and synaptic processing of sensory information in the glomerular layer of the olfactory bulb. *Seminars in Cell & Developmental Biology* **17**, 411–423 (2006).

50. Nagayama, S., Homma, R. & Imamura, F. Neuronal organization of olfactory bulb circuits. *Frontiers in Neural Circuits* **8**, (2014).

51. Buzsáki, G. Neural syntax: cell assemblies, synapsembles and readers. *Neuron* **68**, 362–385 (2010).

52. Buzsáki, G., Logothetis, N. & Singer, W. Scaling Brain Size, Keeping Timing: Evolutionary Preservation of Brain Rhythms. *Neuron* **80**, 751–764 (2013).

53. Buzsáki, G., Anastassiou, C. A. & Koch, C. The origin of extracellular fields and currents — EEG, ECoG, LFP and spikes. *Nat Rev Neurosci* **13**, 407–420 (2012).

54. Leung, L.-W. S. & Yim, C.-Y. C. Intrinsic membrane potential oscillations in hippocampal neurons in vitro. *Brain Research* **553**, 261–274 (1991).

55. Hutcheon, B. *et al.* Resonance, oscillation and the intrinsic frequency preferences of neurons. *Trends in Neurosciences* **23**, 216–222 (2000).

56. Llinás, R. R. The Intrinsic Electrophysiological Properties of Mammalian Neurons: Insights into Central Nervous System Function. *Science* **242**, 1654–1664 (1988).

57. Singer, W. Neuronal Synchrony: A Versatile Code for the Definition of Relations? *Neuron* **24**, 49–65 (1999).

58. Singer, W. Neuronal oscillations: unavoidable and useful? *European Journal of Neuroscience* **48**, 2389–2398 (2018).

59. Wang, X. J. & Buzsáki, G. Gamma oscillation by synaptic inhibition in a hippocampal interneuronal network model. *J Neurosci* **16**, 6402–6413 (1996).

60. Traub, R. D., Whittington, M. A., Colling, S. B., Buzsáki, G. & Jefferys, J. G. Analysis of gamma rhythms in the rat hippocampus in vitro and in vivo. *J Physiol* **493**, 471–484 (1996).

61. Wang, X.-J. & Buzsáki, G. Gamma Oscillation by Synaptic Inhibition in a Hippocampal Interneuronal Network Model. *J. Neurosci.* **16**, 6402–6413 (1996).

62. Fries, P., Nikolić, D. & Singer, W. The gamma cycle. *Trends in Neurosciences* **30**, 309–316 (2007).

63. Hansel, D. & Mato, G. Asynchronous states and the emergence of synchrony in large networks of interacting excitatory and inhibitory neurons. *Neural Comput* **15**, 1–56 (2003).

64. Buzsáki, G. & Wang, X.-J. Mechanisms of Gamma Oscillations. *Annual Review of Neuroscience* **35**, 203–225 (2012).

65. Singer, W. & Gray, C. M. Visual Feature Integration and the Temporal Correlation Hypothesis. *Annual Review of Neuroscience* **18**, 555–586 (1995).

66. Canolty, R. T. *et al.* High gamma power is phase-locked to theta oscillations in human neocortex. *Science* **313**, 1626–1628 (2006).

67. Chrobak, J. J. & Buzsáki, G. Gamma oscillations in the entorhinal cortex of the freely behaving rat. *J Neurosci* **18**, 388–398 (1998).

68. O'Keefe, J. & Recce, M. L. Phase relationship between hippocampal place units and the EEG theta rhythm. *Hippocampus* **3**, 317–330 (1993).

69. Skaggs, W. E., McNaughton, B. L., Wilson, M. A. & Barnes, C. A. Theta phase precession in hippocampal neuronal populations and the compression of temporal sequences. *Hippocampus* **6**, 149–172 (1996).

70. Jacobs, J., Kahana, M. J., Ekstrom, A. D. & Fried, I. Brain Oscillations Control Timing of Single-Neuron Activity in Humans. *J. Neurosci.* **27**, 3839–3844 (2007).

71. Kay, L. M. Olfactory system oscillations across phyla. *Current Opinion in Neurobiology* **31**, 141–147 (2015).

72. Kepecs, A., Uchida, N. & Mainen, Z. F. The Sniff as a Unit of Olfactory Processing. *Chemical Senses* **31**, 167–179 (2006).

73. Berger, H. Über das Elektrenkephalogramm des Menschen. *Archiv f. Psychiatrie* **87**, 527–570 (1929).

74. Stanfield, B. B. The development of the corticospinal projection. *Progress in Neurobiology* **38**, 169–202 (1992).

75. Brosch, M., Budinger, E. & Scheich, H. Stimulus-related gamma oscillations in primate auditory cortex. *J Neurophysiol* **87**, 2715–2725 (2002).

76. Kreiter, A. K. & Singer, W. Stimulus-dependent synchronization of neuronal responses in the visual cortex of the awake macaque monkey. *J. Neurosci.* **16**, 2381–2396 (1996).

77. Wehr, M. & Laurent, G. Odour encoding by temporal sequences of firing in oscillating neural assemblies. *Nature* **384**, 162–166 (1996).

78. Baldauf, D. & Desimone, R. Neural Mechanisms of Object-Based Attention. *Science* **344**, 424–427 (2014).

79. Merker, B. Cortical gamma oscillations: the functional key is activation, not cognition. *Neuroscience & Biobehavioral Reviews* **37**, 401–417 (2013).

80. Bartos, M., Vida, I. & Jonas, P. Synaptic mechanisms of synchronized gamma oscillations in inhibitory interneuron networks. *Nat Rev Neurosci* **8**, 45–56 (2007).

81. Vida, I., Bartos, M. & Jonas, P. Shunting inhibition improves robustness of gamma oscillations in hippocampal interneuron networks by homogenizing firing rates. *Neuron* **49**, 107–117 (2006).

82. Hasenstaub, A. *et al.* Inhibitory Postsynaptic Potentials Carry Synchronized Frequency Information in Active Cortical Networks. *Neuron* **47**, 423–435 (2005).

83. Buzsáki, G. & Chrobak, J. J. Temporal structure in spatially organized neuronal ensembles: a role for interneuronal networks. *Current Opinion in Neurobiology* **5**, 504–510 (1995).

84. Adrian, E. D. Olfactory reactions in the brain of the hedgehog. *J Physiol* **100**, 459–473 (1942).

85. Hayar, A., Karnup, S., Shipley, M. T. & Ennis, M. Olfactory Bulb Glomeruli: External Tufted Cells Intrinsically Burst at Theta Frequency and Are Entrained by Patterned Olfactory Input. *J. Neurosci.* **24**, 1190–1199 (2004).

86. Viertel, R. & Borisyuk, A. A Computational model of the mammalian external tufted cell. *Journal of Theoretical Biology* **462**, 109–121 (2019).

87. Fontanini, A. & Bower, J. M. Variable Coupling Between Olfactory System Activity and Respiration in Ketamine/Xylazine Anesthetized Rats. *Journal of Neurophysiology* **93**, 3573–3581 (2005).

88. Gourévitch, B., Kay, L. M. & Martin, C. Directional coupling from the olfactory bulb to the hippocampus during a go/no-go odor discrimination task. *J Neurophysiol* **103**, 2633–2641 (2010).

89. Zhu, P. *et al.* Odor-induced modification of oscillations and related theta-higher gamma coupling in olfactory bulb neurons of awake and anesthetized rats. *Front Chem* **10**, 865006 (2022).

90. Kay, L. M. & Laurent, G. Odor- and context-dependent modulation of mitral cell activity in behaving rats. *Nat Neurosci* **2**, 1003–1009 (1999).

91. Heale, V. R., Vanderwolf, C. H. & Kavaliers, M. Components of weasel and fox odors elicit fast wave bursts in the dentate gyrus of rats. *Behav Brain Res* **63**, 159–165 (1994).

92. Zibrowski, E. M., Hoh, T. E. & Vanderwolf, C. H. Fast wave activity in the rat rhinencephalon: elicitation by the odors of phytochemicals, organic solvents, and a rodent predator. *Brain Res* **800**, 207–215 (1998).

93. Kay, L. M. Chapter 9 - Circuit Oscillations in Odor Perception and Memory. in *Progress in Brain Research* (eds. Barkai, E. & Wilson, D. A.) vol. 208 223–251 (Elsevier, 2014).

94. Kay, L. M. & Freeman, W. J. Bidirectional processing in the olfactory-limbic axis during olfactory behavior. *Behavioral Neuroscience* **112**, 541–553 (1998).

95. Hermer-Vazquez, R., Hermer-Vazquez, L., Srinivasan, S. & Chapin, J. K. Beta- and gamma-frequency coupling between olfactory and motor brain regions prior to skilled, olfactory-driven reaching. *Exp Brain Res* **180**, 217–235 (2007).

96. Neville, K. R. & Haberly, L. B. Beta and Gamma Oscillations in the Olfactory System of the Urethane-Anesthetized Rat. *Journal of Neurophysiology* **90**, 3921–3930 (2003).

97. Lowry, C. A. & Kay, L. M. Chemical Factors Determine Olfactory System Beta Oscillations in Waking Rats. *Journal of Neurophysiology* **98**, 394–404 (2007).

98. Murthy, V. N. & Fetz, E. E. Oscillatory activity in sensorimotor cortex of awake monkeys: synchronization of local field potentials and relation to behavior. *Journal of Neurophysiology* **76**, 3949–3967 (1996).

99. Kay, L. M. *et al.* Olfactory oscillations: the what, how and what for. *Trends in Neurosciences* **32**, 207–214 (2009).

100. Rojas-Líbano, D. & Kay, L. M. Olfactory system gamma oscillations: the physiological dissection of a cognitive neural system. *Cogn Neurodyn* **2**, 179–194 (2008).

101. Nusser, Z., Kay, L. M., Laurent, G., Homanics, G. E. & Mody, I. Disruption of GABAA Receptors on GABAergic Interneurons Leads to Increased Oscillatory Power in the Olfactory Bulb Network. *Journal of Neurophysiology* **86**, 2823–2833 (2001).

102. Eeckman, F. H. & Freeman, W. J. Correlations between unit firing and EEG in the rat olfactory system. *Brain Res* **528**, 238–244 (1990).

103. Denk, W., Strickler, J. H. & Webb, W. W. Two-photon laser scanning fluorescence microscopy. *Science* **248**, 73–76 (1990).

104. Grienberger, C. & Konnerth, A. Imaging Calcium in Neurons. *Neuron* **73**, 862–885 (2012).

105. Svoboda, K. & Yasuda, R. Principles of Two-Photon Excitation Microscopy and Its Applications to Neuroscience. *Neuron* **50**, 823–839 (2006).

106. Komiyama, T. *et al.* Learning-related fine-scale specificity imaged in motor cortex circuits of behaving mice. *Nature* **464**, 1182–1186 (2010).

107. Chalasani, S. H. *et al.* Dissecting a circuit for olfactory behaviour in Caenorhabditis elegans. *Nature* **450**, 63–70 (2007).

108. Dombeck, D. A., Harvey, C. D., Tian, L., Looger, L. L. & Tank, D. W. Functional imaging of hippocampal place cells at cellular resolution during virtual navigation. *Nat Neurosci* **13**, 1433–1440 (2010).

109. Wang, J. W., Wong, A. M., Flores, J., Vosshall, L. B. & Axel, R. Two-photon calcium imaging reveals an odor-evoked map of activity in the fly brain. *Cell* **112**, 271–282 (2003).

110. Carrillo-Reid, L., Yang, W., Bando, Y., Peterka, D. S. & Yuste, R. Imprinting and recalling cortical ensembles. *Science* **353**, 691–694 (2016).

111. Miller, J. K., Ayzenshtat, I., Carrillo-Reid, L. & Yuste, R. Visual stimuli recruit intrinsically generated cortical ensembles. *Proc Natl Acad Sci U S A* **111**, E4053-4061 (2014).

112. Alejandre-García, T., Kim, S., Pérez-Ortega, J. & Yuste, R. Intrinsic excitability mechanisms of neuronal ensemble formation. *Elife* **11**, e77470 (2022).

113. Carrillo-Reid, L. & Yuste, R. Playing the piano with the cortex: role of neuronal ensembles and pattern completion in perception and behavior. *Current Opinion in Neurobiology* **64**, 89–95 (2020).

114. Hebb, D. O. *The Organization of Behavior: A Neuropsychological Theory*. (Psychology Press, 2005).

115. Carrillo-Reid, L. *et al.* Identification of Pattern Completion Neurons in Neuronal Ensembles Using Probabilistic Graphical Models. *J. Neurosci.* **41**, 8577–8588 (2021).

116. Hopfield, J. J. Neural networks and physical systems with emergent collective computational abilities. *Proceedings of the National Academy of Sciences* **79**, 2554–2558 (1982).

117. Carrillo-Reid, L., Han, S., Yang, W., Akrouh, A. & Yuste, R. Controlling Visually Guided Behavior by Holographic Recalling of Cortical Ensembles. *Cell* **178**, 447-457.e5 (2019).

118. Marshel, J. H. *et al.* Cortical layer–specific critical dynamics triggering perception. *Science* **365**, eaaw5202 (2019).

119. Russell, L. E. *et al.* The influence of visual cortex on perception is modulated by behavioural state. 706010 Preprint at https://doi.org/10.1101/706010 (2019).

120. Hamm, J. P., Peterka, D. S., Gogos, J. A. & Yuste, R. Altered Cortical Ensembles in Mouse Models of Schizophrenia. *Neuron* **94**, 153-167.e8 (2017).

121. Wenzel, M., Hamm, J. P., Peterka, D. S. & Yuste, R. Acute Focal Seizures Start As Local Synchronizations of Neuronal Ensembles. *J Neurosci* **39**, 8562–8575 (2019).

122. Carrillo-Reid, L., Yang, W., Kang Miller, J., Peterka, D. S. & Yuste, R. Imaging and Optically Manipulating Neuronal Ensembles. *Annual Review of Biophysics* **46**, 271–293 (2017).

123. Ben-Shaul, Y. OptiMouse: a comprehensive open source program for reliable detection and analysis of mouse body and nose positions. *BMC Biol* **15**, 41 (2017).

124. Grewe, B. F., Langer, D., Kasper, H., Kampa, B. M. & Helmchen, F. High-speed in vivo calcium imaging reveals neuronal network activity with near-millisecond precision. *Nat Methods* **7**, 399–405 (2010).

125. Wilson, D. A. Olfaction as a model system for the neurobiology of mammalian short-term habituation. *Neurobiology of Learning and Memory* **92**, 199–205 (2009).

126. Wilson, D. A. & Linster, C. Neurobiology of a Simple Memory. *Journal of Neurophysiology* **100**, 2–7 (2008).

127. Silverman, J. L., Yang, M., Lord, C. & Crawley, J. N. Behavioural phenotyping assays for mouse models of autism. *Nat Rev Neurosci* **11**, 490–502 (2010).

128. Agetsuma, M., Hamm, J. P., Tao, K., Fujisawa, S. & Yuste, R. Parvalbumin-Positive Interneurons Regulate Neuronal Ensembles in Visual Cortex. *Cerebral Cortex* **28**, 1831–1845 (2018).

129. Cardin, J. A. Inhibitory Interneurons Regulate Temporal Precision and Correlations in Cortical Circuits. *Trends in Neurosciences* **41**, 689–700 (2018).

130. Carrillo-Reid, L. Neuronal ensembles in memory processes. *Seminars in Cell & Developmental Biology* **125**, 136–143 (2022).

131. Palop, J. J. & Mucke, L. Network abnormalities and interneuron dysfunction in Alzheimer disease. *Nat Rev Neurosci* **17**, 777–792 (2016).

132. Maset, A. *et al.* Aberrant Patterns of Sensory-Evoked Activity in the Olfactory Bulb of LRRK2 Knockout Mice. *Cells* **10**, 3212 (2021).